High-Resolution Temperature Measurement during Forced Convective Heat Transfer at a Wall with a Dimple Structure

Vom Fachbereich Maschinenbau
an der Technischen Universität Darmstadt
zur
Erlangung des akademischen Grades eines Doktor-Ingenieurs (Dr.-Ing.)
genehmigte

D I S S E R T A T I O N

vorgelegt von

M.Sc. Bo Su
aus Shaanxi/China

Berichterstatter:	Prof. Dr.-Ing. Peter Stephan
Mitberichterstatter:	Prof. Dr.-Ing. habil. Nikolai Kornev
Tag der Einreichung:	30.06.2014
Tag der mündliche Prüfung:	09.12.2014

Darmstadt 2015

D 17

Acknowledgements

This study was carried out as my research project in the Institute of Technical Thermodynamics (TTD) at TU Darmstadt. First of all, I would like to thank my advisor, Prof. Dr.-Ing. P. Stephan, head of TTD, for giving me this great opportunity to deepen my knowledge in thermodynamics as well as heat transfer and garner experience in thermo-fluid experiments. I also appreciate his guidance, encouragement, and generous help in this period, which not only benefited me in my studies, but also influenced me in my further career and studies. Second, I would like to thank the German Research Foundation (DFG) for financing my research in this four-year project. Third, I extend my gratitude to the group leaders of the other two teams participating in this project, Prof. Dr.-Ing. E. Hassel from the Department of Technical Thermodynamics (LTT) at Rostock University and Prof. Dr.-Ing. H. Herwig from the Institute of Thermo-Fluid Dynamics at TU Hamburg-Harburg, for supporting and coordinating the meetings and workshops between the teams. Finally, I would also like to appreciate Prof. Dr.-Ing. habil. N. Kornev for sharing many valuable ideas and discussions for this study.

Thank you to all my colleagues who worked with me in these years at TTD. First of all, I would like to give my special thanks to Dr.-Ing. F. Dammel. As my supervisor, he took a lot of time to discuss my ongoing project with me. In fact, his thoughtful instructions and patient consideration made the implementation of the project quite smooth and successful. Second, I would like to thank Dr.-Ing. N. Karwa, M. Budakli, J. Marati, and R. Dayal who are my great friends as well as colleagues. Their brilliant ideas as well as their critical points of view always pushed me forward to once again improve the frontier of the study. I would like to thank Dr.-Ing. N. Schweizer, Dr.-Ing. B. Schilder, Dr.-Ing R. Nasarek, and Dr.-Ing. J. Vogt for sharing with me their specific experiences and knowledge in experiments. Third, I would like to thank my project partners from the other teams: Dr.-Ing. J. Turnow and T. Wenterodt. Because of our close collaboration, the knowledge of dimple structures became more systemic and complete. Finally, I would like to thank all the students, ADPs, and research assistances (HiWis). Particularly, I want to thank S. Pulyaev, who worked with me as a HiWi and helped me a great deal in the experiment, both

with programming and data analysis. His effort pushed the project along much faster than had been originally planned in the first project year of this study.

I would like to thank our secretary G. Gunkel for taking care of daily affairs and the project documents. Here, I also extend my gratitude to R. Schrod and R. Berntheisel, who were responsible for the experimental equipment and manufacturing in the lab. Finally, I would like to thank M. Mattern and D. Schinko for maintaining the office computers and networks.

In the end, I would like to offer my deep appreciation to my parents and my wife Jinfeng. Since starting my studies in Germany, my parents have had to live alone in China without my company. And my wife Jinfeng, I thank you for your support and understanding during these years.

Bo Su

31.12.2013, Bessungen

Abstract

A dimple structure is a concave surface, processed onto a heat transfer surface to promote convective heat transfer. Benefits, such as heat transfer enhancement with moderate flow resistance, less fouling, etc., have been reported by many researchers. Due to the limitations of the experimental method, heat transfer on dimpled surfaces in turbulent flow, which is complex in distribution and dynamic over time, has not yet been fully understood. With the aid of Infrared (IR) Thermography, details of the Nusselt number distributions on these surfaces in high resolution were investigated in this study.

Three surfaces, including a plane surface, a single-dimpled surface, and a double-dimpled surface were observed in turbulent water flow within a dimple Reynolds number range of $\mathrm{Re}_\mathrm{d} = 1 \times 10^4 - 3.5 \times 10^4$ and a flow temperature range of $T_\mathrm{in} = 25 - 43\,°\mathrm{C}$. All surfaces have the same dimple structure with a printing diameter $D_\mathrm{d} = 15.3\,\mathrm{mm}$ and a relative dimple depth $t/D_\mathrm{d} = 0.26$. These surfaces were coated using physical vapor deposition (PVD) technology with an indium tin oxide (ITO) layer, a SiO_2 layer, and copper layers onto the dimpled surfaces of calcium fluoride (CaF_2) glass substrates. During the heating experiment, the ITO layer was charged with direct current (DC) power providing a constant heat flux ($\dot{q}$) up to $53\,\mathrm{kW/m^2}$ from the structured surface through Joule heating. Wall temperature distributions on the heating surface were recorded through the CaF_2 substrate by an IR camera with a spatial and a temporal resolution of 283 μm and 50 Hz, respectively. Before the measurement for each surface, in-situ calibration was conducted to determine the relationship between wall temperature and raw IR intensity from the camera. These IR images include the averaged images (averaged over 10 s) and image sequences over 115 s.

Reattaching zone, recirculating zone, and wake were observed in the wall temperature distribution on dimpled surface. At $\mathrm{Re}_\mathrm{d} = 2 \times 10^4$, a maximum heat transfer region was found in the reattaching zone close to the rear dimple's edge with a Nusselt number ratio ($\mathrm{Nu}_\mathrm{d}/\mathrm{Nu}_\mathrm{pl}$) of around 2, while the rate was found to be around 1 in the recirculating zone. Considering the

influence of three-dimensional distributions of heat transfer, the spanwise-averaged and area-averaged Nusselt number ratios ($\overline{\overline{\mathrm{Nu}}}_{\mathrm{span,\,d}}/\overline{\overline{\mathrm{Nu}}}_{\mathrm{span,\,pl}}$ and $\overline{\overline{\overline{\mathrm{Nu}}}}_{\mathrm{d}}/\overline{\overline{\overline{\mathrm{Nu}}}}_{\mathrm{pl}}$) showed maximum values of 1.6 and 1.3, respectively. In the wake, the heat transfer drops sharply from the higher value near the rear edge to that on the plane surface ($\mathrm{Nu_d}/\mathrm{Nu_{pl}} = 1$) with a distance around $1.5D_{\mathrm{d}}$. The experiment on the double-dimpled surface showed that the maximum Nusselt number ratio in the second dimple was significantly larger than in the dimple upstream. The increase was around 10% at $\mathrm{Re_d} = 2 \times 10^4$.

Heat transfer on dimpled surfaces increased with rising Reynolds number. However, the Nusselt number ratio was observed to decrease with increasing of the Reynolds number. On double dimpled surface, the influence of the upstream dimple in heat transfer became weaker at higher Reynolds numbers. Finally, other experimental parameters, such as the inlet flow temperature and the heat flux, had limited influence on the heat transfer over the dimpled surfaces.

Time resolved temperature distributions showed that a switching mode of the wall temperature between two symmetric states would repeat several times in low frequency as $\mathrm{Re_d} > 1 \times 10^4$. The comparison showed that the switching mode influenced six temperature subzones, which were symmetrically distributed in and downstream of the dimple.

Zusammenfassung

Eine Dellenstruktur besteht aus konkaven Wölbungen, welche in die Oberfläche eines Wärmeübertragers eingebracht sind, um den konvektive Wärmeübergang zu verbessern. Vorteile wie ein verbesserter Wärmeübergang bei moderatem Strömungswiderstand, wenigerem Fouling etc. wurden von vielen Forschern bestätigt. Die Wärmeübertragung an Dellenoberflächen in turbulenter Strömung ist aufgrund der räumlichen Verteilung und der zeitlichen Dynamik sehr komplex. Durch die begrenzten experimentellen Möglichkeiten ist dieser Mechanismus noch nicht vollständig verstanden. Mithilfe von Infrarot-Thermographie wird in dieser Studie die Verteilung der Nusselt-Zahl auf Oberflächen mittels hoher räumlicher und zeitlicher Auflösung untersucht.

Es werden drei Oberflächen in turbulenter Wasserströmung untersucht: Eine ebene Oberfläche, eine Oberfläche mit einer Delle und eine Oberfläche mit zwei in Strömungsrichtung aufeinander folgende Dellen. Die auf den Dellendurchmesser bezogene Reynolds-Zahl beträgt zwischen $\mathrm{Re_d} = 1 \times 10^4$ und 3.5×10^4 bei einer Strömungs-Einlasstemperatur zwischen $T_{\mathrm{in}} = 25$ und 43 °C. Alle Oberflächen weisen die gleichen Dellen auf mit einem Durchmesser von $D_{\mathrm{d}} = 15.3$ mm und einer relativen Tiefe von $t/D_{\mathrm{d}} = 0.26$. Diese Oberflächen werden unter Verwendung des physikalischen Gasphasenabscheidungs-Verfahrens (engl. physical vapor deposition, PVD) beschichtet. Dünne Schichten Indium-Zinn-Oxid (engl. indium tin oxide, ITO), SiO_2 und Kupfer werden auf den mit Dellen versehenen Glas-Träger aus CaF_2 aufgedampft. Während des Experiments wird die ITO-Schicht mit Gleichtstrom beaufschlagt. Aufgrund des Jouleschen Widerstandes der ITO-Schicht stellt sich eine konstante Wärmestromdichte von bis zu $\dot{q} = 53\ \mathrm{kW/m^2}$ ein. Die Temperaturverteilung auf der beheizten Oberfläche wird durch das CaF_2-Glas hindurch mittels einer IR-Kamera mit einer räumlichen und zeitlichen Auflösung von 283 μm und 50 Hz gemessen. Um die Verteilung der Wandtemperatur aus den Kamera-Rohdaten zu ermitteln, wird vor Messungen eine In-Situ-Kalibrierung durchgeführt. Es wurden Sequenzen über eine Zeitspanne von 115 s sowie über 10 s gemittelte Bilder aufgenommen.

Die Verteilung der Wandtemperatur wird in der Wiederanlegezone, dem Rezirkulationsbereich und in der Nachlaufströmung untersucht. Bei $\mathrm{Re_d} = 20000$ befindet sich der Bereich maximaler Wärmeübertragung mit einem Nusselt-Quotienten $\mathrm{Nu_d}/\mathrm{Nu_{pl}}$ von etwa 2 in der Wiederanlegezone der Strömung nahe der hinteren Dellenkante. Zum Vergleich beträgt dieser Quotient im Rezirkulationsbereich etwa 1. Zur Berücksichtigung des Einflusses der dreidimensionalen Verteilung des Wärmetransports werden die quer zur Strömungsrichtung und über die Fläche gemittelten Nusselt-Zahlen-Quotienten $\overline{\mathrm{Nu}}_{\mathrm{span,\,d}}/\overline{\mathrm{Nu}}_{\mathrm{span,\,pl}}$ und $\overline{\overline{\mathrm{Nu}}}_{\mathrm{d}}/\overline{\overline{\mathrm{Nu}}}_{\mathrm{pl}}$ ermittelt. Diese besitzen Maximalwerte von 1.6 und 1.3. Im Nachlaufbereich fällt der Wärmeübergang stark ab vom erhöhten Wert an der hinteren Dellenkante auf den Wert der flachen Oberfläche. Bei der Oberfläche mit zwei Dellen beträgt der Dellenabstand in der Kanalmitte etwa $1.5D_{\mathrm{d}}$. Dieses Experiment zeigt, dass der maximale Nusselt-Quotient in der in Strömungsrichtung hinteren Delle signifikant größer ist als in der vorderen Delle. Bei $\mathrm{Re_d} = 2 \times 10^4$ beträgt diese Vergrößerung rund 10%.

Der Wärmeübergang auf der Dellenoberfläche verbessert sich mit steigender Reynolds-Zahl. Der Nusselt-Quotient jedoch verringert sich mit steigender Reynolds-Zahl. Des Weiteren zeigt die Auswertung der Experimente, dass der Einfluss der vorderen Delle mit steigender Reynolds-Zahl sinkt. Andere Parameter, wie die Einlasstemperatur und die Wärmestromdichte, zeigen nur einen begrenzten Einfluss auf die Wärmeübertragung der Dellenoberfläche.

Die zeitliche Verteilung der Temperatur zeigt, dass bei Reynolds-Zahlen größer als 10000 ein hochfrequenter Wechsel zwischen zwei symmetrischen Strömungskonfigurationen erfolgt. Ein Vergleich zeigt, dass dieser Wechsel sechs symmetrisch verteilte Temperatur-Teilbereiche in der Delle und stromabwärts beeinflusst.

Table of Contents

Nomenclature

Roman Symbols

Symbol	Description	Unit
A	Resolution	[mm/pixel]
C_1, C_2, C_3, and C_4	Calibration matrixes	[−]
d	Circle of confusion	[mm]
D_d	Dimple print diameter	[mm]
D_h	Hydraulic diameter	[mm]
f	Frequency	[Hz]
F	Focal ratio	[−]
f_E	Friction factor	[−]
$f_\mathrm{E,pl}$	Friction factor of plane surface	[−]
$f_\mathrm{E,str}$	Friction factor of structured surface	[−]
f_s	Concavity area density	[−]
h	Channel height	[mm]
I	Electric current	[A]
I	Radiation intensity	[W]
I_B	Black-body-radiation intensity	[W·m^{-2}]
$I_\mathrm{B,med}$	Black-body-radiation intensity from media	[W·m^{-2}]
$I_\mathrm{B,ob}$	Black-body-radiation intensity from object	[W·m^{-2}]
$I_\mathrm{B,amb}$	Black-body-radiation intensity from ambient	[W·m^{-2}]
I_IR	Recorded IR intensity	[−]
$I_\mathrm{IR,cal}$	Recorded IR intensity in calibration	[−]

Symbol	Description	Unit
i, j	Streamwise and spanwise pixel element number, respectively	[−]
L_{f}	Focus length	[mm]
L_{ob}	Distance between lens and objective	[mm]
M_{B}	Spectral radiance from a black body	$[\mathrm{W{\cdot}m^{-2}{\cdot}m^{-1}}]$
M_{Gray}	Spectral radiance from a gray body	$[\mathrm{W{\cdot}m^{-2}{\cdot}m^{-1}}]$
P	Wetted perimeter	[mm]
P	Power of Joule heating	[W]
$\dot{q}$	Heat flux	$[\mathrm{kW{\cdot}m^{-2}}]$
$\dot{Q}_{\mathrm{d}}$	Heat load of dimpled surface	[W]
$\dot{Q}_{\mathrm{pl}}$	Heat load of plane surface	[W]
$\dot{Q}$	Heat flow	[W]
$\dot{Q}_{\mathrm{c}}$	Heat flow due to the cooling of the thermostat	[W]
$\dot{Q}_{\mathrm{h,1}}$ and $\dot{Q}_{\mathrm{h,2}}$	Heat flow from the heating parts	[W]
$\dot{Q}_{\mathrm{loss,1}}$ and $\dot{Q}_{\mathrm{loss,2}}$	Heat losses from the Joule heating and fluid to the environment, respectively	[W]
R	Wall curvature radius	[m]
R	Thermal resistance	$[\mathrm{K{\cdot}W^{-1}}]$
s_1 and s_2	Cross sections of inlet tubes	$[\mathrm{mm^2}]$
s_{c}	Cross section of the channel	$[\mathrm{mm^2}]$
s_{d}	Area of dimple surface	$[\mathrm{mm^2}]$
s_{dp}	Area of the dimple printing region	$[\mathrm{mm^2}]$
s_{heating}	Heating surface area	$[\mathrm{mm^2}]$
t	Dimple depth	[mm]
t_{BC}	Thickness between wall B and wall C	[mm]
t	Time	[s]
T	Temperature	[K]
T_{air}	Air temperature	[°C]
$\overline{T}_{\mathrm{span}}$	Spanwise-mean temperature	[°C]
$\overline{\overline{T}}$	Area-mean temperature	[°C]
T_{avg}	Time-averaged wall temperature	[°C]
T_{flow}	Flow temperature	[°C]
T_{in}	Inlet flow temperature	[°C]

Symbol	Description	Unit
$T_{\mathrm{i,cal}}$	Inlet flow temperature during calibration	[°C]
$T_{\mathrm{o,cal}}$	Outlet flow temperature during calibration	[°C]
T_{tran}	Wall temperature in transient case	[°C]
T_{w}	Wall temperature	[°C]
U	Electric voltage	[V]
U_0	Mean flow velocity	$[\mathrm{m \cdot s^{-1}}]$
V	Flow rate	$[\mathrm{l \cdot min^{-1}}]$
X	Coordinate in streamwise direction	[mm]
Z	Coordinate in spanwise direction	[mm]

Greek Symbols

Symbol	Description	Unit
α	Heat transfer coefficient	$[\mathrm{W \cdot m^{-2} \cdot K^{-1}}]$
β_1 and β_2	Characteristic angles	[°]
δ	Uncertainty of temperature measurement	[K]
δ^{**}	Momentum boundary-layer thickness	[m]
δ_{w}	Measurement uncertainty of wall temperature	[K]
δ_{TC}	Measurement uncertainty of thermocouple	[K]
δ_{C}	Measurement uncertainty of IR camera	[K]
δ_{fit}	Uncertainty of the least square method	[K]
Δ	Difference	[−]
Δ_{dimple}	Area difference	$[\mathrm{mm^2}]$
$\Delta\mathrm{Nu}$	Nusselt number difference	[−]
$\Delta\mathrm{T}$	Temperature difference	[K]
$\Delta\mathrm{t}$	Time interval	[s]
ε	Asymmetric ratio	[−]
Φ	Characteristic angle of the asymmetric dimple	[°]
Ψ	Characteristic factor	[−]
λ	Wavelength	[m]
λ_{max}	Peak wavelength	[µm]
λ	Thermal conductivity	$[\mathrm{W \cdot m^{-1} \cdot K^{-1}}]$
ν	Kinematic viscosity	$[\mathrm{m^2 \cdot s^{-1}}]$

Symbol	Description	Unit
ξ	Surface factor	[–]
ϵ	Emissivity	[–]
τ	Transmittance	[–]
ρ	Reflectivity	[–]

Dimensionless Groups

Symbol	Description
Gr	Grashof number
Nu	Nusselt number
$\mathrm{Nu}_{\mathrm{avg}}$	Time-averaged Nusselt number
Nu_{∞}	Nusselt number for fully developed flow
Nu_{d}	Nusselt number on the dimpled surface
$\mathrm{Nu}_{\mathrm{pl}}$	Nusselt number on the plane/reference surface
Nu_{x}	Streamwise Nusselt number
$\mathrm{Nu}_{\mathrm{str}}$	Nusselt number of structured surface
$\mathrm{Nu}_{\mathrm{tran}}$	Nusselt number in the transient case
$\overline{\mathrm{Nu}}_{\mathrm{span}}$	Spanwise mean Nusselt number
$\overline{\overline{\mathrm{Nu}}}_{\mathrm{d}}$	Area-mean Nusselt number on dimpled surface
$\overline{\overline{\mathrm{Nu}}}_{\mathrm{dimple}}$	Area-mean Nusselt number on dimple region
$\overline{\overline{\mathrm{Nu}}}_{\mathrm{e}}$	Area-mean Nusselt number of an empirical equation
$\overline{\overline{\mathrm{Nu}}}_{\mathrm{pl}}$	Area-mean Nusselt number on plane surface
$\overline{\overline{\mathrm{Nu}}}_{\mathrm{ref}}$	Area-mean Nusselt number on reference surface
$\overline{\overline{\mathrm{Nu}}}_{\mathrm{str}}$	Area-mean Nusselt number on structured surface
$\overline{\overline{\mathrm{Nu}}}_{\mathrm{wake}}$	Area-mean Nusselt number on the wake region
Pr	Prandtl number
Ra	Rayleigh number
Re_{d}	Reynolds number based on the dimple print diameter
Re_{h}	Reynolds number based on the hydraulic diameter
Re_{x}	Streamwise Reynolds number
St	Stanton number
$\overline{\overline{\mathrm{St}}}_{\mathrm{d}}$	Area-mean Stanton number on dimpled surface
$\overline{\overline{\mathrm{St}}}_{\mathrm{pl}}$	Area-mean Stanton number on the plane surface

Abbreviations

Abbr.	Description
DAQ	Data acquisition
DOF	Depth of field
FOV	Field of view
IR	Infrared
ITO	Indium tin oxide
LDA	Laser Doppler anemometry
LES	Large eddy simulation
LIF	Laser-induced fluorescence
LWIR	Long-wavelength infrared
MWIR	Middle-wavelength infrared
NETD	Mean noise equivalent temperature difference
PIV	Particle image velocimetry
PVD	Physical vapor deposition
RANS	Reynolds-averaged Navier–Stokes equations
RTD	Resistance temperature detector
TC	Thermocouple
TLC	Transient liquid crystal

Subscripts and superscripts

Symbol	Description
amb	Ambient
avg	Averaged value in time
B	Black body
c	Cooling/Channel
C	Camera
cal	Calibration
d	Dimple
dp	Dimple printing region
e	Empirical equation
f	Focus
fit	Regression

Symbol	Description
Gray	Gray body
h	Hydraulic parameter based on the channel geometry
h	Heating
in/i	Inlet
IR	Infrared image
Loss	Heat loss
max	Infrared image
med	Media
o	Outlet
ob	Object
pl	Plane surface
ref	Reference surface
span	Spanwise
TC	Thermocouple
tran	Transient value
w	Wall
x	Streamwise
∞	Fully developed flow
¯	Mean value
=	Area mean value
**	Indicator of momentum thickness

Chapter 1

Introduction

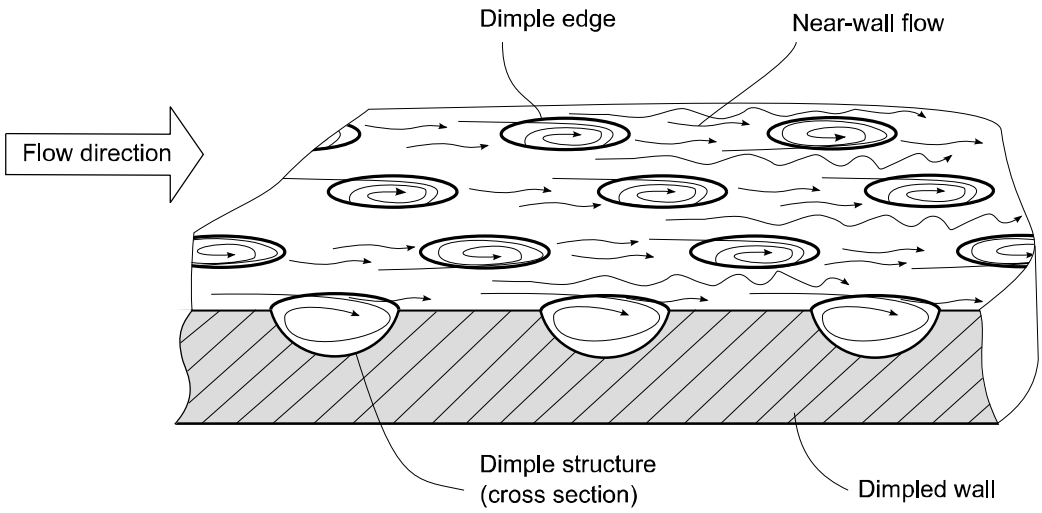

Fig. 1.1: Schematic of using dimple structures in a channel wall to enhance heat transfer.

Convective heat transfer at a solid-liquid or solid-gas interface is widely encountered in many industrial applications. For instance, in the electronic cooling, this physical phenomenon determines the performance of the cooling technologies using air or water as coolant, such as fan-cooled heat sinks for CPUs and large power LEDs, liquid cooled minichannels heat sink, etc. [13, 71, 75]. The same process also plays an important role in air conditioning and heat pumps, in which convective heat transfer on surfaces of evaporator or condenser determines the efficiency of the equipment [6, 66]. Accompanied by the rising demands on energy conservation,

parts miniaturization and costs, the development in the enhancement technology for convective heat transfer is becoming more and more significant. As an example, the internal cooling of a turbine blade is a crucial technique for developing more powerful and efficient turbine engines [24, 87].

In the past decades, various passive enhancement methods, such as fins, ribs, surface roughness, wire coils, twisted tapes, and baffles, have been employed in the industry [49, 50, 58, 59]. Because of the growth of a momentum and thermal boundary layer at the interface, the Nusselt number ratio, which is the comparison between Nusselt numbers on structured surface and plane surface (Nu_{str}/Nu_{pl}), reduces along the flow direction. Therefore, these methods greatly enhance the heat transfer by thinning, breaking or redeveloping the boundary layer and introducing the mixing of the liquid in the main flow and in the boundary layer. Furthermore, in structures like fins, the enlargement of the heat transfer area is also a reason for the intensification. However, a crucial defect of these methods is that a larger flow resistance is generated along with the heat transfer enhancement [52, 55, 87]. Thus, the benefit of the higher heat transfer is minimized by providing more energy to pumping power for maintaining a certain flow rate. Again in the case of the internal cooling of the turbine blade, it can be quite difficult to apply a conventional enhancement method to increase the Nusselt number ratio in the cooling passages with a lower coolant flow rate [65].

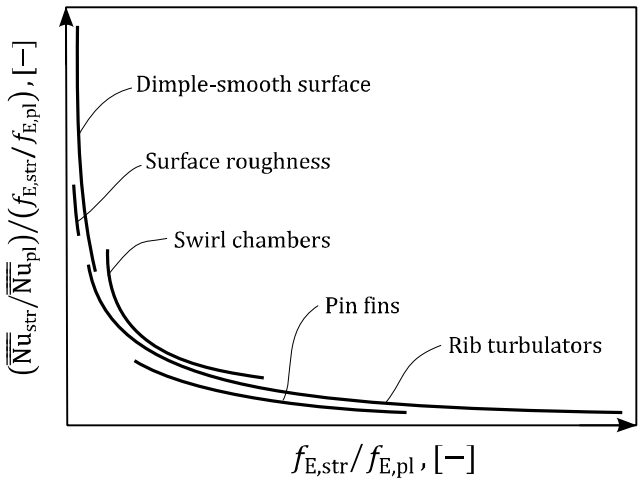

Fig. 1.2: Comparison of performance parameters of different heat transfer enhancement techniques (according to [55]).

A structure of concave dimples processed on a heat transfer surface was reported to enhance the heat transfer with only a moderate increase of the flow resistance [51]. Meanwhile, this structure is mostly applied as an enhancement element spread on the surface in an array formation (see Fig. 1.1). The performance parameter ($(\overline{\overline{Nu}}_{str}/\overline{\overline{Nu}}_{pl})/(f_{E,str}/f_{E,pl})$, see section 2.1.2) of different enhancement techniques are compared in various friction factors ($f_{E,str}/f_{E,pl}$) and the value

dimpled surface is the highest compared to the other methods (shown in Fig. 1.2). The dimple structure was first applied to the surface of golf balls to reduce the drag during their flight in the air [61]. Afterwards, the heat transfer enhancement effect was discovered in studies on cylindrical dimples [26, 82]. Later, it was found that the enhancement ability of spherical dimples is much higher comparatively [92]. Subsequent to this discovery, a great body of experimental and numerical simulation investigations, regarding the flow structures and the effects of the dimple geometry on heat transfer were carried out [51, 88]. After the year 2000, due to the great evolution of the computational technology, the study of the heat transfer mechanism on a dimple structure was significantly promoted by numerical simulations, predicting the local flow structures and the heat transfer caused by the dynamic vortex at quite a high resolution [16, 30, 45]. Meanwhile, many high-resolution measurement technologies were adopted for studying the heat transfer on dimple array surfaces [48, 62, 95]. However, due to the limits of the experimental technology, detailed investigations on the heat transfer mechanism of such structures, which are linked to the unsteady and local complex flow structure, are still insufficient [51].

At the institute of Technical Thermodynamics at TU Darmstadt, high-resolution temperature measurement technologies, such as the IR thermography, TLC (Transient Liquid Crystal) and LIF (Laser-Induced Fluorescence) methods had been used for many thermal fluid experiments at small scales [64, 85, 86]. IR thermography had been applied in studies on pool boiling and three-phase contact lines with a spatial and temporal resolution on the plane surface of up to 50 μm and 1 ms, respectively. In this study, the similar method was employed to investigate the heat transfer on dimpled surface in a fully developed turbulent flow. Influences such as Reynolds number, inlet flow temperature, heat flux, and upstream dimple were considered in the investigation. Furthermore, the Nusselt number distributions measured from the dimpled surfaces were compared to a non-structured plane surface with identical size to quantify the performance of the enhancement by Nusselt number ratios.

As a result, heat transfer enhancement of the dimple structures was observed in this study. Due to the existence of transverse vortex structures, the enhancement area took the rear half of the dimple surface and in its wake, while on the front part of the dimple the heat transfers are equal or lower than those of the flat surface. Furthermore, temperature distributions are found related to the flow structures in and downstream of the dimple structure. Local temperature fluctuations related to the switching of the flows were recorded in different locations inside the dimple at higher Reynolds numbers. Nevertheless, these transient fluctuations have little influence on the mean heat transfer of the dimpled surface. Finally, an increasing Nusselt number ratio was observed in the downstream dimple.

Chapter 2

State of the Art

In this section, methods and principles for enhancing heat transfer in single-phase flow are introduced in section 2.1. Studies on dimple structures including the flow structure and heat transfer are reviewed in section 2.2. As the basis of the experimental method, IR thermography and its applications in thermo-fluid studies are presented in section 2.3. A summary concludes this discussion in section 2.4.

2.1 Heat Transfer Enhancement in Single Phase Flow

As mentioned in the introduction, the heat transfer enhancement at solid-liquid/solid-gaseous interface is the focus of this study. In this section, the basic principles for heat transfer enhancement are discussed in general. Afterwards, various types of passive enhancement technologies are introduced. Since the enhancement is evaluated in most cases through a comparison with a plane surface, heat transfer on this non-structured surface scenario will be the first subject at the beginning.

2.1.1 Convective Heat Transfer on a Plane Surface

On a plane surface in a single-phase flow, convective heat transfer is majorly influenced by the flow structures characterized by the hydraulic boundary layer and its development. It is quite well-known that as shown in Fig. 2.1 the hydraulic boundary layer along the surface can be divided into two types: a laminar boundary layer and a turbulent boundary layer. Since in the turbulent boundary layer, turbulent pulsations of the flows intensify the mixing between the main flow and the boundary layer, heat transfer in this type of boundary layer is much better

than in the laminar boundary layer. In the internal flow, hydraulic boundary layers from the surrounded walls form a fully developed flow regime, such as laminar regime and turbulent regime. As a consequence of heat transfer in the near wall flows, thermal boundary layer is generated along the wall and develops with the hydraulic boundary layer. Since the thermal boundary layer is quite thin near the leading edge of the heating surface, the heat transfer coefficient is considerably high in this location. However, following the flow direction, it drops sharply to a much lower value in the thermally fully developed region [47]. Namely, without any enhancement method, the heat transfer on the plane surface just decreases abruptly to a poor level. In the turbulent boundary layer, thermal resistance of the interface is mainly due to the viscous sublayer, which is a thin layer near the wall acting similarly to laminar boundary layer.

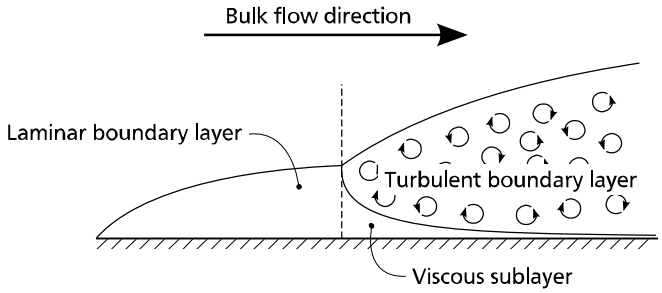

Fig. 2.1: Schematic of the hydraulic boundary layer on the plane surface (according to [8]).

In many studies for evaluating heat transfer enhancement of a structured surface, heat transfer of fully developed turbulent tube flow, described by the Dittus-Boelter equation

$$\mathrm{Nu}_\infty = 0.023\mathrm{Re}_\mathrm{h}^{0.8}\mathrm{Pr}^{0.4}, \tag{2.1}$$

was considered as a baseline for different comparison [10, 46, 69]. In present study, due to the insufficient empirical correlation specified for the case of asymmetric heating in a rectangular channel with thermally developing flow, baseline Nusselt numbers were collected from the experiment.

2.1.2 Methods for Heat Transfer Enhancement

The aim of heat transfer enhancement is trying to reduce the thermal resistance at the interface as much as possible. In this case, the enhancement can be achieved by either enlarging the heat transfer area or increasing the heat transfer coefficient. As mentioned in the previous section, heat transfer in turbulent flow can be enhanced by introducing turbulence in the boundary layer, destroying the viscous boundary layer to enhance the mixing, or interrupting the development of the thermal boundary layer. Different enhancement methods are categorized as passive methods and active methods, depending on whether the external energy is introduced. In this study, the focus is placed on passive enhancement methods in single-phase flows.

As suggested by Bergles [2], passive techniques include rough surfaces, extended surfaces, displacement enhancement, swirl flow devices, and coiled tubes. The method of rough surfaces, like the wavy wall of the corrugated tubes shown in Fig. 2.2 (a), vortex generators, grooves, and so on, enhances heat transfer by interrupting the thermal boundary layer periodically as well as causing secondary flows to influence the boundary layer behind the structure. The extended surface method, such as the fins and pins, is processed on the heat surface to enlarge the heat transfer area. The displacement enhancement method promotes heat transfer by inserting a wire matrix into the channel (Fig. 2.2(b)) which diverts the flow in the center of the channel towards the walls and enhances the mixing in the boundary layer. Due to this effect, the different colored dyes on the wall in a laminar flow are transported to the region near the tube center by the displacement effect in the insert section. Finally, the augmentation effect of the swirl flow device, like various type of swirl tapes inserted into the circular tube (Fig. 2.2(c)), and coiled tubes is executed by the secondary flows, which is generated by the rotating flows. Most enhancement techniques are available in both laminar and turbulent flows. However, rough surfaces are only suitable when the element of roughness extends beyond the laminar sublayer and are therefore only effective in turbulent flows [50]. Similar to the corrugated tubes, dimple structure can be considered as a kind of rough surface.

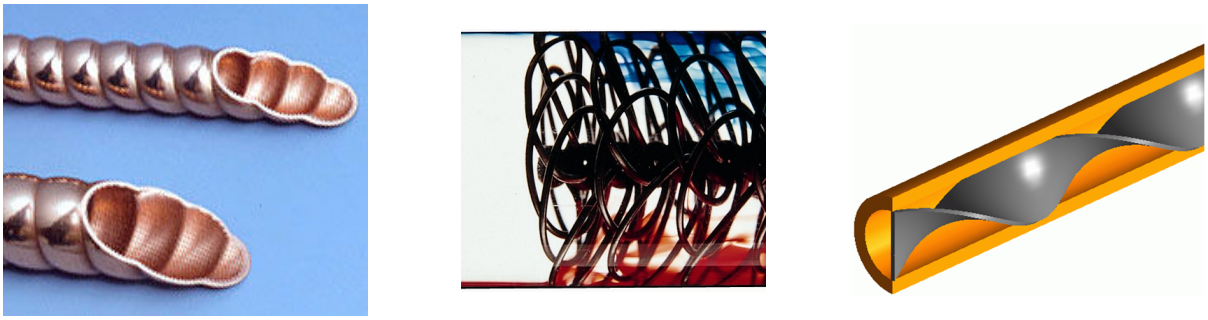

(a) (b) (c)

Fig. 2.2: Applications of heat transfer enhancement techniques: (a) corrugated tubes[1], (b) matrix elements in a tube[2], (c) swirl tape inserts in a circular tube[3].

In order to evaluate the performance of different enhancement methods, several parameters were suggested and applied in the previous studies [2, 55]. The most direct parameter is the Nusselt number ratio (Nu_{str}/Nu_{pl}), which compares the heat transfer on the enhanced surface to the one on the non-structured surface (plane surface) under the same conditions. As reported by

[1] FURUKAWA ELECTRIC Co. Ltd.

[2] hiTRAN Matrix Elements, Cal Gavin Ltd.

[3] Naka fusion institute, JAEA.

Ligrani et al. [55], the rib turbulators and swirl chambers achieve a high enhancement with a Nusselt number ratio of up to nearly 5.8. On the other hand, the Nusselt number ratios of the dimpled surfaces (dimple-smooth arrangements) are quite lower, at values between 1.8 and 3.4. Nevertheless, as mentioned in the introduction, conventional enhancement methods generate considerably higher flow resistance, described by the friction factor ratio ($f_E/f_{\mathrm{E,pl}}$). In this case, it was proposed to use the thermal-hydraulic performance to assess the enhancement by combining the friction factor with heat transfer [2]. Considering that the channel with the enhancement structures has the same cross section and length of heating area as on one featuring plane surface, the thermal-hydraulic performance is expressed as:

$$\left(\frac{\overline{\overline{\mathrm{Nu}}}_{\mathrm{str}}}{\overline{\overline{\mathrm{Nu}}}_{\mathrm{pl}}}\right)\Big/\left(\frac{f_{\mathrm{E,str}}}{f_{\mathrm{E,pl}}}\right)^{\frac{1}{3}}. \tag{2.2}$$

This parameter indicates the effect of different enhancement methods on heat transfer at equal pumping power. Table 2.1 shows the comparison of different methods in the thermal-hydraulic performance [55]. Under the same pumping power, heat transfer performance of dimple-smooth arrangements, rib turbulators, and swirl chambers is rendered comparable. At this point, Ligrani would like to suggest a new parameter regarding the Reynolds analogy as

$$\left(\frac{\overline{\overline{\mathrm{Nu}}}_{\mathrm{str}}}{\overline{\overline{\mathrm{Nu}}}_{\mathrm{pl}}}\right)\Big/\left(\frac{f_{\mathrm{E,str}}}{f_{\mathrm{E,pl}}}\right). \tag{2.3}$$

Considering the distributions shown in Fig. 1.1, the performance of the dimple-smooth arrangement surface shows the highest value between 0.5 and 1.8. This suggests that with an equalized friction factor, the heat transfer enhancement of the dimple structure is better than other methods.

Table 2.1: Enhancement methods and performance parameters (according to [55]).

Enhancement method	$\left(\frac{\overline{\overline{\mathrm{Nu}}}_{\mathrm{str}}}{\overline{\overline{\mathrm{Nu}}}_{\mathrm{pl}}}\right)\Big/\left(\frac{f_{\mathrm{E,str}}}{f_{\mathrm{E,pl}}}\right)^{\frac{1}{3}}$	$\left(\frac{\overline{\overline{\mathrm{Nu}}}_{\mathrm{str}}}{\overline{\overline{\mathrm{Nu}}}_{\mathrm{pl}}}\right)\Big/\left(\frac{f_{\mathrm{E,str}}}{f_{\mathrm{E,pl}}}\right)$
Dimple-smooth surface	$1.3-2.4$	$0.5-1.8$
Surface roughness	$1.2-1.3$	$0.8-1.1$
Swirl chambers	$1.5-2.6$	$0.2-0.8$
Pin fins	$0.7-1.8$	$0.1-0.4$
Rib turbulators	$0.8-2.2$	$0.1-1.1$

2.2 Heat Transfer Enhancement by Dimple Structure

Generally speaking, the heat transfer enhancement of the dimple structure is intensified by the separated flow-induced vortex and turbulent structures in and downstream of the structure [31, 51]. This process on the surface is dynamic and three-dimensionally distributed. In this section, the behavior of the flows on the dimpled surface will be presented first, followed by the introduction of heat transfer studies. The last section will focus on factors influencing the performance of dimple structures.

2.2.1 Flow Structures

Boundary Layer Separation

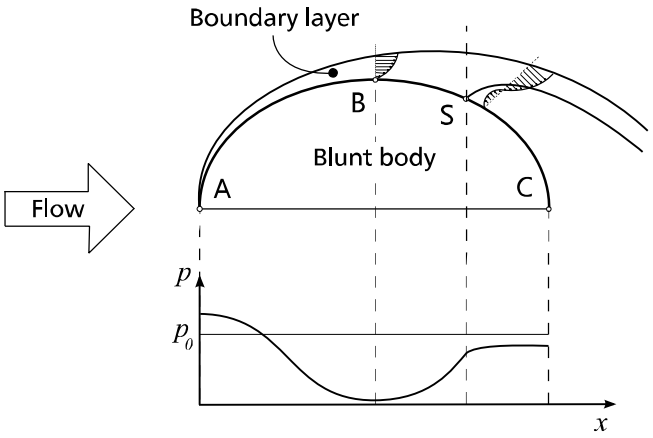

Fig. 2.3: Flow separation on a bluff body (according to Schlichting and Gersten [80]).

The boundary layer separation happens when a viscous flow passes a solid surface at a condition shown in Fig. 2.3. The boundary layer is formed on the surface at point A and further develops downstream along the solid body's surface. Then, a maximum flow pressure is generated here due to the flow suddenly being stopped by the body. In this case, flows in the boundary layer accelerate in the area between points A and B with a decreasing pressure gradient. In other words, the potential energy of the flows is transformed into kinetic energy in this region. After point B, an increasing adverse pressure gradient causes the decelerations in the boundary layer flows. Consequently, since the extra energy is taken up by the frictions in the boundary layer, the flow, in an ideal situation should stop at point C, where the entire kinetic energy is transferred to the potential energy again, comes to a standstill at point S between points B and C. Carried off by the main flow, it forms a separated boundary layer. The separation primarily depends on the body geometry, especially when there is a sharp change in shape [80]. In internal flows, expansion of channel cross section in flow direction can cause a separation as well.

Steady Vortex Structures

In the internal flow, after separation from the surface, the boundary layer becomes a free shear layer in the flow. In the case shown in Fig. 2.4, a shear layer, generated by the separation in the backward facing step at point A, reattaches to the wall at point R and is split into one stream going upstream and one stream going downstream in the wake of the structure [93]. In this case, with point R dividing both, the wake is separated into two regions: the recirculation region and the relaxation region. In the recirculation region, steady vortex structures are generated under certain conditions. On the other hand, the flow is reestablished in the relaxation region with a decreasing level of turbulence intensity [72, 93]. Usually, the first vortex from the left side of point R is rotating clockwise, while the other one is turning anticlockwise. Due to the shape of the step showing no spanwise change, like the grooves and the ribs, the vortex structure is nearly the same and can be considered two-dimensional.

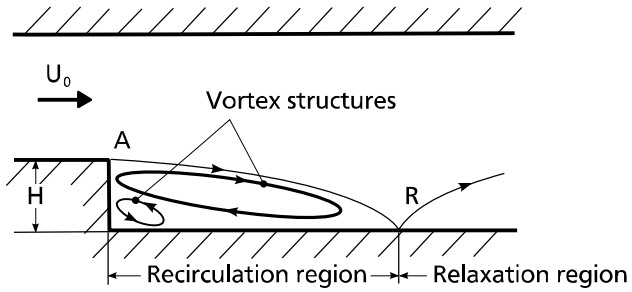

Fig. 2.4: Flow structures induced by a backward-facing step (according to Terekhov et al. [93]).

In case of that body showing a sudden change both streamwise and spanwise, such as occurs in pin structures, delta-winglets, and so on, the separation could cause three-dimensional vortices. As an example, in the case of a vortex generated by a pin structure, reported by Délery [14], except for the two-dimensional vortex structure generated downstream of the pin's middle part, longitudinal vortices are formed at each end of the cylinder structure. Particularly at the bottom of the leading surface of the pin structure, a horseshoe vortex is generated due to the separation of the flow just upstream of the structure. Consequently, the vortex develops near the bottom around the pin body and thus turns into the lower longitudinal vortices in the wake.

Vortex Oscillations

Another characteristic of the vortex is spontaneous oscillation. A classic example is the Kármán vortex street, which is a series of vortices shed periodically from a cylinder [94]. This type of oscillation is transformed from a steady and symmetric vortex pair upon exceeding a critical Reynolds number [19]. Meanwhile, the amplitude and the frequency of the shedding are increased the higher the Reynolds number is.

Flow Structures on the Dimpled Surface

The first study on flow structures on a dimpled surface was reported by Snedeker and Dup [81] in 1966. By placing a movable tuft in different locations inside the dimple, a transverse vortex structure was visualized. An alternation of the vortex axis in symmetric positions was observed in the study as well. In 1983, Hiwada et al. [26] studied the flow structures in cylindrical dimples and identified the alternation of the vortex in a similar manner by observing the pressure fluctuations at the points symmetrically located at the bottom of the structure. In this regard, the word 'switching' was first used. Since the 1980s, many studies were carried out by investigators in Russia regarding the formation, mechanism, and influence factors, such as the dimple geometry, Reynolds number, flow turbulence intensity, of the vortex structures [88]. Terekhov et al. [90-92] investigated the flow structures in a single dimpled surface by tracking the hydrogen bubbles and the air bubbles, LDA method (laser Doppler anemometry method) as well as soot-oil visualization technique. These studies determine many characters of the oscillation behavior of the vortex in the dimpled surface. Since 1994, great numbers of simulations were reported by Isaev et al. [29, 31-33, 37, 38], predicting the detailed flow structures on the dimpled surface with various dimple geometries and Reynolds numbers. In 2001, Ligrani et al. [54, 55] used the smoke stream to visualize the flow structure above the concavity. In the study, mushroom-like vortex structures were discovered in the spanwise plane of the dimpled surface in low Reynolds numbers. In recent years, the LES method was adopted by researches to study the instantaneous flow structure inside the dimple [16, 17, 45, 46]. Transient analyses and measurements were carried out to determine the oscillation behavior of the dimple flows. Furthermore, the particle image velocimetry (PIV) method was introduced to visualize the velocity fields in the dimple structure [68]. Based on the discoveries of the previous studies, the flow structures on the dimpled surface and their oscillation characters will be presented subsequently in this section.

Similar to the case of the backward facing step, the flow visualization reported by Terekhov et al. [88] shows that on the center plane of the dimple in streamwise view, the separated flow detached at point 1 to become a free shear layer across the dimple region (Fig. 2.5). After reattaching on the rear surface near the dimple's edge, the flow becomes both an upwash flow at point 3 and a recirculating flow inside the dimple, forming the vortex structure. However, different from the case of backward facing step, only one single vortex merged in the recirculation region. According to Presser [73], the form of shear layer depends on the Reynolds number. Here, based on different characteristic length, channel Reynolds number ($\mathrm{Re_h}$) and dimple Reynolds number ($\mathrm{Re_d}$) are defined as:

$$\mathrm{Re_h} = \frac{U_0 D_\mathrm{h}}{\nu} \text{ and } \mathrm{Re_d} = \frac{U_0 D_\mathrm{d}}{\nu}, \tag{2.4}$$

where $D_h = 4s_c/P$ is the hydraulic diameter of the channel. At $\mathrm{Re_h} < 2300$, the shear layer is continuous and stable across the dimple region. However, if $\mathrm{Re_h} > 2300$ and $\mathrm{Re_d} < 1 \times 10^4$, the shear layer starts to decay in region 2. Then, reattached flows become unsteady, showing strong turbulence. Furthermore, the upwash flow leaving the dimple intensifies the mixing in the wake.

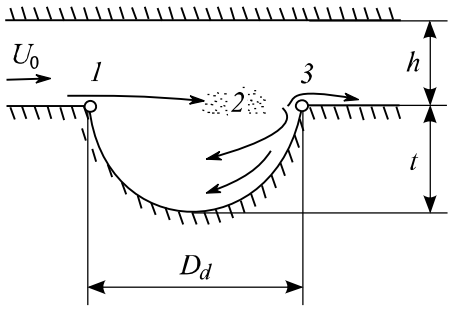

Fig. 2.5: A diagram of flow structures in the central plane of the dimple (according to [73, 88]).

Furthermore, according to the introduction of Terekhov et al. [88], the dimple depth is a condition of flow separation. At the relative dimple depths $t/D_\mathrm{d} > 0.2$, separation starts. When $t/D_\mathrm{d} < 0.1$, the flow is similar to a diffuser-confuser flow without separation. In this flow, some micro-unstable separations are generated if the dimple either has a rounded edge no larger than the dimple depth or has a sharp edge with an angle between the tangential line of the dimple surface and the plane surface of more than 6°.

Due to the influence of the dimple structure, the vortex is a three-dimensional structure [31]. In the symmetric formation, two foci are located symmetrically in the front half (upstream half) of the dimple with respect to the streamwise central plane. In this case, the flow streams on the wall are trapped by the focus on each side and move to the focus center. There, a spiral jet is formed and detaches from the dimple wall in the above flow [39]. Finally, the jets generated from each side create a horseshoe vortex in the front half of the dimple [88]. Under certain conditions, such as increasing the flow velocity, the vortex becomes asymmetric with one side larger than the other. The jet from the larger vortex side tries to 'push' the jet on the other side out of the dimple and eventually forms a transverse single-cell vortex called a tornado-like vortex [88]. Both experiment and simulation found that the axis of this type of vortex has an angle around 45° to the flow direction [31, 91].

Spontaneous oscillations of the vortex in the dimple were observed in many flow visualization studies [54, 81, 88]. According to Terekhov et al. [91], the behavior of the oscillation consisted of both a 'high frequency' component as well as a 'low frequency' component. The high-frequency oscillation, usually has a frequency of $f > 1$ Hz, was observed in all the investigated

flow velocities and dimple geometries. On the other hand, the low frequency oscillation at $f <$ 1 Hz was only observed in transitional or turbulent flow with $\mathrm{Re_d} > 1 \times 10^4$.

The visualization by tracing the bubbles in the flow shows that at a flow velocity $U_0 \leq$ 0.2 m/s ($\mathrm{Re_d} \leq 1 \times 10^4$) [91], the vortex in the dimple was symmetric and presented a high frequency oscillation. In this process, periodic ejections of the flows in the dimple to the outside were observed leading to a flow structure above the dimple similar to the Kármán vortex street. Similar flow structures were observed by Ligrani et al. [54]. The visualization was executed by using horizontal smoke wires in the airflow over a dimple array surface on a channel wall. The relative dimple depth and relative channel height are $t/D_\mathrm{d} = 0.2$ and $h/D_\mathrm{d} = 1$, respectively. At $\mathrm{Re_h} = 3800$, a periodic ejection of the upwash flows was observed in mushroom formation with a period of 83 ms [56]. These mushroom-shaped vortices are formed by the counter-ascending circulation pairs in the dimple, which are caused by the separation flows reattaching in the dimple. When exceeding the dimple window (top plane of the dimple structure which coincides with the channel wall), these vortex pairs were stretched and removed downstream by the main flow. After that, the separated flows reattached again on the rear surface and initiated the next period of the oscillation. The frequency of the oscillation is $f = 9 - 10$ Hz at $t/D_\mathrm{d} = 0.1$ with $\mathrm{Re}_d = 3800$ and is $f = 7 - 8$ Hz at $t/D_\mathrm{d} = 0.25$ and 0.5 with $\mathrm{Re_d} = 2500$. The author also reported that at $\mathrm{Re_h} = 1250$ and $h/D_\mathrm{d} = 0.5$, two smaller vortex pairs were found adjacent to each side of the primary mushroom-shaped vortex. Along with the primary vortex, these small structures developed downstream in a similar process.

The low frequency oscillation was found in a special flow motion in the dimple structure, called the switching mode [88]. In this mode of oscillation, the asymmetric vortex alternates in a large amplitude between two symmetric flow patterns. As an example, shown in Fig. 2.6, the pink-colored dye streams ejected from three locations at the dimple's bottom wall indicate the directions of the local flows change in the switching mode at $\mathrm{Re_d} = 4 \times 10^4$ [42]. In each pattern, the colored stream is at an angle to the main flow direction, which suggests that the recirculation flow of the transverse vortex is asymmetrically distributed. Compared to each other, the angles are comparable in magnitude and exactly opposite in flow direction. This means that the vortex structures in these two patterns are symmetric to each other.

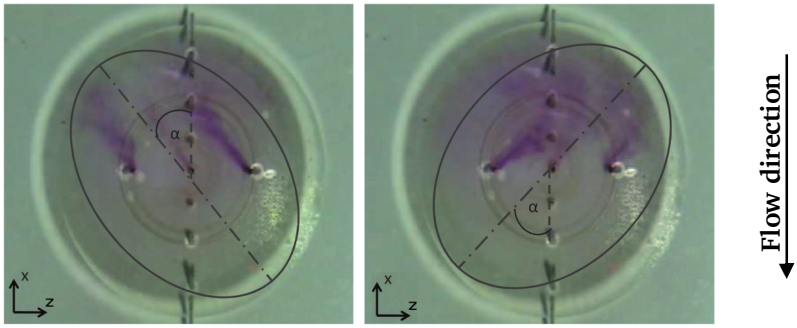

(a) (b)

Fig. 2.6: Snapshots of the flow patterns in the dimple structure at different moments in the switching mode [42]: (a) pattern I, (b) pattern II.

Terekhov et al. [91] studied the switching mode in the oscillating dimple flow by adopting the LDA. At the flow velocity of $U_0 = 0.8\ m/s$ ($\mathrm{Re_d} = 4 \times 10^4$), the switching mode was observed in a dimple with a relative depth of $t/D_\mathrm{d} = 0.26$. Furthermore, this type of oscillation combines the 'high frequency' component with $f > 1$ Hz and the 'low frequency' component with a characteristic period between $\Delta t = 5$ and 20 s. Meanwhile, the angle between the recirculating flow and the flow direction was $\pm 45°$, respectively, in each pattern of the switching mode.

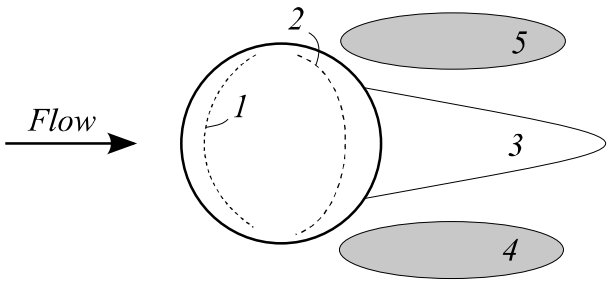

Fig. 2.7: Time-averaged flow pattern in and around the dimple structure [90].

Another investigation by the same author [90] observed a time-averaged flow pattern on the surface with a shallow dimple ($t/D_\mathrm{d} = 0.13$) at $\mathrm{Re_d} = 1.9 \times 10^5$ by using the soot-oil visualization technique in the airflow (Fig. 2.7). The arc-dashed lines 1 and 2 respectively indicate the regions of the detaching flow and the reattached flow in the dimple. Region 3, located directly downstream of the dimple, indicates the influence of the flow in the wake. Beside this region, region 4 and 5 are located symmetric to each other behind the rear dimple's edge. These regions are caused by the outgoing jet generated by the oscillating vortex in the switching mode inside the dimple [91]. Since the jet may alternate its direction from one side of the dimple to another symmetric location, it is possible that the region 4 and 5 are the accumulation of this effect in time.

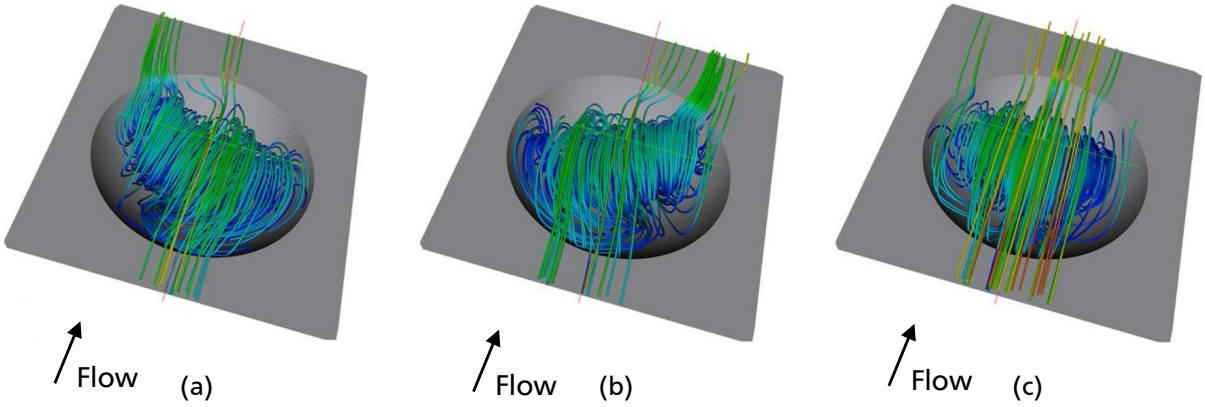

Fig. 2.8: Simulated flow structures in the dimple structure [45], (a) velocity field averaged over 1 s of real time in the interval $t = 2 - 5$ s, (b) velocity field averaged over 1 s of real time in the interval $t = 5 - 8$ s, (a) velocity field averaged over 11 s.

In numerical simulation, Turnow et al. [45] studied the flow structure in a single dimple ($t/D_\mathrm{d} = 0.26$) at $\mathrm{Re}_\mathrm{d} = 4 \times 10^4$ by large eddy simulation (LES). As the result shows in Fig. 2.8, the flow structure in the dimple with switching mode flows becomes symmetric after averaging over a sufficiently long time. In Fig. 2.8(a) and (b), velocity fields averaged in short time intervals show that the asymmetric flow is alternating from one pattern to another. The particle trajectories shows that the major outgoing flows in these two cases are asymmetrically distributed to one side of the wake, while less of the flows are located near the streamwise center plane. However, after averaging over $11s$, the flow structure becomes symmetric in the dimple and in the wake, in agreement with the distribution shown in Fig. 2.7.

2.2.2 Heat Transfer on the Dimpled Surface

The first heat transfer study for dimple structures appeared in 1972, when Presser [73] initiated the first scientific investigation into heat transfer of a dimpled surface in a channel flow. In the study, empirical correlations of the mean Nusselt number were reported from the laminar flow to the turbulent flow. Since 1990s, a great number of studies on either experiments or simulations have been published by many authors [51, 88]. Ezerskii and Shekhov [18] were the first to use IR thermography to visualize the heat flux distributions on a single dimpled surface in an airflow with various flow velocities. They observed a high frequency switching ($\Delta t \leq 1s$) of the heat flux in the dimple wake and believed this type of oscillation to be related to the flow structures on the surface. Terekhov et al. [91, 92] reported the Nusselt number distribution on a spherical dimple surface and compared the mean Nusselt number to the previous studies on cylindrical dimples with various depths. The result shows that at the relative depth of $t/D_\mathrm{d} = 0.13$, the enhancement of the dimple structure is more effective than any other cylindrical structure. The authors drew the conclusion that the enhancement mechanism of the dimple structure is due to the combination of enlarging the heat transfer area and intensifying the flows in the oscillation

regime. Since 1998, Isaev has published many simulation results on the heat transfer of dimple structures accompanied by the flow structure investigations [27, 28, 30, 31, 33, 34, 36-41]. In these studies, the relationship between the flow structure and Nusselt number distributions was presented with different numerical arrangements. Terekhov et al. [90] experimentally investigated the influence of heat transfer by placing another dimple upstream of the investigated dimple and found that the influence can only be identified in the local heat transfer while the effect on mean heat transfer values is limited. Furthermore, numerical simulation study reported by Isaev et al. [40] showed that the local heat transfer rises by increasing the number of dimple rows. Except for the detailed investigation on the heat transfer of a single dimpled surface, many authors released studies on the heat transfer of dimple arrays. In 1992 and 1993, Afanasyev et al. [3, 4] experimentally investigated the heat transfer on a dimple array surface. After that, Moon et al. [62] studied surface temperature by using the TLC technique and visualized the Nusselt number distributions on a dimple-array surface. Since year 2000, Ligrani et al. [54], Mahmood et al. [56, 57], and Burgess et al. [10, 11] have used IR thermography to study the local heat transfer of dimple array surfaces with various influence factors, such as the dimple arrangement, dimple depth, temperature ratio, Reynolds number, and channel height. Furthermore, many studies were focused on the heat transfer enhancement of the dimple structure in various applications, such as in circular tubes, rotating channels, mini-channels and curved surfaces [9, 87, 98, 101]. Some optimizations of the dimple geometry, estimation method, and combinations with other enhancement structures were proposed as well [12, 15, 16, 44, 76, 77]. In the following part, the mechanism of heat transfer will be presented, followed by a discussion of the influencing factors for heat transfer.

Heat Transfer Distributions

It is common that in two-dimensional distributions on the dimpled surface observed in the experiment, a lower heat transfer zone covers almost half of the dimple region and the local maximum can be found in a narrow region near the dimple's rear edge [56]. The similar distributions was reported in the simulation research, as well [42]. Additionally in the simulation, without the influence of the neighborhood dimples, another heat-transfer-enhanced zone is identified in the wake. These three typical zones are generated by the flow structure shown in Fig. 2.5, where a flow separated from the front dimple's edge reattaches to the dimple surface in the rear, triggering the recirculation in the dimple and the turbulence in the wake. Consequently, a strong mixing effect in the reattachment region leads to a much higher heat transfer near the rear dimple's edge. At the same time, reticulation flows rotate in the front half space of the dimple and cause a rather low heat transfer in this region. Then, in the wake, the upwash flow reacting with the main flow generates an additional turbulence in the wake,

leading to a high local heat transfer. Since the flow is developing in the wake, the heat transfer is reduced sharply in the streamwise direction, similar to that on the plane surface. Furthermore, due to the dimple geometry, the distribution is different spanwise. Especially in the wake, the heat transfer is greater in the streamwise centerline and reduced on both sides.

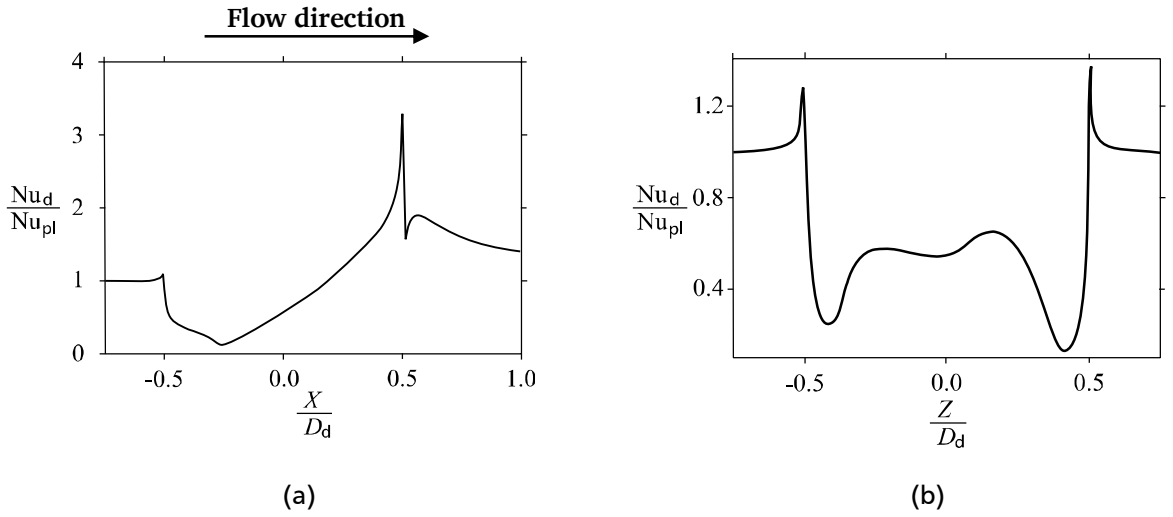

Fig. 2.9: Local Nusselt number distributions on a single-dimpled surface ($t/D_d = 0.26$, $h/D_d = 0.33$, $Re_d = 2 \times 10^4$, according to [30]: (a) distribution on the streamwise center line, (b) distribution on the spanwise centerline.

Figure 2.9 shows the typical distributions on the centerlines of a dimpled surface, as reported by Isaev et al. [30]. Streamwise, the Nusselt number ratio sharply drops just behind the front dimple's edge and is reduced to a minimum value at a distance of $0.25D_d$ to the leading edge. After this point, the heat transfer rises steeply to reach its maximum value quite close to the rear edge. In the wake, the Nusselt number gradually decreases downstream. On the spanwise centerline, the Nusselt number ratio is much lower than on the plane surface outside the dimple. Meanwhile, a higher value relative to that was found at the position around $0.3D_d$ to the dimple center.

Influencing Factors on Heat Transfer Enhancement

Generally speaking, the influencing factors of the heat transfer on dimpled surface can be classified by the effects of the flow and the geometries of channel and dimple structure. The flow effects include the Reynolds number, the turbulent intensity, and the temperature ratio. The geometry effects include the dimpled depth, size of the rounded edge, dimple shape, and upstream dimple. The effects of these factors will be described in more details in this section.

Considered in most investigations, the effect of the Reynolds number is the most important factor. Similar to equation 2.1, the correlation of the heat transfer parameters, such as the Nusselt number, Stanton number, and Nusselt number ratio are described by Reynolds number.

As the correlation will be introduced in the following part, only the general effect is taken into consideration at this point. According to the simulation reported by Isaev et al. [30], in turbulent flow ($\mathrm{Re_d} = 2 \times 10^4 - 6 \times 10^4$), there is less influence from the Reynolds number on local heat transfer enhancement on the dimple surface than in the wake, where the 'tongue'-like regions decrease in length but grow wider near the dimple's edge as the Reynolds number increases. The turbulent intensity of the inlet flow has a strong influence on both the local heat transfer coefficient and the flow structure [88]. The heat transfer is only 15% higher than the plane surface as the inlet flow is low turbulent. In higher turbulent case, as the flow inside dimple could become a tornado-like vortex, heat transfer increases to 70% higher. The influence of the temperature ratio studied by Mahmood et al. [56] within a temperature ratio $T_{\mathrm{in}}/T_{\mathrm{w}}$ range from 0.68 to 0.94 showed that the heat transfer was enhanced when this ratio is reduced.

Regarding the influence of the dimple depth, Terekhov et al. [89] studied the heat transfer of dimple structures with various depths ($t/D_{\mathrm{d}} = 0.13,\ 0.26$ and 0.5). The results show that the mean heat transfer rate increases along with increasing dimple depth and reaches a maximum at $t/D_{\mathrm{d}} = 0.5$. The influence on the Nusselt number ratio distributions were revealed by the same author in another investigation [92]. Since the flow structure is influenced by the dimple depth, the heat transfer distribution in the dimple is affected as well. Streamwise, the local maximum found near the rear edge is much higher than the value of a small depth. However, on the spanwise centerline, the local Nusselt number ratio is either equal or slightly lower than in a shallow dimple. This effect was found in the simulation as well [30]. Furthermore, the Nusselt number ratio in the deep dimple's wake is also higher than that of the shallow dimple at the same location. This shows that instability in the boundary layers is significantly stronger in the deep dimple's wake.

Terekhov et al. [89] studied the effect of the round edge. A comparison to a dimple with a sharp edge showed that the heat transfer enhancement of the dimple with rounded edges is stronger. Turnow et al. [45] numerically studied the enhancement by changing the round radius of a spherical dimple with a depth of $t/D_{\mathrm{d}} = 0.28$ (Fig. 2.10). As a result, the dimple has a better Nusselt number ratio than the one with a sharp edge at a radius up to $r/D_{\mathrm{d}} = 0.4$. Meanwhile, an optimal round radius at $r/D_{\mathrm{d}} = 0.25$ was discovered to yield the highest Nusselt number ratio around 1.1. By considering the friction factor, the highest performance parameter was found at the maximum radius. Simulation results showed that certain forms of asymmetrical dimples are more effective than the conventional spherical dimple. Isaev et al. [36, 39] studied a type of asymmetric in which one half of the dimple radius is reduced by a value ε. The result showed that at $\varepsilon = 0.5$, the heat load rate ($Q_{\mathrm{d}}/Q_{\mathrm{pl}}$) is higher than that of a spherical dimple ($\varepsilon = 0$). In this case, heat transfer is enhanced by using this shape, due to the vortex motion in the fluid

increasing [36], generated by a single asymmetrical tornado-like vortex in this asymmetric structure [32, 33]. A different asymmetric dimple, which is in an arena shape, was proposed by Isaev et al. [40] for creating a single tornado-like vortex in the dimple. Turnow et al. [45] studied the effect of the angle Φ of this structure, which is between the axis of this structure to the flow direction (Fig. 2.10). The result showed that both the Nusselt number ratio and the performance parameter is higher than the case of the spherical dimple. Additionally, an optimal angle was discovered at $\Phi = 60^{\circ}$ for both parameters.

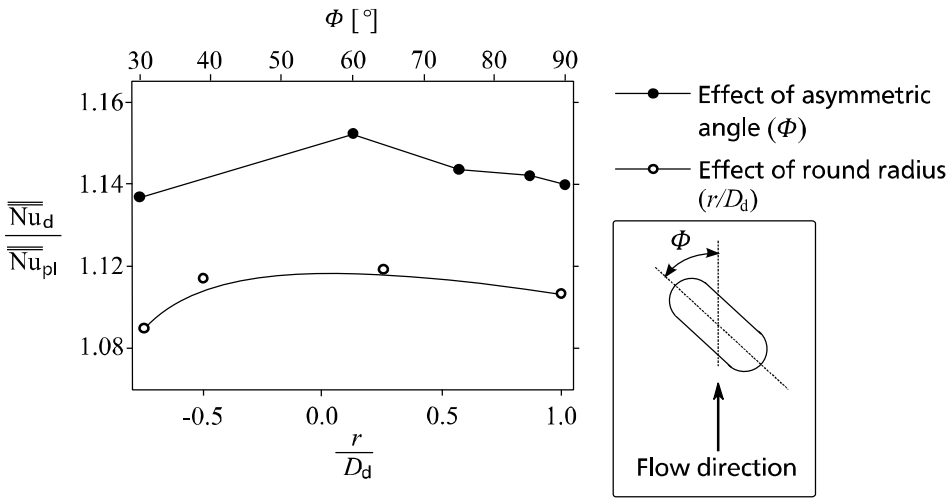

Fig. 2.10: Effects of the dimple parameters [45].

Terekhov et al. [90] investigated the influence of a spherical dimple on heat transfer by the upstream dimple. The local heat transfer was enhanced near the rear dimple's edge. However, the influence on the mean Nusselt number on the surface was nearly independent of this effect. Meanwhile, Isaev et al. [40] numerically investigated the heat transfer of a wall with a dimple package. Their results showed the local Nusselt number ratio to be increased by the dimple rows.

Correlations

Table 2.2: Correlations of the previous studies

Author & year	Boundary condition	Dimple/channel geometry	Dimple arrangement	Correlation	
Presser, [73]	$T_w = const.$	$t/D_{\mathrm{d}} = 0.5$;	Single dimple	$\mathrm{Nu}_x = 0.001\mathrm{Re}_x^{1.33}[1 + 0.75 \times 10^3(\mathrm{Gr}/\mathrm{Re}_x^{5.33})^{0.25}]$; $\mathrm{Nu}_{\mathrm{x}} = 0.001\mathrm{Re}_x^{1.33}$; $\mathrm{Nu}_{\mathrm{x}} = 0.265\mathrm{Re}_x^{0.7}\mathrm{Pr}^m f_E^{0.2}$;	$\mathrm{Re}_{\mathrm{h}} \leq 2300$ $\mathrm{Re}_{\mathrm{h}} \leq 2300$ & $\mathrm{Re}_x \leq 10^4$ $\mathrm{Re}_{\mathrm{h}} \geq 2300$ & $\mathrm{Re}_x \geq 10^4$
Xiao et al., [99]	$\dot{q} = const.$	$t/D_d = 0.1\ and\ 0.3$; $h/D_{\mathrm{d}} = 0.25, 0.37\ and\ 0.5.$	Dimple array	$\overline{\overline{\mathrm{Nu}}}_{\mathrm{d}}/\overline{\overline{\mathrm{Nu}}}_{\mathrm{pl}} = 0.9583Re_h^{0.23}(h/D_d)^{0.53}(t/D_d)^{0.19} - 0.1977$;	$\mathrm{Re}_{\mathrm{h}} = 260 - 1030$
Burgess & Ligrani, [10]	$\dot{q} = const.$	$t/D_{\mathrm{d}} = 0.1, 0.2\ and\ 0.3.$	Dimple array	$\overline{\overline{\mathrm{Nu}}}_{\mathrm{d}}/\overline{\overline{\mathrm{Nu}}}_{\mathrm{pl}} = 1.0 + 6.183(t/D_{\mathrm{d}})^{1.162}$;	$\mathrm{Re}_{\mathrm{h}} = 5000\ - 8 \times 10^4$
Bunker & Donnellan, [9]	$\dot{q} = const.$	$D_d/D_{\mathrm{h}} = 0.271$; $f_S = 0.473.$	Circular tube with dimple structures	$\overline{\overline{\mathrm{Nu}}}_{\mathrm{d}} = 0.033\mathrm{Re}_{\mathrm{h}}{}^{0.83}\mathrm{Pr}^{0.33}$;	$\mathrm{Re}_{\mathrm{h}} = 2 \times 10^4 - 5 \times 10^4$
Syred et al., [87]	$\dot{q} = const.$	$t/D_{\mathrm{d}} = 0.5.$	Single dimple on a curved surface	$\overline{\overline{\mathrm{St}}}_{\mathrm{d}}/\overline{\overline{\mathrm{St}}}_{\mathrm{pl}} = 1.2\boldsymbol{\Psi}$, where $\Psi = [1 + 1.8 \times 10^3\lvert\delta^{**}/R\rvert]^{0.16}$ [53];	$\mathrm{Re}_{\mathrm{h}} = 1.3 \times 10^5 - 3.1 \times 10^5$
Rao et al.,[76]	$\dot{q} = const.$	$t/D_{\mathrm{d}} = 0.2$S.	Fin-dimple channels	$\overline{\overline{\mathrm{Nu}}}_{\mathrm{d}} = 0.21\mathrm{Re}^{0.69}.$	$\mathrm{Re}_{\mathrm{h}} = 1100 - 1.1 \times 10^5$

2.3 IR Thermography

In this section, the background of IR thermography is presented. Physical basis of this method is introduced in section 2.3.1, followed by a description of the different calibration methods for determining the wall temperature in section 2.3.2. Finally, different measurement techniques and their respective advantages and disadvantages are discussed in section 2.3.3.

2.3.1 Physical Basics

The physical process of IR thermography includes three parts: the emission, transmission and detection of the IR radiation. A typical observation scenario is that the IR radiation emitted from the object's surface detected by the IR camera through the transparent media. This section will consider these three parts in detail, also discussing the relationship between the wall temperature and the detected IR intensity.

Emission and Transmission

According to Planck's law, the absolute surface temperature of a black body is related to the spectral radiance emitted from it through the equation

$$M_{\mathrm{B}}(T,\lambda)=\frac{N_1}{\lambda^5}\frac{1}{\left(\exp\left(\frac{N_2}{\lambda T}\right)-1\right)}, \tag{2.5}$$

where $N_1 = 2\pi hc^2 = 1.19104 \times 10^{-16}\,\mathrm{Wm}^2$ and $N_2 = hc/k = 0.014\,\mathrm{mK}$. If the equation is integrated into the whole wavelength, a simple correlation between the radiation energy and temperature can be determined by Stefan–Boltzmann law:

$$\int_0^{\infty} M_{\mathrm{B}}(T,\lambda)d\lambda = \sigma T^4, \tag{2.6}$$

where $\sigma = 5.67 \times 10^{-8}\,\mathrm{W/m^2K^4}$ is the Stefan-Boltzmann constant. This shows that the power of radiation emitted from a body has a four-ordered relation to the body temperature. The basis of the relations above is the assumption that the object is a black body. However, the most objects measured by IR thermography are gray bodies, which radiate less energy than a black body. In this case, the emissivity ε is used to describe the radiance from these bodies

$$M_{\mathrm{Gray}}(T,\lambda) = \epsilon M_{\mathrm{B}}(T,\lambda). \tag{2.7}$$

The emissivity is different for different surface qualities, temperatures, wavelengths, and angles between the normal axes of the surface. In this case, the emissive power of a surface at a specific spectrum range and emission angles is expressed as

$$I(T) = \epsilon \int_{\lambda_1}^{\lambda_2} M_{\mathrm{B}}(T, \lambda) d\lambda. \tag{2.8}$$

Here, it is assumed that the emissivity is not sensitive to temperature and wavelength. As a result, the emissive power is only related to the temperature in a fixed spectrum range and at a fixed position in the space.

Before being detected by the IR camera, the emissions from the surface travel through the transparent medium, which is frequently the atmosphere. In this process, the received radiance power is influenced by either the transmittance τ of the media and reflectivity ρ of ambient radiations at the interfaces and the radiation from the media. Thus, the received radiance power after the media becomes

$$I(T) = \epsilon\tau I_{\mathrm{B,\,obj}}(T) + (1-\rho)\tau I_{\mathrm{B,\,amb}}(T) + (1-\tau) I_{\mathrm{B,\,med}}(T). \tag{2.9}$$

The influence of the reflection is ignored during the measurement, if the space between the surface and camera is isolated from the ambient radiation sources.

Furthermore, according to Wien's displacement law, the distribution of the spectrum radiance from a black body at a certain temperature has a maximum value at a peak wavelength, which is

$$\lambda_{\max} = \frac{2880}{T}. \tag{2.10}$$

In the normal applications of temperature measurement, much larger amount of emitted radiation are in the infrared range which has a specified wavelength from 3 μm *to* 15 μm. Due to the band between 5 μm *and* 7.5 μm being the adsorption band of the atmosphere, the IR band is therefore technically divided into the middle infrared band (MWIR, 3 μm $-$ 6 μm) and the long infrared band (LWIR, 6 μm $-$ 15 μm).

Detection

The IR camera detects the IR power and digitizes the signals into the thermal image. The sensor system of the camera includes the lens and detector. The lens optics are made of either silicon for MWIR or Germanium for LWIR. The detector is an array of sensors, which can be divided into two types, the thermal detector and the quantum detector. The thermal detector consisting of the semiconductor observes the IR intensity via the local temperature change, caused by the absorption of the IR power. The quantum detector senses the IR power by the quantum well IR photon effect, which accumulates the numbers of IR photons into a single measure of the IR intensity. Compared to the thermal detector, the quantum detector is more sensitive and has

faster response times. It is made of either Indium antimonide (InSb) for MWIR or HgCdTe alloy (MCT) or GaAs/AlGaAs layers for LWIR. At the operation temperature of around 77 K, the directivity of the detector is approaching an optimum value. For the application, the MWIR detector is lower in price and is more sensitive than the LWIR detector at temperatures above 10 ℃.

The quality of the IR camera is evaluated primarily by three aspects: thermal sensitivity, scan speed, image resolution and dynamic range. The thermal sensitivity is estimated by a mean noise equivalent temperature difference (NETD, mK) which is a mean value of the maximum difference of the pixel values when observing a black body. The scan speed is the frame rate of the recording image. The image resolution is the spatial resolution of the camera field of view (FOV) which is calculated from the area of FOV divided by the total number of pixels of the detector. The dynamic range is the digital step which can describe the maximum observable temperature difference of the camera.

2.3.2 Calibration

The calibration of the IR camera is a process intended to determine the correlation (F) between the IR intensity and temperature for each pixel, which is expressed for a limited sized surface as

$$T = F(I, \epsilon, \beta_1, \beta_2), \tag{2.11}$$

where:
ϵ is the local emissivity,
β_1 and β_2 describe the angles between the local surface's normal axes to the optic axis, respectively.

The correlation F can be determined by two methods: the black body calibration and the in-situ calibration. Between these two methods, in-situ calibration is the easiest and most direct method to determine the correlations within a temperature range. In the in-situ calibration, local IR power in an IR image and the reference temperature of the body (assuming that the body temperature is homogeneous) are measured simultaneously at certain levels in the calibration temperature range. By the regression method, the correlation results as a characteristic curve, also called the calibration curve. According to Stefan-Boltzmann's law, as shown in equation (2.6), the relationship between IR intensity and body temperature is a fourth power relation. In a large temperature measurement range, a non-linear regression function of the calibration is selected [63, 78]. It should be note that the calibration is based on the assumption that the surface has the same temperature, related to the homogeneous IR intensity received from the surface. However, in many cases, the IR intensity of the isothermal surface is not uniform. This is due to the emissivity of the surface changing from place to place because of the local surface

geometries or surface quality. Therefore, it is necessary to conduct a pixel-wise calibration method, as described by many authors [63, 97].

2.3.3 IR Thermography in Thermal Fluid Studies

In many thermal fluid studies, the heat flux or the heat transfer coefficient is most frequently focused on. A popular method for determining these parameters is by applying the heated thin foil technique, in which the local heat transfer is determined by using the IR thermography to access wall temperature distributions on an IR accessible thin foil placed in the flow and providing constant heating via Joule heating. For example, in the pool boiling experiments, heat flux is determined through the temperature gradient on the foil surface [63, 97]. Another parameter, the heat transfer coefficient, is determined by assessing the temperature difference between the wall and flow at the known heat flux [12, 25, 56].

In most convective heat transfer studies, airflow is used as the working fluid. Since air is transparent in the operational IR spectrum, the wall temperature is then measured from the fluid-side. In all previous heat transfer studies of dimple structures, the IR measurement has been conducted in this way [12, 18, 56]. In other cases such as pool boiling or falling film studies, the fluid flow is either IR-opaque or the observation is disturbed by bubbles, thus rendering the observation on the fluid side quite difficult. Therefore, a new method was developed by observing the rear side of the heating surface through an IR-transparent glass [23, 85, 96]. Since the foil is very thin, the temperature profile on both sides is considered to be the same. Meanwhile, the IR-transparent glass is used to hold the thin foil and the IR access window in the measurement.

Through the vapor deposition technology [7], coated heating layers were developed instead of metal foils. The layer, which is created on the glass substrate by physical vapor deposition (PVD), also called sputtering, is even thinner than the metal foil. Besides, since the coating is deposited at the atomic level, the coating is more homogenous on the substrate surface. In other words, the coated layer is suitable for the heating not only on plane surfaces but also for some curved or structured surfaces. For example, Yen et al. [100] deposit a 100 nm thick ITO/Ag layer providing constant heat flux by Joule heating on the micro channels with a diameter of around 200 μm. The coating materials are primarily metallic materials, such as gold, platinum, conductive oxidations like ITO [22, 67], etc. The benefit of using ITO as the coating material is first, the coating material has a higher resistivity than the metals, and second, the coating is opaque in MWIR. However, the oxidation is not stable during heating in the air, and electric charging needs protection. In the study by Schilder et al. [79], a Parylene-F coating was added to the ITO layer

to avoid the layer oxidizing when being heated in air. To that end, the deposition technique enables functional area coating and multi-layer structured coating. In order to achieve a homogeneous heating on the ITO layer deposited on glass, a copper layer was added by copper plating on the sides of the heating area [70]. Furthermore, as shown in Fig. 2.11, the gold coating was coated much thicker on the sides of the heating area for the same purpose.

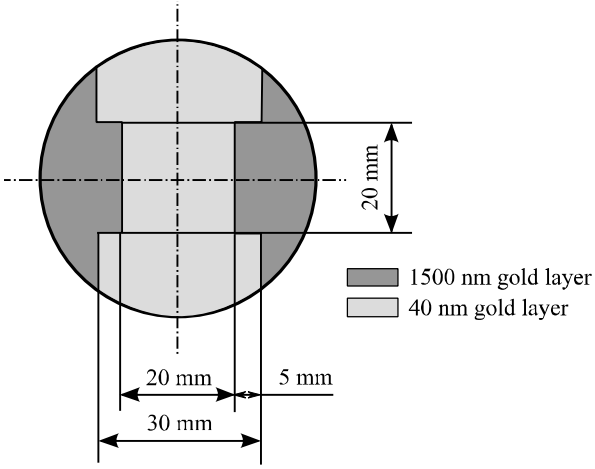

Fig. 2.11: Structured coating surface on a 10 mm zinc sulfide glass (ZnS) substrate with different coating thicknesses [60].

2.4 Summary and Scope of Study

As one of the methods for passive heat transfer augmentation, dimple structures not only intensify the heat transfer but also show less flow resistance compared to other methods. The heat transfer mechanism is due to the enhanced turbulence created by the dimple structure and the redevelopment of the boundary layer in the dimple wake. Flow visualizations and simulations showed that a vortex structure is generated in the recirculation region of the dimple. This vortex leads to the heat transfer inside the dimple being enhanced near the trailing edge and reduced near the leading edge. Given the three-dimensional geometry of the dimple, the vortex is symmetric at a lower Reynolds number or in a shallow dimple and becomes asymmetric in turbulence or at a deeper dimple depth. Heat transfer studies showed that in a broad range of Reynolds numbers in turbulence, the highest Nusselt number ratio in the streamwise center plane of the dimple structure is around 3.3. Furthermore, two types of vortex oscillations were discovered inside the dimple. The high frequency oscillation that took place in the entire Reynolds number range is a periodical outburst of the jet inside the dimple. The low frequency oscillation, called the switching mode, was discovered in deep dimple ($t/D_\mathrm{d} = 0.26$) in the Reynolds number range of $\mathrm{Re_d} > 1 \times 10^4$. However, since the heat transfer in and around

dimples is complex and dynamic and limited by the experimental method, the details of the heat transfer process in the dimple structure have not yet been clarified.

The aim of the study is to investigate heat transfer on dimpled surface in turbulent flow by using high-resolution IR thermography, which visualized and measured local wall temperature distributions on the surface over time. Surface with single dimple structure having the similar geometries reported by Terekhov, Isaev and Turnow was focused to compare to the previous experiment and simulation results. In order to study the influence of upstream dimple to the next one, which provides a detailed study for dimple array, double-dimpled surface was considered as well. Constant heat flux boundary conditions were achieved by generating joule heating from a multi-layer coating on each dimpled surface in hydraulically developed channel flows. In this case, Nusselt number distributions can be calculated from the measured temperature distributions for quantifying the local heat transfer on the surfaces. Furthermore, comparing to the referenced Nusselt number distributions, performance parameters were determined for quantifying the heat transfer enhancement of the structured surface. Due to the complexity of the experimental condition during the measurement, which is an asymmetric heating with developed hydraulic boundary and developing thermal boundary layer, the reference Nusselt number distributions were collected from a plane surface heated in the flow with identical experimental parameters. Sequences of temperature distributions on dimpled surfaces were measured with a frequency up to 50 Hz to study the fluctuation of wall temperature over time. The observation of low frequency switching mode in and near the dimple structure was also an aim of the experiment.

Chapter 3

Experimental Methodology

In this chapter, the experimental method used in this study is introduced. It covers three major phases: the experimental setup, conditions, and measurement method. In section 3.1 and 3.2, the experimental setup is presented from its basic concept to its structure, including the water circulation system and test section. After that, typical parameters and experimental conditions for the experiments are listed in section 3.3, followed by a separated description of the measurement procedure in section 3.4. A summary concludes the chapter in section 3.5.

3.1 Experimental Setup

3.1.1 Concept

The diagram in Fig. 3.1 is the basic concept of the experiment. The wall temperature of a heated surface on the bottom wall of a channel is observed by an IR camera installed vertically below. The channel is locally heated on this surface, while the remaining channel is virtually adiabatic. This heated wall is made from IR-transparent glass, features the dimpled surface, and is coated with an electricity-resistive film on the test surface side to provide variable Joule heating and high emissivity for infrared measurements. Since the heating surface (the coating) is very thin, the temperature difference between its two faces is negligibly small. The temperature distribution of the dimpled surface is determined by performing a spatially resolved calibration of the local infrared emission rate with respect to the coating temperature. Furthermore, the inlet flow is hydraulically fully developed in the investigated flow velocity range and adjustable within a certain temperature range. The measurement is then conducted under different experimental conditions with regard to three parameters: heat flux $\dot{q}$, Reynolds number ($\mathrm{Re_d}$ or $\mathrm{Re_h}$) calculated from the mean flow velocity $\overline{U}$ and inlet temperature T_{in}. The measurements were performed in many experimental conditions in order to investigate the influence of these varying conditions.

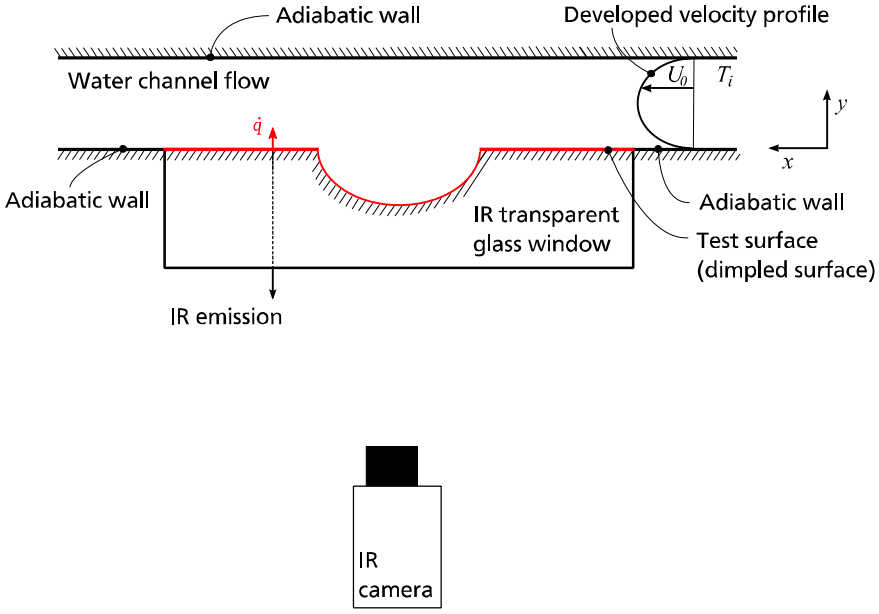

Fig. 3.1: Diagram of the experiment concept.

According to the experiment concept, an experiment setup was developed for implementing the experiment, such as different test surfaces and experimental conditions. The setup is a water circulation system, consisting of the tube section, channel section, and the test section.

3.1.2 Water Circulation System

As shown by the schematic in Fig. 3.2, the water circulation system is a closed loop system with a flow of deionized water. The system consists of a 25 L Teflon water tank, a variable speed progressive cavity pump[4], an in-line filter[5], a flow meter[6], a plate heat exchanger[7], and the channel section, which includes a flow-regulating part and a long channel, made of polycarbonates. The test section was installed near the outlet end of the long channel. Below the test section, an IR camera[8] was installed. Except for the channel section and the test section, all the parts connected by flexible circular tubes of the same size. The deionized water has an electrical conductivity of $0.1 - 0.6$ μS/cm before being filled into the water tank. Its flow is initiated and maintained by the progressive cavity pump with the flow rate range of $2.8 - 16$ l/min, which is set by a potentiometer controller. In the plate type heat exchanger, the

[4] Type MD 05-6LT, Seepex GmbH, Bottrop/Germany

[5] Cintropur® Type NW25 (filter mesh sized 50 μm), Airwatec s. a., Eupen/Belgium

[6] Type 8035, Christian Bürkert GmbH & Co. KG, Ingelfingen/Germany

[7] APTE® Type WP01-020, Apparatetechnik Harald Schönstein GmbH, Hamburg/Germany

[8] PtSi 256 SM with a MWIR-28mm lens, DCG Systems GmbH, Erlangen/Germany

working fluid temperature, varying from 24 to 50 °C, is controlled by a thermostat. The inlet and outlet flow temperature are measured by the two thermocouples placed respectively in the inlet section and outlet of the long channel. The channel has a height of 5 mm, a width of 32 mm and a length of 720 mm. The length of the long channel is around 84 times that of the channel hydraulic diameter (D_h = 8.6 mm). It is much larger than the length of developing section of turbulent flow which is 60 times that of the hydraulic diameter [8]. The channel system (including the test section) and the test section were covered with 20 mm thick Polystyrene foam sheets to reduce the heat loss from the flow to the environment.

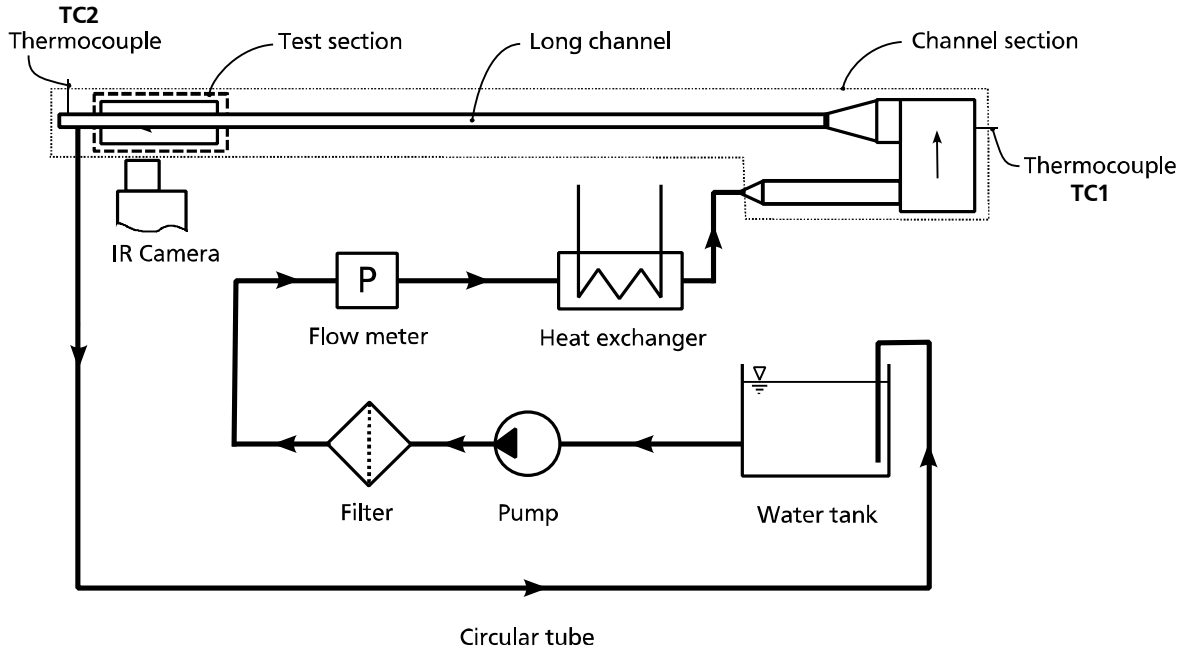

Fig. 3.2: Schematic of the experimental setup.

The flow-regulating part made of stainless steel consisted of two metal tubes, a diffuser, a turning section, a honeycomb, and a convergence section (Fig. 3.3). The diffuser expands the cross section of the inlet tube with an expansion rate (s_2/s_1) of 10. The circular tube was connected with the turning section, and the cross section here is rectangular, at a size of 85 mm × 32 mm. There is another opening in the turning section above the tube, connected to a honeycomb with a cross section of 32 mm × 65 mm and a length of 45 mm. This honeycomb is array of 75 miniature hexagonal-channels at a characteristic diameter of 5 mm in each passage. After the honeycomb, the convergence section was installed, compressing the channel's cross section to 32 mm × 5 mm with a contraction rate of 11.2. Between the honeycomb and the convergence section, a screen was installed. At the end, a plastic valve was installed on the topside of the turning section, along with the thermocouple TC1.

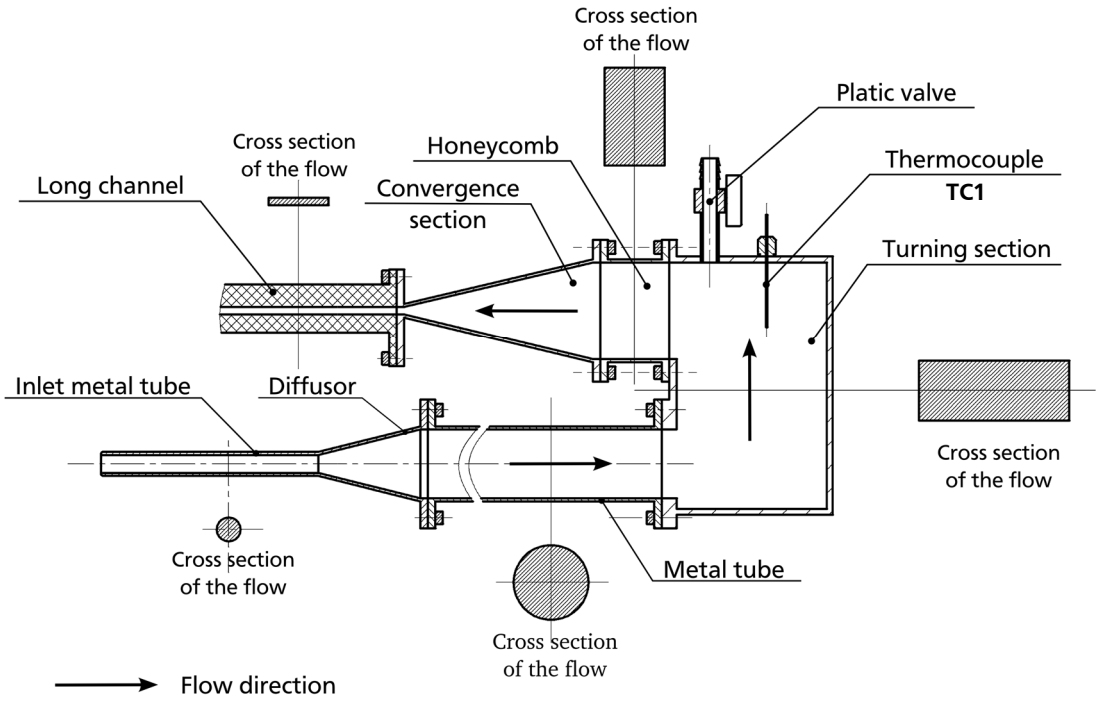

Fig. 3.3: Structure of the flow regulating part.

3.1.3 Test Section

The test section, consists of the bottom mounting part, a plastic cover and the glass window, is installed near the outlet of the long channel (Fig. 3.4). Both bottom mounting plate and cover are screwed into place, respectively at the bottom or on top, to form a part of the channel wall. In the bottom mounting plate, a glass window is installed, its heating surface flush with the bottom wall of the long channel. On the other side of the glass, an arena shape opens (see Fig. 3.9) just below to allow optical access for IR measurement. In order to avoid the influence of ambient IR radiations, the space between the glass window and the IR camera was enclosed by the polystyrene foam wall.

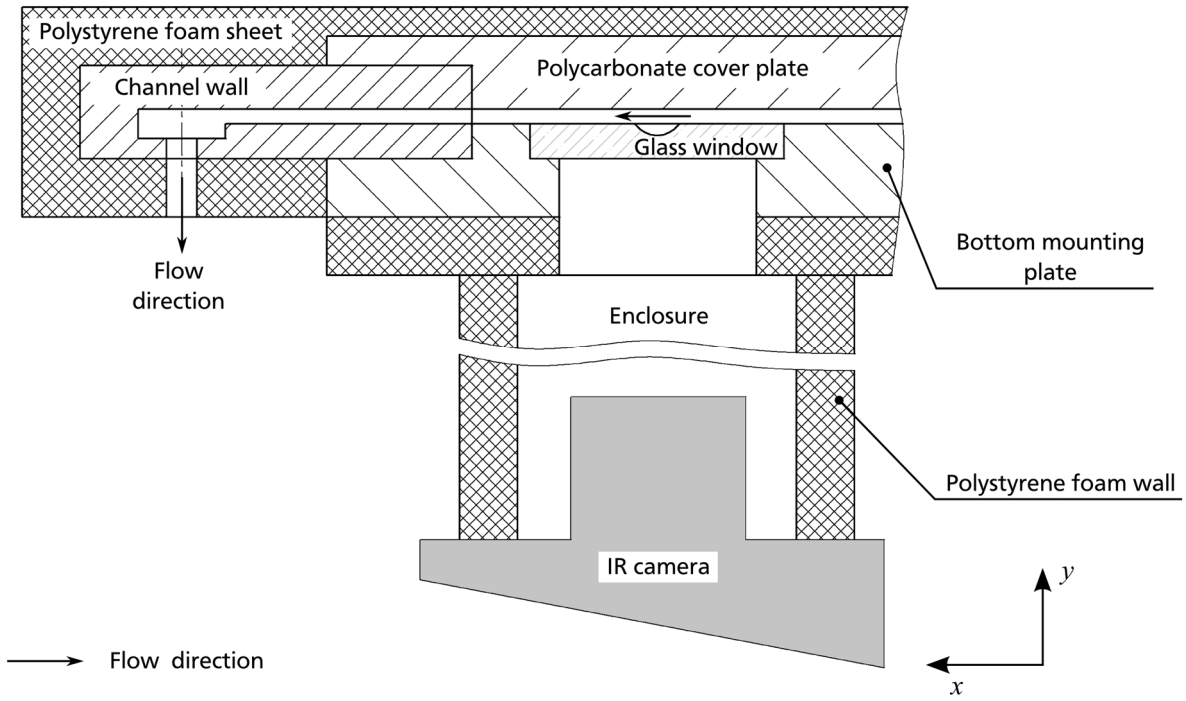

Fig. 3.4: Side view of the test section.

Electric Connection

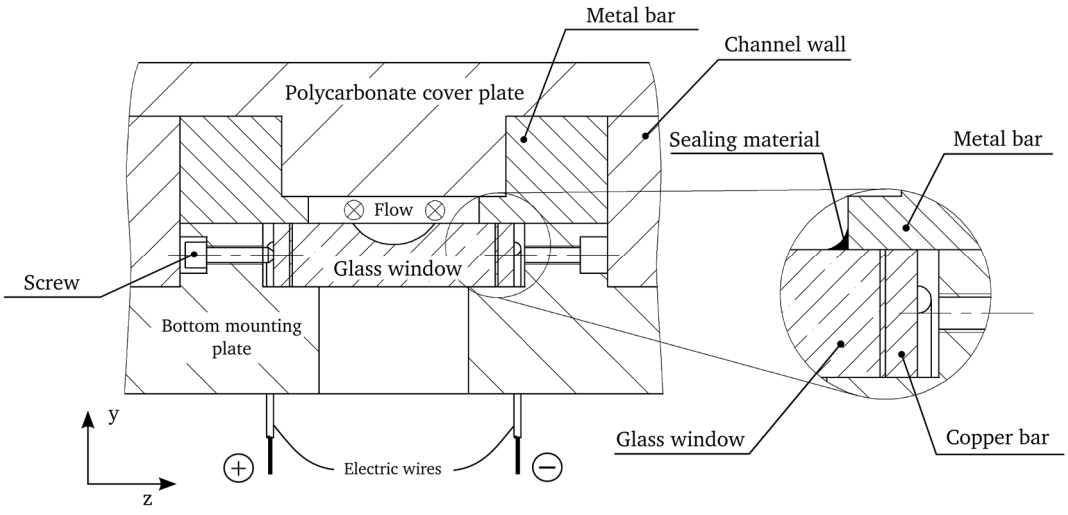

Fig. 3.5: Cross section of the test section.

The electric circuit in the test section was designed to provide electric power for Joule heating on the heating surface. It includes the external power supply, cables, copper bars and the glass window. The arrangement of this circuit is schematically shown in Fig. 3.5 (the power supply is not displayed). After being pressed in the bottom mounting plate by two metal bars, two copper bars were inserted under the screws and attached on the sides of the glass. Meanwhile, two

50 μm copper foils were placed between the bars and the glass surface to ensure a good contact between these parts. Two cables were welded to these copper bars, separately connected to the external DC power supply[9] through the holes made on the bottom mounting plate. Due to the special design of the coatings on the glass window, the current was led from one side of the glass to the top surface, on which the heating surface is located, and then to the opposite side, connected to the cathode. Due to the heating surface's significant electric resistance, Joule heating was continuously provided from here through the electric current. In order to prevent leakage between the parts, except for those fixed by screws, silicon glue was applied as the sealing material in the gaps. For the same purpose, thin dielectric tapes were attached on the topside of the space enclosed by the bottom mounting plate and the glass sides.

Glass-Heating Element

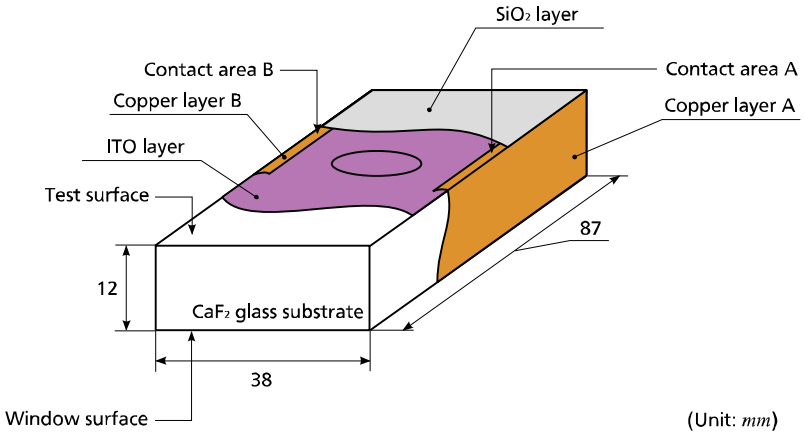

Fig. 3.6: Structure of the heating element.

The glass-heating element consisted of an IR-transparent glass substrate and a multi-layer heating film (Fig. 3.6). The glass substrates made of the calcium fluoride (CaF_2) crystals are transparent in the wavelength range of 0.2 – 7 µm. The element has a rectangular shape in the size of 87 mm × 38 mm × 12 mm. Dimple structures were processed onto the test surface which is a diffused surface with an average surface roughness[10] of 12 μm. On the other side, the window surfaces were polished to a surface quality of 60/40 [11]. On the glass substrate, three different layers[12] were coated to satisfy the functions listed in Table 3.1. The first layer deposited

[9] EA-PS 3032-05 B, Elektro-Automatik GmbH & Co. KG, Viersen/Germany.

[10] Average distance between the highest peak and lowest valley in the sampling length.

[11] Scratch width / dig diameter.

[12] The coatings were processed by IOF Fraunhofer, Jena/Germany.

on the test surface was the ITO layer with a thickness of around 1.7 μm and a measured surface resistance of 6.55 Ω[13]. The second layer was the copper layer, covering two areas at the sides (A/B areas). On each side, the coating was attached to the ITO coating on the contact area and the surface at the glass side, crossing a 90° edge. Finally, the SiO_2 layer was coated on the test surface covering the ITO layer and copper layer in the area.

Table 3.1: Layers of the heating film.

Coating layer	Thickness	Function	Preparation method
ITO layer	~1.7 μm	Joule heating	Deposited by plasma ion-assisted evaporation [21]
Copper layer	500 nm	Enhancing electric contact	PVD at room temperature
SiO_2 layer	2.5 μm	Protecting the ITO and copper layers during heating	PVD at room temperature

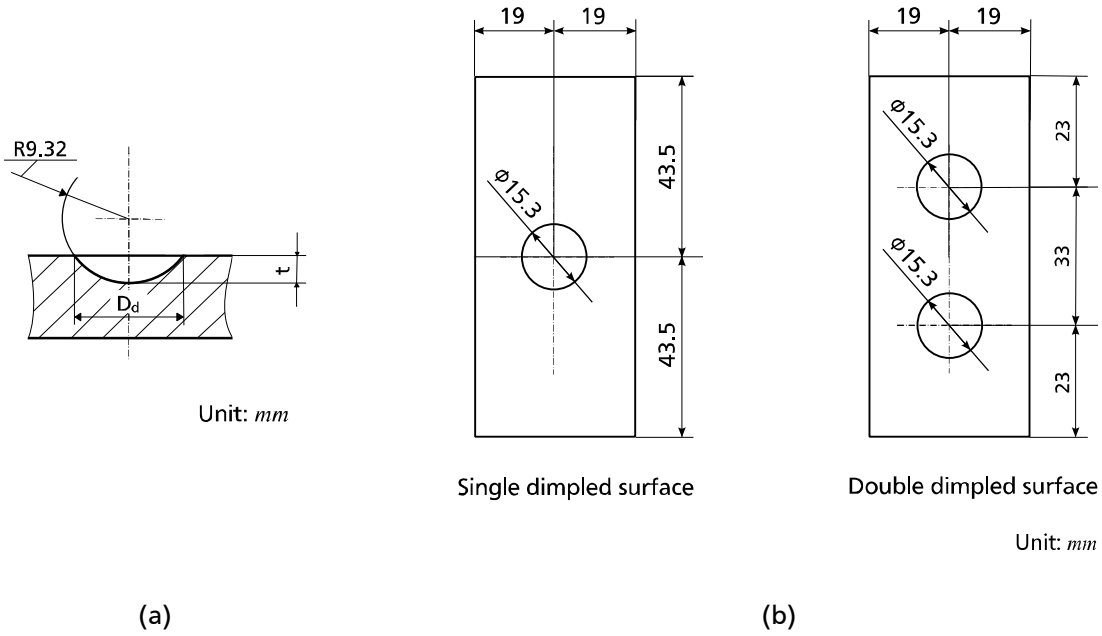

Fig. 3.7: Dimensions and arrangement of the dimples on the test surface: (a) dimensions of the dimple structure; (b) dimensions of two investigated dimpled surfaces.

The dimensions of the dimple structure are shown in Fig. 3.7(a). The dimple is a spherical cap-structured concavity in the wall and has a printing dimple diameter D_d of 15.3 mm and a dimple

[13] Calculated from a measured surface resistance of 15 Ω/square.

depth t of 4 mm. Thus, the relative depth (t/D_d) of the structure is 0.26. The edge of the dimple structure was considered as a sharp corner. This dimple structure was used in both types of structured test surfaces in the arrangements shown in Fig. 3.7(b). In the single-dimpled surface, the dimple structure is centered, while in the double-dimpled surface, the structures with same dimensions were centered along the Z coordinate and systemic to the centerline of the surface along the X coordinate.

Reference Surface

A reference surface was investigated in the experiment and considered as the baseline of the heat transfer compared to dimpled surfaces. This surface is a plane surface and has the same dimensions, substrate and coating layers as the structured surfaces.

3.2 Determination of the Experimental Conditions

An experimental condition for the measurement is the combination of three parameters, as listed in Table 3.2. The Reynolds number in the long channel is calculated from the measured flow rate. The inlet flow temperature was measured by the thermocouple (TC-1) placed before the long channel (see Fig. 3.2 and Fig. 3.3). The heat flux was determined by calculating the measured current and voltage against the heating area. Here, the Reynolds number and the flow temperature are summarized as the flow properties for the introduction. Finally, several characteristic values were picked for each parameter in order to determine different experimental conditions.

Table 3.2: Ranges of investigated parameters

Parameter	Range	Characteristic values
$\mathrm{Re_d}[-]$	$10^4 - 3.5 \times 10^4$	$1 \times 10^4, 1.5 \times 10^4, 2 \times 10^4,$ $2.5 \times 10^4,\ 3 \times 10^4$ and 3.5×10^4
T_{in} [°C]	$25 - 43$	$25, 30, 35, 40$ and 43
$\dot{q}$ [kW/m^2]	$18 - 53$	$18, 32$ and 53

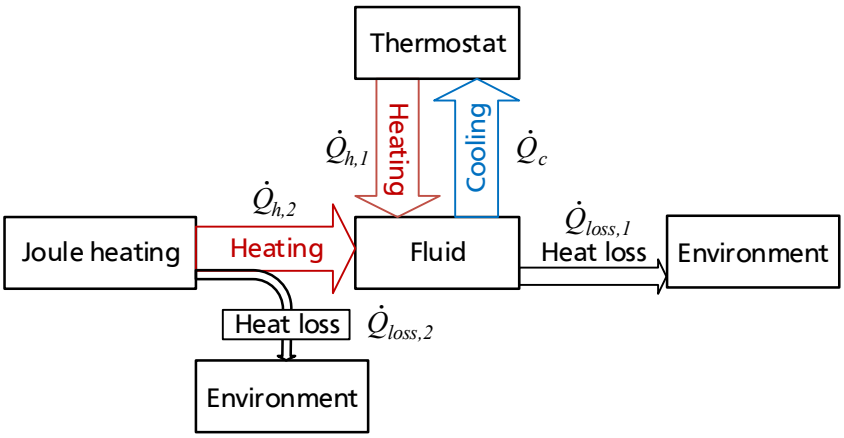

Fig. 3.8. Heat balance of the experimental setup

In order to estimate the heat loss of the system, the heat balance of the setup is discussed in this section. As shown in Fig. 3.8, the heat from the thermostat and Joule heating on the heating surface was introduced into the fluid. Heat losses occur both in the flow and from the heating surface during Joule heating. The experiment consisted of a calibration and heating experiment. In this case, the heat balance can be divided into two major scenarios, as described below.

Heat Balance in Calibration

In the calibration, since there was no heating from the surface, the heat balance was only established between the thermostat, fluid, and environment. The heat flow $\dot{Q}_{\mathrm{h},1}$ from the thermostat was introduced to the flow to compensate for the heat loss $\dot{Q}_{\mathrm{loss},1}$ to the surroundings:

$$\dot{Q}_{\mathrm{h},1} = \dot{Q}_{\mathrm{loss},1} \,. \tag{3.1}$$

This heat loss occurs at the non-insulated parts, including the pump, water tank, filter, and the glass window in the test section, and depends on the temperature difference between the flow and its surroundings. Since the thermostat has a heating power of up to 1 kW, the heat losses in these areas were compensated, and the inlet flow temperature has less influence from the surrounding temperatures.

Heat Balance in Heating Experiment

In the heating experiment, Joule heating of the heating surface was an additional heat source to the flow, which is equal the input electric power P. Since a heat loss $\dot{Q}_{\mathrm{loss},2}$ occurred in the test section, the heat flow $\dot{Q}_{\mathrm{h},2}$ was:

$$\dot{Q}_{\mathrm{h},2} = P - \dot{Q}_{\mathrm{loss},2} \,. \tag{3.2}$$

Two types of scenario could be distinguished here. In the first case, since the heat flow from the surface was comparably smaller than the heat loss $\dot{Q}_{\mathrm{loss},1}$, the thermostat still provided heat to the flow. Then, the balance is

$$\dot{Q}_{\mathrm{h},2} + \dot{Q}_{\mathrm{h},1} = \dot{Q}_{\mathrm{loss},1} \ . \tag{3.3}$$

In another case, the heat flow from the surface was greater than the heat loss $\dot{Q}_{\mathrm{loss},1}$. In this case, the thermostat cools down the flow by removing heat from the system:

$$\dot{Q}_{\mathrm{h},2} = \dot{Q}_{c} + \dot{Q}_{\mathrm{loss},1} \ . \tag{3.4}$$

The heat flow from Joule heating ($\dot{Q}_{\mathrm{h},2}$) used in the experiment is listed in Table 3.3. It has been assumed that the heat loss $\dot{Q}_{\mathrm{loss},2}$ in the test section is very small and therefore can be ignored (see section 3.3.2). In this case, the heat flow $\dot{Q}_{\mathrm{h},2}$ in the heating experiment is equal to the heating power P. In the experiment, the scenario mentioned firstly occurred both in the low heat flow case, and the second scenario happened in the high heat flow. This suggests that with the heat flow below or equal to 91 W, the heat was primarily exhausted through the uncovered parts of the test section. Nevertheless, since the cooling power $\dot{Q}_{\mathrm{c}}$ of the thermostat is 200 W, the inlet flow temperature was always independent of the higher heat flow from the surface.

Table 3.3: Heat flows investigated in the heating experiment

Experiment	Heat flux [kW/m^2]	Heat flow [W]
Low	18	51
Reference case	32	91
High	53	160

3.2.2 Flow Properties

Determination of the Reynolds Number

The Reynolds number of the flow in the long channel is determined by the mean flow velocity, characteristic length, and flow viscosity. The mean flow velocity $\overline{U}$ is calculated from the flow rate V against the channel cross section $s_{\mathrm{c}} = 32\ \mathrm{mm} \times 5\ \mathrm{mm}$. In the normal definition, the characteristic length is the hydraulic diameter D_{h} of the long channel. However, in order to compare the results with the previous studies, the dimple-printing diameter D_{d} is used as the characteristic length in this study as well. Therefore, to avoid confusion, the Reynolds numbers were distinguished as channel Reynolds number ($\mathrm{Re_h}$) and dimple Reynolds number ($\mathrm{Re_d}$), respectively (equation 2.4). The viscosity of the liquid was picked up from the VDI-Wärmeatlas [1].

The flow rate was measured by a flow meter[14] installed after the pressure-side of the pump. The measured flow rate data was sampled by a DAQ (data acquisition) system[15], connected to the flow meter, with the data stored on a PC. In the previously mentioned Reynolds number range, the flow rate varied from 1.8 l/min to 17 l/min accordingly. Thus, the measurement accuracy of the flow rate is between $\pm 4\%$ and $\pm 0.5\%$ [16]. The uncertainty associated with the Reynolds number will be discussed in section 4.2.2.

Measurement of inlet flow temperature

The inlet flow temperature was measured by calibrated Type-K thermocouple[17] (TC-1) connected to the DAQ system. The conjunction of the thermocouple was placed at the center of the channel to guarantee measuring a free stream temperature of the flow. Furthermore, the analog signal measured by the thermocouples was acquired and digitized by the DAQ system and recorded on the PC by the LabVIEW program. In this process, since the input signal is quite small, the total measurement error of the temperature includes not only the error of sensor, but also the error of the DAQ system, both of which are listed in Table 3.4.

Table 3.4: Accuracy of the NI DAQ system[18]

Temperature (°C)	Input voltage signal (mV)	PCI absolute accuracy (mV)	SCXI absolute accuracy (mV)	System accuracy (mV)
24	± 0.960	± 0.0016	± 0.0301	± 0.0302
50	± 2.023	± 0.0022	± 0.0303	± 0.0304

The thermocouple sensor was calibrated with the aid of a resistance temperature detector (RTD, PT100) in a range of $20 - 50$ °C and gained an accuracy of ± 0.13 K. According to Table 3.4, in the calibration temperature range from 24 °C to 50 °C, the error of the DAQ process lies between ± 0.0302 mV and ± 0.0304 mV. According to the revised thermocouple reference table, every change of 1 K in the temperature measurement, voltage variation from the k-type thermocouple is 0.040 mV. Thus, the equivalent temperature accuracy of the DAQ system is within $\pm 0.76\,K$. Therefore, the total temperature measurement accuracy of inlet flow temperature is ± 0.77 K.

[14] Type 8035, Christian Bürkert GmbH & Co. KG, Ingelfingen/Germany.

[15] Type SCXI 1102 Input module and Type PCI-6036E, NI Crop., Austin/Texas.

[16] The error of the DAQ system is ignored here.

[17] Type-K class-I grounded thermocouples with 0.5 mm sheath diameter.

[18] Calculated from: http://www.ni.com/advisor/accuracy/.

3.2.3 Heat Flux

The heat flux $\dot{q}$ is defined as the heat flow $\dot{Q}_{h,2}$ divided by the heating surface area $s_{heating}$. Since the heat loss $\dot{Q}_{loss,2}$ is ignored in this study, the heat flow is equal to the power of the Joule heating P which is calculated from the voltage U and current I on the heating surface. To achieve the heat flux range shown in Table 3.2, the power provided on the surface reaches up to 160 W, a maximum voltage of 25 V, and a maximum current of 6.4 A. The voltage was measured by a multimeter[19] connected to the cables from the electrodes with a measurement accuracy of $\pm 0.7\%$. The current was measured by the ammeter embedded in the DC power supply with an accuracy of $\pm 2\%$. In this case, the uncertainty in determining the heat flow $\dot{q}$ is $\pm 2\%$ (uncertainty for determine heating area was ignored).

The heating surface is the area on the test surface uncovered by the copper layers, which has three different types with sizes of $s_{heating} = 87\ mm \times 32\ mm + \Delta_{dimple}$ (Table 3.5). The value Δ_{dimple} is the area increase due to the dimple structure, which is expressed as the difference between the dimple surface area and the dimple printing area ($\Delta_{dimple} = s_d - s_{dp}$). In the experiment, the voltage and current were recorded manually, since little changes were expected during the whole process.

Table 3.5: Areas of different heating surfaces

Types of the heating surface	$s_{heating}[mm^2]$
Flat surface	2784
Single-dimpled surface	2834
Double-dimpled surface	2885

3.2.4 Experiment Conditions

The experiment conditions are represented by the combination of the characteristic values of three experimental parameters. Once the parameters are set, the experiment condition is determined for the heat transfer investigation. In the experiment, the experiment conditions were planned in advance and are shown in Table 3.6. Condition No. 5, in which $Re_d = 2 \times 10^4$, $T_{in} = 35\ °C$ and $\dot{q} = 32\ kW/m^2$, is set as the reference condition of the investigation. Other conditions are implemented by changing the parameters of this reference condition one at a time.

[19] Hexagon 110, BEHA-AMPROBE Glottertal FLUKE Deutschland GmbH, Glottertal/Germany.

Table. 3.6: Experiment conditions

Exp. cond.	$\mathrm{Re_d}$[-]	T_{in} [°C]	$\dot{q}$ [kW/m²]	Exp. cond.	$\mathrm{Re_d}$[-]	T_{in} [°C]	$\dot{q}$ [kW/m²]
1	2×10^4	25	32	7	3×10^4	35	32
2	2×10^4	30	32	8	3.5×10^4	35	32
3	1×10^4	35	32	9	2×10^4	35	18
4	1.5×10^4	35	32	10	2×10^4	35	53
5	2×10^4	35	32	11	2×10^4	40	32
6	2.5×10^4	35	32	12	2×10^4	43	32

3.3 Wall Temperature Measurement

Wall temperatures were measured by the IR thermography system consisting of the IR camera, a PC, and a specified power supply. Before the measurement, the camera was installed vertically below the test section and focused on the rear side of the test surface. A calibration was performed to determine the calibration curve，i.e. the correlation between the local IR intensity and temperature on each pixel (see section 2.3.2). After completing the preparations, the measurement phase was started. IR images captured under each experiment condition were stored in a PC. Later, these IR images were translated into the temperature distributions with the aid of the calibration curves via a MatLab program. In all measurements, the integration time of the IR camera was set to 20 ms.

3.3.1 View of the IR Camera

Viewing Area

The camera was mounted on an aluminum plate fixated on two beams of the setup. Adjusting the positions of the plate and the beams brought the heating surface into the camera's field of view (FOV). The surface was focused on by manually adjusting the focal length of the camera lens. An IR image of a plane surface is presented in Fig. 3.9(a). The viewing area includes two regions displayed in Fig. 3.9(b). The arena shaped region is the viewed heating surface, while the left region is the view of the wall of the bottom mounting plate. Since it is blocked by the bottom mounting plate, the viewed heating area is a part of the total heating area. For the purpose of easier data processing (see section 4.1.1), a rectangular region inside the viewed

heating area of the size 48.3 mm × 19.8 mm was marked as the calibrated area. Hence, all the experimental results will refer to this area.

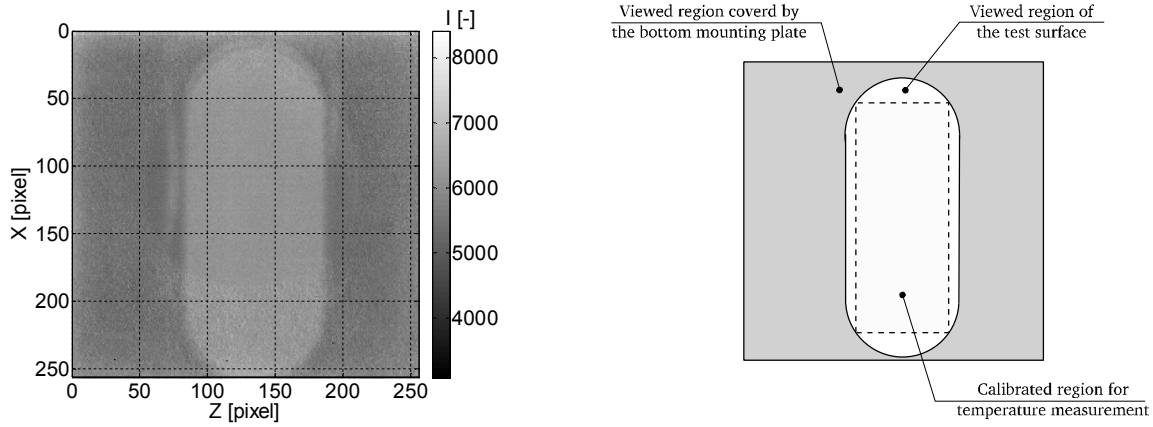

Fig. 3.9: View of the IR camera: (a) an IR image taken during calibration, (b) diagram of the areas in the view.

Measurement resolution

The measurement resolution consisted of the spatial and temporal resolution. The spatial resolution A was determined by calculating the pixels of an object with known dimensions. In this study, the rounded dimple's edge with a diameter of 15.3 mm was used as this reference object. Through a MatLab program, the number of pixels in the circle diameter was identified. After analyzing this for different dimpled surfaces, the resolution for the FOV was determined as 283 μm. It is to be noted that, due to the three-dimensional geometry of dimple structure, the resolution of the parts could be reduced, when the surface extend out of the depth of field (DOF) of the camera lens. The DOF depends on the resolution A calculated from FOV, F-number, and focus length L_f of the camera lens. The relationship is [5]

$$\mathrm{DOF} = \frac{2L_\mathrm{f}^2 L_\mathrm{ob}^2 F d}{(L_\mathrm{f}^4 - F^2 d^2 L_\mathrm{ob}^2)}. \tag{3.5}$$

The camera lens used in this study has a focus length $L_\mathrm{f} = 28$ mm and F-number $F = 1.5$. The distance between the lens and objective is $L_\mathrm{ob} = 307$ mm. The circle of confusion d should be no larger than the resolution on the plane (here, $d = A = 283\ \mu$m). In this case, the calculated depth of view is 105 mm and thus is significantly larger than the dimple depth 4 mm, i.e. suitable to cover the entire dimpled surface. The temporal resolution depends on the full frame rate available from the IR camera in use, which is 50 Hz. In this case, the resolution is 20 ms.

In-Situ Calibration

During the calibration, the channel flow was maintained at a flow rate of 11 l/min with a variable reference flow temperature，measured by the thermocouples located at both inlet (TC-1) and outlet (TC-2) of the test section (see Fig. 3.2). Once the system was stable, the averaged IR image was recorded by the IR camera along with recording the flow temperatures via the DAQ system. This process was repeated by changing the flow temperature from 24 ℃ to 50 ℃ at steps of 1 K. The system was determined to be stable by observing the mean IR intensity from the heating surface over time and waiting for the fluctuations and temperature increases to subside into a small range, which took around 20 minutes. Since it is quite difficult to conduct 17 calibration steps in one day, the calibration was divided into two temperature sections: 24 ℃ to 40 ℃ and 34 ℃ to 50 ℃, respectively.

Analysis of Heat Loss During Calibration

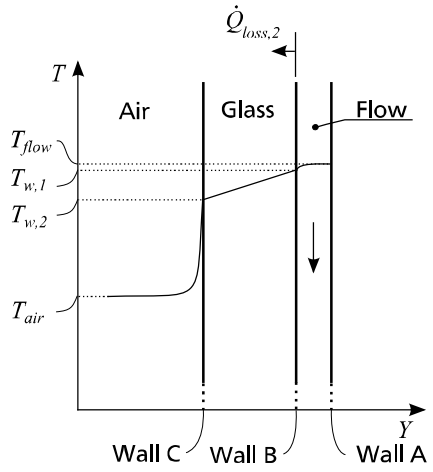

Fig. 3.10: Schematic of temperature distribution between the atmosphere and the heating surface during calibration (without dimple structure).

During calibration, due to the flow temperature being higher than the surrounding and the channel walls, with the exception of the bottom walls, which are considered adiabatic, a heat loss $\dot{Q}_{\mathrm{loss},2}$ from the flow to the ambient air through the glass was found (Fig. 3.10). This heat loss may cause a temperature difference between the wall and flow, causing an error in the calibration of the IR camera. In order to investigate the heat loss of the test section during

calibration, a thin foil thermocouple[20] was attached to the air-side of the window surface (wall C) to measure the temperature $T_{w,2}$. This test was performed under the same condition as the calibration. As a result, the heat loss was calculated from the measured wall temperature $T_{w,2}$ and the mean surface temperature on wall B $\bar{T}_{w,1}$, as determined by the inlet flow temperature (Table 3.7). According to the calculation, the greatest heat loss took place at the highest flow temperature, which is 1.15 W.

Table 3.7: Results of the test for heat loss during calibration

No.	$T_{w,1}$(°C)	$T_{w,2}$(°C)	ΔT(K)	$\dot{q}$ (kW/m^2)	$\dot{Q}$(W)
1.	25.01	24.94	0.07	0.06	0.10
2.	29.94	29.72	0.22	0.18	0.31
3.	39.73	39.28	0.45	0.37	0.63
4.	49.96	48.82	0.82	0.67	1.15

In order to estimate the temperature difference between the wall and flow at this maximum heat loss in the flow, the Nusselt number on the surface of the flow temperature of 50 °C (Pr = 3.568) was calculated. This was achieved by using the Dittus-Boelter equation (equation 2.1) in the case of cooling of the flow ($n = 0.33$) and the Reynolds number $\mathrm{Re_h} = 18265$. As a result, the estimated temperature difference was 0.1 K. Since in this study, the Nusselt number is higher than the value calculated from the Dittus-Boelter equation (see section 5.1), the temperature difference in the calibration was less than 0.1 K and therefore smaller than the measurement error. Accordingly, it was considered negligible and could be ignored in the calibration process.

3.3.3 Measurement Accuracy of Wall Temperature

The accuracy of the wall temperature measurements depends on the camera noise, the accuracy of the thermocouples measuring the flow temperatures, the error from the least squares method, and the error due to heat loss. Since the heat loss during calibration was ignored, the uncertainty of the measurement is:

$$\delta_w^2 = \delta_{TC}^2 + \delta_C^2 + \delta_{fit}^2 \tag{3.6}$$

Since the reference temperature was the mean of the measured value from the two thermocouples which are considered equally precise, the uncertainty of the reference temperature (δ_{TC}) was ± 0.77 K. The error of the measurement with the IR camera (δ_C) was

[20] Self-Adhesive Patch Thermocouple, NiCr-Ni (K), -100C to 200 C, response time 70 ms, Conatex GmbH, St. Wendel/ Germany.

defined by NETD as ± 85 mK of the camera employed in this study. The uncertainty by using fourth ordered polynomial correlation in the least square method (δ_{fit}) was ± 0.03 K. As a result, the uncertainty of the wall temperature measurement was determined to be ± 0.78 K.

3.3.4 Measurement Procedures

The IR image of the heating surface was recorded in two ways: as a single image and an image sequence. In each measurement, the single image presents the averaged image recorded in 10 s. The image sequence includes 2000 frames of IR images recorded over 40 s. Such sequences were not recorded under all the experiment conditions but only in No. 3, 5 and 8 (Table 3.6). Furthermore, in order to record the IR image over a longer time, an image sequence with each frame representing an averaged image over 0.36 s was applied to the measurements for single dimpled surface. In this case, 320 frames of recorded sequence enabled a continuous observation in 115 s.

3.4 Summary

In order to investigate the heat transfer on the dimpled surfaces under different experimental conditions, the experimental setup and measurement for the parameters were adopted. The experimental setup is a loop structure in which deionized water was used as the working fluid. The heat transfer was investigated by observing the wall temperature distribution on the dimpled wall. This wall was placed at the bottom of a rectangular channel and heated through the Joule heating generated from a coated multi-layer film. Single- and double-dimpled surfaces were considered in this study. Furthermore, the dimple Reynolds numbers in this study ranged from $\mathrm{Re_d} = 1 \times 10^4 - 3.5 \times 10^4$. Wall temperature distributions were measured by IR thermography with an accuracy of ± 0.78 K, with a spatial and temporal resolution $A = 283$ µm/pix. and 20 ms, respectively. Other measured parameters are the flow rate, inlet and outlet temperature as well as the heating voltage and current. 12 experimental conditions distinguished by Reynolds number, heat flux, and inlet flow temperature, were investigated in the experiments. In these conditions, averaged IR images and sequences were recorded from the surfaces.

Chapter 4

Data Processing and Uncertainty Estimation

In this chapter, data processing and uncertainty estimation for the experimental parameters are presented. In Section 4.1, the processing method will be introduced separated into three phases: calibration data processing, pre-processing, and experimental data processing. In section 4.2, the uncertainty of the parameters is discussed. A summary concludes the discussion in section 4.3.

4.1 Data Processing

The raw data measured from the experiment was processed into the heat transfer parameters for the next stages of the investigation. Data processing consisted of three phases: calibration data processing, pre-processing and experimental data processing (Fig. 4.1.). In calibration data processing, raw data such as the inlet and outlet flow temperatures ($T_{\mathrm{i,cal}}$ and $T_{\mathrm{o,cal}}$) as well as the IR images ($I_{\mathrm{IR,cal}}(i,j)$) captured during the calibration were used to produce the calibration curves in the form of a pixel-wise calibration matrix $C(i,j)$. In the next phase, IR images ($I_{\mathrm{IR}}(i,j)$) collected during the heating experiment were translated into the temperature distribution with the aid of this calibration matrix. Furthermore, measured values like the flow rate (V), the heating voltage (U), and the heating current (I) were processed to derive the Reynolds number (Re) and the heat flux ($\dot{q}$). In the phase of experimental data processing, the parameters were processed into the Nusselt number distribution ($\mathrm{Nu}(i,j)$) and the mean Nusselt numbers

($\overline{\mathrm{Nu}}_{\mathrm{span}}(i)$ and $\overline{\overline{\mathrm{Nu}}}$). Finally, the correlation of mean Nusselt number and Reynolds number ($\overline{\overline{\mathrm{Nu}}} = f(\mathrm{Re})$) was determined. The data processing was conducted with two MATLAB programs: one program worked on the wall temperature data, the other not only calculated the Nusselt number but also performed the correlations and data analyzing.

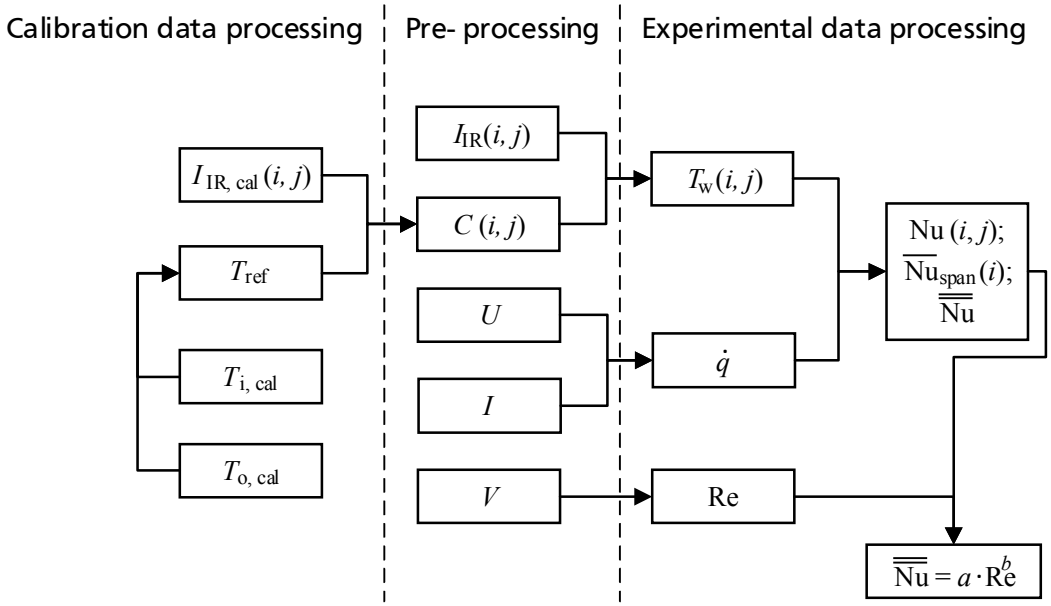

Fig. 4.1: Procedure of data processing.

4.1.1 Calibration Data Processing

At first, reference temperatures T_{ref} were the mean values of the inlet and outlet flow temperatures ($T_{\mathrm{i,cal}}$ and $T_{\mathrm{o,cal}}$). In each calibration step, a reference temperature was set corresponding to a calibration IR image. Since there were 17 steps in each calibration section, the calibration curves resulted from using the least square method on 17 pairs of reference temperature and IR image. The form of the regression model is shown in equation 4.1, which is a fourth order polynomial. The process was conducted for each pixel, then the coefficients were stored in a matrix with their positions corresponding to their pixel positions. Five coefficients of each pixel were saved in a calibration structure C as shown in equation 4.2. In order to keep the use of computing resources manageable, only a part of the viewing area, called the calibrated area, was processed (see Fig. 3.9(b)).

$$T(i,j) = C_1(i,j) \cdot I^4(i,j) + C_2(i,j) \cdot I^3(i,j) + C_3(i,j) \cdot I^2(i,j) + C_4(i,j) \cdot I(i,j) + C_5(i,j); \qquad (4.1)$$

$$C(i,j) = [C_1(i,j), C_2(i,j), C_3(i,j), C_4(i,j), C_5(i,j)]; \qquad (4.2)$$

An example is shown in Fig. 4.2 where three calibration curves at three different positions on the dimpled surface are plotted. The lines are generated from the coefficients of the calibration curves, the dots are the values measured in the calibration. As shown, the calibration curve kept quite close to the calibration data at each pixel. The differences of the curves show that at the same reference temperature IR intensities from different locations are not identical (see section 2.3.2).

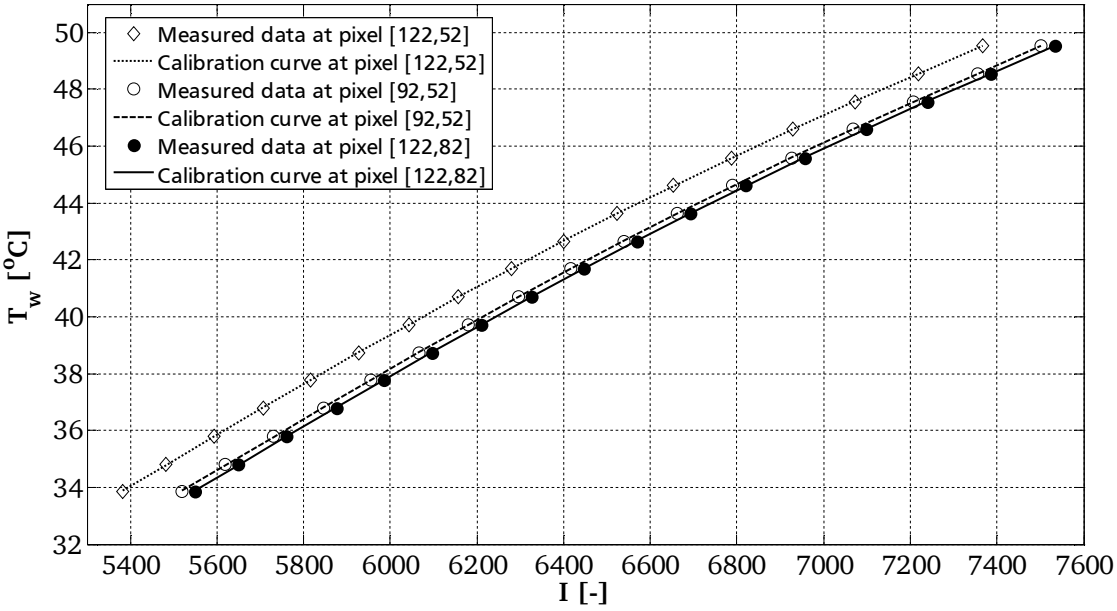

Fig. 4.2: Measured data and calibration curves at three positions on a test surface.

4.1.2 Pre-Processing

IR images ($I_{\mathrm{IR}}(i,j)$) recorded in the heating experiment were translated into the temperature distribution by processing them with the known calibration structure (equation 4.1). Before the processing, the IR images were cut to match the calibration area. The heat flux ($\dot{q}$) was then calculated from the equation:

$$\dot{q} = \frac{\dot{Q}}{s} = \frac{UI}{s_{\mathrm{heating}}}. \tag{4.3}$$

Here, it was assumed that the heat flow from the heating surface to the flow is equal to the total power of the Joule heating (see section 3.2.3) which is determined by the measured voltage and current data. The heating area (s_{heating}) depends on the type of heating surfaces which is listed in Table 3.5. The calculation of the Reynolds number was executed following the equation:

$$Re = \frac{U_0 D}{\nu} = \frac{V}{s_{\mathrm{c}}} \cdot \frac{D}{\nu}. \tag{4.4}$$

As already introduced in section 3.2.2, the mean flow velocity in the channel was calculated from the measured flow rate in the cross section of the channel. Since different characteristic lengths were considered in this study, two types of Reynolds numbers were taken into account (equation 2.4). The kinematic viscosity, a function of the flow temperature, was determined from the VDI-Wärmeatlas [1].

4.1.3 Experimental Data Processing

The Nusselt numbers and correlations were results of the experimental data processing. The processed Nusselt numbers include the two-dimensional distributions and the mean value distributions. The correlations were derived from the regression model of the channel Reynolds numbers and area-mean Nusselt numbers. Furthermore, extra functions were embedded in this processing to determine the measurement resolution, temperature distributions, and local temperature fluctuations in time.

Nusselt Number Distribution

The local Nusselt numbers of the distribution were determined by the equation:

$$\mathrm{Nu}\,(i,j) = \frac{\dot{q} D_\mathrm{h}}{[T_\mathrm{w}(i,j) - T_\mathrm{in}]\lambda_\mathrm{water}}. \tag{4.5}$$

The local temperature ($T_\mathrm{w}(i,j)$) is the value at each position of the temperature distribution. The thermal conductivity was flow temperature dependent and determined by the VDI-Wärmeatlas [1]. The channel hydraulic diameter was used as the characteristic length for calculating the Nusselt number. This characteristic length was also used when calculating the mean Nusselt numbers.

Mean Nusselt Numbers

The mean Nusselt numbers include the spanwise-mean Nusselt number ($\overline{\mathrm{Nu}}_\mathrm{span}$) and area-mean Nusselt number ($\overline{\overline{\mathrm{Nu}}}$). The spanwise-mean Nusselt number is determined by the spanwise-mean temperature measured from the surface (equation 4.6 and equation 4.7). The spanwise-mean Nusselt number is a one-dimensional distribution of the same size as the longitudinal dimension of the calibrated area.

$$\overline{\mathrm{Nu}}_\mathrm{span}\,(i) = \frac{\dot{q} D_\mathrm{h}}{\left[\bar{T}_\mathrm{span}(i) - T_\mathrm{in}\right]\lambda_\mathrm{water}}. \tag{4.6}$$

where,

$$\bar{T}_{\text{span}}\,(i) = \frac{1}{J}\sum_{j=1}^{J} T_{\text{w}}(i,j), \tag{4.7}$$

where J is the total amount of pixels streamwise. The area-mean Nusselt number was calculated from the mean temperature over a selected region in the calibrated area:

$$\overline{\overline{\text{Nu}}} = \frac{\dot{q} D_{\text{h}}}{\left[\bar{\bar{T}} - T_{\text{in}}\right]\lambda_{\text{water}}}. \tag{4.8}$$

where,

$$\bar{\bar{T}} = \frac{1}{I \cdot J}\sum_{j=1}^{J}\sum_{i=1}^{I} T_{\text{w}}(i,j), \tag{4.9}$$

With I is the total amount of pixels spanwise. Both mean Nusselt numbers were processed for evaluating the heat transfer over the heating surface in different aspects. The spanwise-mean Nusselt number focused on the heat transfer distribution streamwise, also taking into account the spanwise influences. The area-mean Nusselt number is used to consider the heat transfer of the complete heating surface. It was used to relate the Reynolds number into the correlation.

Correlation

The correlation results from inserting the channel Reynolds number and area-mean Nusselt number into a function in a form of

$$\overline{\overline{\text{Nu}}} = a \cdot \text{Re}_{\text{h}}^{b}\,. \tag{4.10}$$

The parameters a and b were determined by adopting log-linear regression. The independent variable ($\overline{\overline{\text{Nu}}}$) was a six-element sequence related to the six Reynolds numbers considered in the experiment conditions in which the flow temperature was 35 ℃ and the heat flux was 32 kW/m^2. The independent variable (Re_{h}) was the channel Reynolds number under each condition.

Extra Functions

Aside from the calculations, temperature distributions were analyzed by the extra functions. The first function was conducted on a temperature distribution to determine the resolution of the measurement. It was calculated by dividing the pixel diameter of the dimple's edge by its actual diameter determined by the measurement, which is 15.3 mm. The pixel diameter was derived by the program identifying the dimple's edge on the distribution yielding the center coordinates and diameter of the edge. On the reference surface, since there is no dimple structure, the resolution of this surface was achieved by adopting the measured resolution of the single-dimpled surface.

The second function analyzed the temperature distributions in time. For one thing, the program transferred the recorded IR sequences into the temperature distribution sequences and processed them into an .avi-format movie with various frame rates (fps). For another, the program recorded the temperature fluctuations at four characteristic points inside the dimple. These fluctuations were later plotted in order to analyze the transient temperature fluctuations influenced by the oscillating flow.

4.2 Uncertainty Estimation for the Experimental Parameters

In this section, uncertainty estimations for heat flux, Reynolds number, and Nusselt number are presented. The estimation is based on the accuracy of measured values discussed in Chapter 3. The estimation for heat flux is more complex, because it is not only influenced by the measurement of each value but also influenced by the inhomogeneous heating from the surface.

4.2.1 Heat flux

As introduced in section 3.2.3, the measurement accuracy of the heat voltage and current was $\pm 0.7\%$ and $\pm 2\%$. The uncertainty of the heat flux ($\dot{q}$) was determined within $\pm 2\%$. However, in order to estimate the uncertainty of heat flux, heat loss from heating surface to the surroundings during joule heating and inhomogeneous of heat flux on the surface need to be considered.

Heat Loss During Joule Heating

In the test section, a glass window was fitted into a polycarbonate frame. Since the material is 12 mm thick and has a thermal conductivity of 0.21 W/(m·K)[21], the plastic walls around the glass are all considered adiabatic. However, in order to conduct IR measurements, the window surface of the glass is open to the air and not covered by the insulation material (Fig. 4.3). In this case, the heat loss from the window surface may have had an impact on the measurement. Additionally, the calcium fluoride glass has a thermal conductivity of 9.71 W/(m·K)[22] which is comparable to stainless steel. Thus, the heat loss could be worse.

[21] DIN 52612-1 (http://www.thyssenkrupp-plastics.de/produkte/marken-von-a-z/lexanR/)

[22] From: http://www.crystaltechno.com/CaF2_en.htm

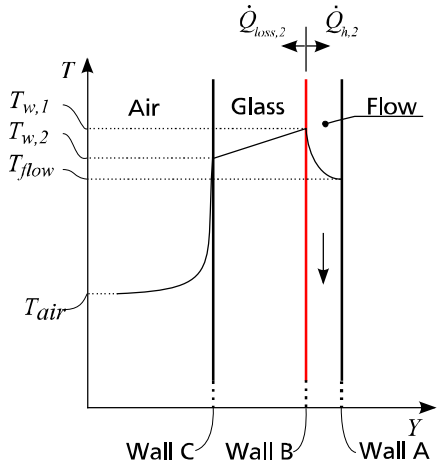

Fig. 4.3: Schematic of temperature distribution between the atmosphere and the heating surface during Joule heating (glass substrate without dimpled structure).

According to the process shown in Fig. 3.8, the heat loss during the heating is estimated by the following equation:

$$\frac{\dot{Q}_{\mathrm{loss},2}}{\dot{Q}_{\mathrm{h},2}} = \frac{(T_{\mathrm{w},1} - T_{\mathrm{air}})/R}{\alpha_{\mathrm{flow}}(T_{\mathrm{w},1} - T_{\mathrm{in}})}, \tag{4.11}$$

where $T_{\mathrm{w},1}$ is the wall temperature on the heating surface (wall B), R is the thermal resistance between the heating surface and the ambient. Considering that wall A is made adiabatic, the thermal resistance is expressed as:

$$R = \frac{1}{\alpha_{\mathrm{out}} s_{\mathrm{C}}} + \frac{t_{\mathrm{BC}}}{\lambda_{\mathrm{glass}} s_{\mathrm{B}}}. \tag{4.12}$$

α_{flow} is the heat transfer coefficient on wall B. The heat transfer coefficient α_{out} on wall C was calculated with the equation of nature convection in the case of bottom side heating [1]:

$$\alpha_{\mathrm{out}} = \frac{\lambda_{\mathrm{air}} \overline{\overline{\mathrm{Nu}}}}{L} = \frac{\lambda_{\mathrm{air}}}{L} \cdot 0.6 \cdot (\mathrm{Ra} \cdot f_1)^{1/5}. \tag{4.13}$$

The factor f_1 is 0.35 based on the air Prandtl number ($\mathrm{Pr} = 0.71$) at 20 ℃ and the Rayleigh number Ra in the current case is 3336.4. Thus, $\mathrm{Ra} \cdot f_1 = 1167.7$ and the airflow is laminar flow. Conductivity of the air λ_{air} is 0.028 W/(mK), and the characteristic length L was calculated as the area of exposed surface divided by its perimeter. As a result, the heat transfer coefficient α_{out} is 6.23 W/(m^{2}K). Considering that the thickness of the glass is 12 mm, areas S_{C} and S_{B} are the same as the heating surface area without the dimple, the thermal resistance of the whole process is 92.96 K/W. Again, based on the Dittus-Boelter equation (equation 2.1), in the case of heating

($n = 0.4$) and Prandtl number and thermal conductivity (λ_{water}) of the flow at $T_{flow} = 35$℃ are 4.833 and 0.622 W/(m·K), respectively, the heat transfer coefficient on wall B is:

$$\alpha_{flow} = 3.106 \cdot \mathrm{Re}_h^{0.4}. \tag{4.14}$$

In this case, the ratio of equation 3.1 is:

$$\frac{\dot{Q}_{loss,2}}{\dot{Q}_{h,2}} = \frac{1}{288.725 \cdot \mathrm{Re}_h^{0.4}} \cdot \frac{T_{w,1} - T_{air}}{T_{w,1} - T_{in}} \tag{4.15}$$

Based on the experimental data of the wall temperature on the flat surface, the calculated results are shown in Table 4.1. Wall temperature $\bar{T}_{w,1}$ is the area-mean temperature measured by IR thermography. The listed four cases are the representative cases in the experiment, including the lowest flow rate (No.1), the highest flow rate (No.2), the highest heat flux (No.3), and the highest flow temperature (No.4). The results show that the heat loss $\dot{Q}_{loss,2}$ did not exceed 0.03% of the heat flow $\dot{Q}_{h,2}$. Therefore, the influence of the heat loss is very low and hence this part of energy loss was ignored in the later calculations and analysis.

Table 4.1: Estimated heat loss in the heating experiment on a flat surface

No.	$\bar{T}_{w,1}$ (℃)	T_{in} (℃)	T_{air} (℃)	Re_h	$\dot{Q}_{loss,1}/\dot{Q}_{h,2}$ (%)
1	43.59	34.89	24.33	5663	0.02
2	38.10	35.05	24.59	19788	0.02
3	43.79	35.02	24.73	11226	0.03
4	48.33	42.79	25.43	11480	0.03

On the other hand, the natural convention on wall C enables the good insulation from the heating part. For this reason, the space below the glass, which is between the camera and the test section, was enclosed by the insulation walls to avoid the influence of movement in the surrounding air (see Fig. 3.4).

Electric Resistance for Heating

The influences of electric resistance for Joule heating are the contact resistance, surface temperature, and water hydrolysis on the heating layer in the flow. As Wagner stated [96], the contact resistance is the extra resistance generated at the contact between the electrodes and heating surface. In order to reduce the influence of this effect, the ITO layer, with a higher resistivity, was used as the heating film in the current study. Compared to the metal foil heating film, the ITO film requires less current when generating the same heat flow. Thus, assuming that

the contact resistances in both cases are the same, there is less Joule heat generated at the contact on ITO film. On the other hand, copper layers and copper foils were used between the electrodes and the ITO layer, which could enhance the contact quality as well. For this reason, the contact resistance is neglected in this study, and the voltage measured between the electrodes was considered as the voltage on the heating surface. With regard to the influence of surface temperature on the electric resistance, Wagner [96] found that its influence on the resistance of metal foil heating film can be neglected. In Fig. 4.4, the distributions of resistance of coated heating films on the plane surface with different surface temperatures are displayed. The temperature range covers all the wall temperatures in the experiment. As a result, the resistance of the coated film heater is independent from the temperature.

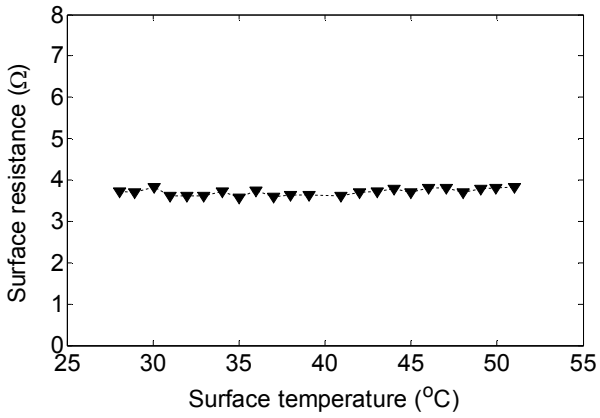

Fig. 4.4: Surface resistance of plane surface by the surface temperature.

Another influence on the electric resistance is due to the hydrolysis of the ITO layer in the water flow. A test has shown that an ITO coating submerged in normal water started reacting with the liquid at a voltage higher than $5V$. In that case, bubbles were generated on the surface, discoloration appeared on the side connected to the cathode, while the resistance of the film increased dramatically. This may be due to the hydrogen bubbles generated on the cathode side of the heating surface decaying the ITO, an oxidized form, to its metal form and therefore causing a permanent change in resistance. To avoid this damage, a dielectric layer made of SiO_2 was deposited on the heating surface, isolating both the layer and the flow. Furthermore, de-ionized water was used as the experiment fluid which can stop the reaction during heating [22]. However, a quite slow damage was still encounter on the ITO layer in the present study even the mentioned protection methods were adopted. For one thing, this is due to the coatings having been deposited on a diffused surface with a roughness of 12 μm, so that the SiO_2 coating may not cover the ITO surface perfectly. A test showed that the resistance measured between the ITO layer and the protection layer with a water film was 1000 times smaller than without the water, which was considered no longer dielectric. Nevertheless, due to the protection of the SiO_2 layer,

the damage to the surface was very slow which allowed the experiments to be carried on for a much longer time period. For another, the deionized water with $20L$ used in the test section, contacting with metal parts like the pump, flow meter and other, was contaminated shortly after the experiment began. For this reason, the water was replaced after each 5 hour in the experiment.

Inhomogeneous Heat Flux Distribution

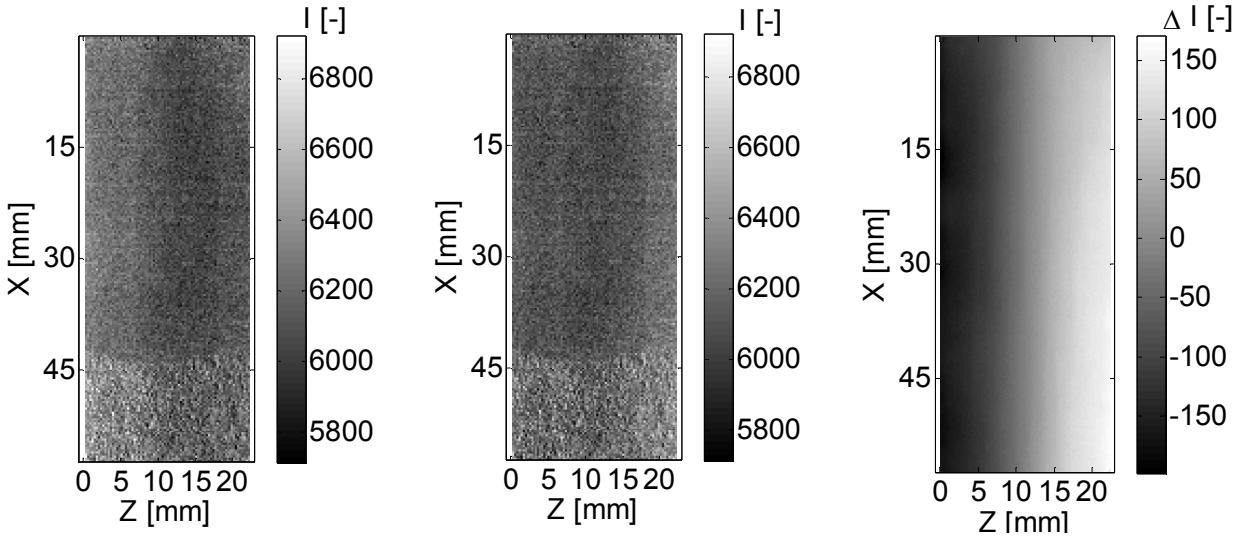

(a) I_{A} (cathode is connected on the left side)

(b) I_{B} (cathode is connected on the right side)

(c) $\Delta I = I_{\mathrm{B}} - I_{\mathrm{A}}$

Fig. 4.5: Inhomogeneous heat flux due to the hydrolysis of the ITO layer in the water flow: (a) and (b) are the raw IR images of the reference surface from two cases with the same experiment conditions but the cathodes connected to different sides, (c) presents the difference between the two cases by subtracting the image from B to A.

In the current measurement method, the heat flux is calculated by dividing the heat flow by the heating surface with the assumption that the heat flux is homogeneous on the surface. The method, similar to the works of Wagner [96] and Schweizer , who used a metal foil to generate a homogeneous heat flux. However, due to the hydrolysis on the heating film and the dimple geometry, the heat flux is inhomogeneous and this has an impact on the results. Figure 4.5 shows the measurement results, influenced by inhomogeneous heating on a flat surface. The raw IR images in the calibrated area are shown in Fig. 4.5(a) and (b). The difference of the two images is shown in Fig. 4.5(c) by subtracting each other. The values deviating from zero indicate the difference between the two cases. As a result, there was always a higher temperature region found in the area, near the cathode side. When the cathode switches, the higher temperature region switches as well. The temperature difference between the sides depends on the heating

power provided from the surface. A large heating power, causes a larger temperature difference. However, considering that the results of the plane surface matched quite closely to the numerical simulation and theory (see section 5.1.2), this influence was limited. Nevertheless, in order to reduce the error caused by these influences, case B, in which the cathode was connected on the right side of the heating surface, was considered as the standard case in the experiment.

Due to the differences of a dimple structure to the flat surface, the resistance in the region becomes inhomogeneous, causing part of the current in the region to go around the dimple. Therefore, as the simulation for the heating on a single-dimpled foil shows in Fig. 4.6(a), an inhomogeneous heat flux distribution is generated on and around the dimpled surface. Furthermore, due to the concave geometry of the dimple, the thickness of the coating during the deposition process could be inhomogeneous, as well. In this case, the local resistance is also influenced inside the dimple. In Fig. 4.6(b), a simulation result compares the coating with homogeneous thickness and shadowing thickness. Due to the insufficient test method, this inhomogeneity has not been determined experimentally. Nevertheless, this inhomogeneity may be the reason for the large difference between the simulation and experimental results on the dimpled surface (see section 5.2).

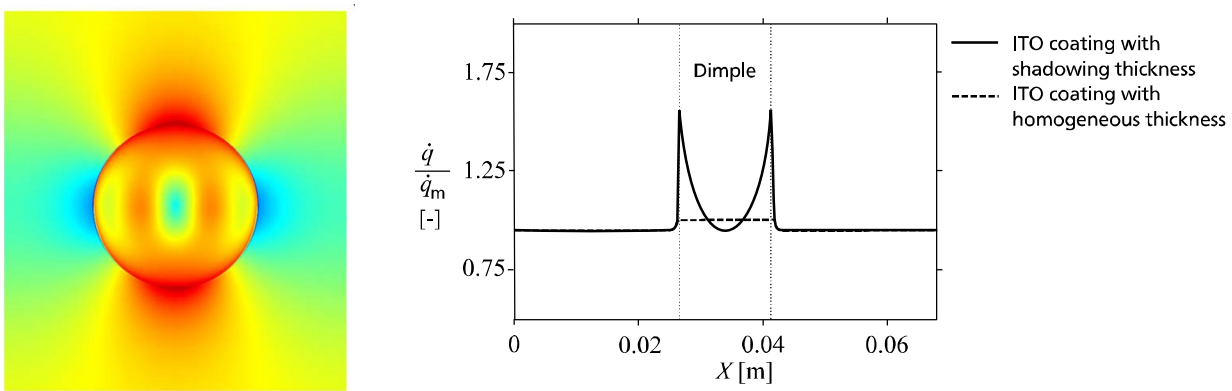

Fig. 4.6: Inhomogeneous heating on the dimpled surface: (a) the pattern of heat generation on the dimpled coating surface [74], (b) distribution of heat flux compared with different ITO coating (according to [20]).

4.2.2 Reynolds Number

As mentioned in section 3.2.2, the measurement accuracy of the flow rate is between ±4% and ±0.5% in the experimental flow rate range. According to the IAPWS' released formulation [83], the uncertainty for determined the viscosity is ±1%. Since the uncertainty for determine

channel cross section and characteristic length is ignored, the Reynolds number has an uncertainty between $\pm 1\%$ and $\pm 4\%$.

4.2.3 Nusselt number

The uncertainty of the Nusselt number primarily depends on the uncertainty of the heat flux, the temperature difference between the wall and the flow and the thermal conductivity of the water. Here since the heat flux is determined by assuming that the heat flux distribution on the surface is homogenous, the uncertainty of the heat flux in this study is thus $\pm 2\%$. The uncertainty of the temperature difference was determined by the measurement accuracy of the measurements of wall and flow temperature which were $\pm 0.77\ K$ and $\pm 0.78\ K$, respectively. There, the uncertainty was $\pm 1.1\ K$. The relative uncertainty of the temperature difference depends on the value of this parameter, varying from $1.48\ K$ to $13\ K$. Thus, the relative uncertainty of the temperature difference was from $\pm 8.4\%$ to $\pm 74.3\%$. The uncertainty of the thermal conductivity is $\pm 0.7\%$ according to the IAPWS' released formulation [84]. As a result, the uncertainty of the Nusselt number was between $\pm 8.7\%$ to $\pm 74.3\%$.

4.3 Summary

In this chapter, data processing was introduced in three aspects: calibration data process, pre-processing and experimental data processing. As a result, the temperature distribution, Nusselt number distribution, mean Nusselt numbers, and the correlation were determined for subsequent analysis. Additionally, in the experimental data processing, extra functions were performed in order to determine the resolution of the measurements and processing the movies or distributions into time-dependent sequences and local/mean values. Based on the calculations for each experimental parameter, the uncertainties of these parameters were evaluated with $\pm 2\%$ for heat flux (by assuming homogenous heat flux distributed on the surface), $\pm 1\% - \pm 4\%$ for the Reynolds number, and $\pm 8.7\% - \pm 74.3\%$ for the Nusselt number. The large uncertainty of the Nusselt number was due to the temperature differences, which were too small in the reattachment zones on the heating surface (see section 5.2) compared to the uncertainty of the temperature difference.

Chapter 5

Results and Discussion

The experimental results are presented and discussed in four sections regarding the convective heat transfer on a reference surface and dimpled surfaces, the influence of experimental parameters, and the time-dependent analysis. In section 5.1, the temperature and Nusselt number distributions on a non-structured surface (plane surface), which is considered as the reference for the dimpled surfaces, are discussed. In the next two sections, the results of the single- and double-dimpled surfaces are considered. Similar to the case of the reference surface, the temperature and Nusselt number distributions are used in the section 5.2 to discuss the heat transfer on the surfaces. Then, the heat transfer enhancement of the dimpled surfaces is analyzed by the Nusselt number ratio (Nu_d/Nu_{pl}), which is presented in local distributions and mean distributions to show that the influence of the dimple geometry. In section 5.3, the effects of the experimental parameters, such as the Reynolds number, heat flux, and inlet flow temperature, are taken into consideration. Finally, transient temperature distributions are investigated in a time sequence, and the heat transfer fluctuations are determined.

5.1 Heat Transfer on the Reference Surface

The reference surface, which has the same printing surface area as the dimpled surfaces, was placed into a flow with the same conditions and was measured with an equalized heat flux. This case is categorized as asymmetric heating in a channel flow, which is hydraulically fully developed but is thermally developing. As a result, two-dimensional distributions of temperature and Nusselt numbers on this surface give a general impression of the heat transfer across the

surface. Then the local Nusselt number distributions and spanwise-mean Nusselt number distributions are presented for a detailed evaluation. The simulation result is compared to the local Nusselt number streamwise. Finally, the distribution of the area-mean Nusselt number versus the Reynolds number is correlated and compared to the empirical correlation.

5.1.1 Temperature and Nusselt Number Distributions

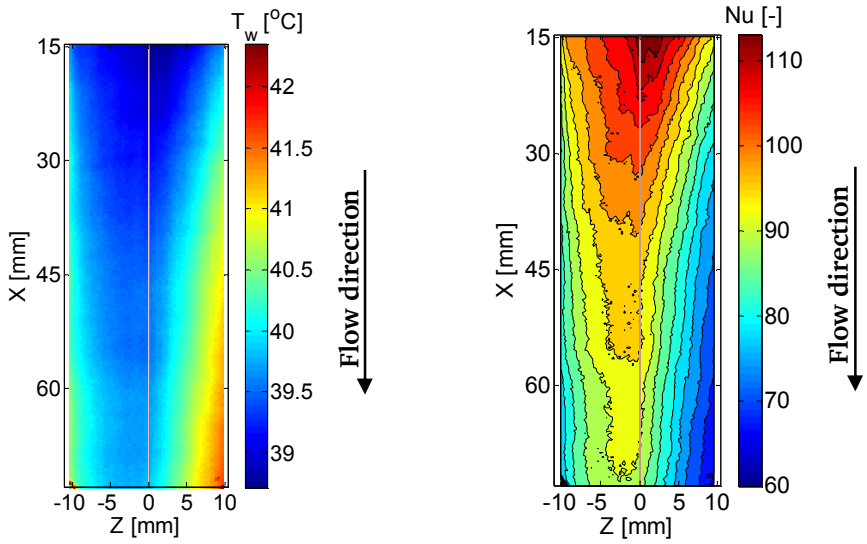

(a) Temperature distribution (b) Nusselt number distribution

Fig. 5.1: Wall temperature and Nusselt number distributions on the flat surface under the reference condition ($\mathrm{Re_d} = 2 \times 10^4, T_{\mathrm{in}} = 35\ ^{\circ}\mathrm{C}$ and $\dot{q} = 32\ \mathrm{kW/m^2}$).

Two-dimensional distributions of temperature and Nusselt number at the reference condition ($\mathrm{Re_d} = 20000$, $T_{\mathrm{in}} = 35\ ^{\circ}\mathrm{C}$, $\dot{q} = 32\ \mathrm{kW/m^2}$) are shown in Fig. 5.1. The temperature distribution is translated from an IR image, averaged over 10 s. The Nusselt number distribution is calculated from the temperature distribution with equation 4.5. As shown in Fig. 5.1(a), the wall temperature, which gradually increases from inlet to downstream, suggests a developing thermal boundary layer on the heating surface. Spanwise, the temperature is the highest near the center of the heating surface and shrinks the further it gets from the center. This means that the thermal boundary layer is influenced by the sidewalls where the local flow velocity is lower than that of the mainstream. Therefore, the heat transfer is lower, and the wall temperature raises. Furthermore, the spanwise distribution is asymmetric in most of the area and symmetric near the inlet. This asymmetric distribution is because of the inhomogeneous heating due to the hydrolysis on the heating surface. Since the right side of the heating surface is connected to the cathode, a higher heat flux is generated locally and, consequently, raises the local temperature. At the inlet, since the wall temperature is quite close to the flow temperature and has less influence from the inhomogeneous heat flux, the temperature distribution is symmetric. The

distribution at the inlet also indicates that the flow structure of the inlet flow is symmetric. In the Nusselt number distribution shown in Fig. 5.1(b), the Nusselt number is reduced in several V-shaped regions. Near the inlet, that region is quite small but has the highest value of around 113. Then the region is stretched and expanded streamwise and spanwise by reducing the value to around 75. The lowest value of around 60 is located at one side of the outlet.

In Fig. 5.2, the Nusselt number distributions streamwise and spanwise are plotted. In the streamwise distribution (Fig. 5.2(a)), both the local Nusselt number on the centerline and the spanwise-mean Nusselt number are displayed. On the centerline, it is reduced from 110 to 90 with a difference of 20 between the inlet and outlet. The spanwise-mean Nusselt number indicates the influences in the spanwise direction. In the distribution, due to the heat transfer near the sidewalls being lower than in the center, the spanwise-mean Nusselt number is lower than the local Nusselt number on the centerline. The distribution decreases from 106 to 82 with a difference of 24 which is similar to the local distribution. A small fluctuation presents at the location A in Fig. 5.2(a) is due to the inhomogeneous heating. In the same location, the magnitude of the fluctuation is much smaller in the mean value distribution, showing that the influence is only a local effect with a limited impact on the heat transfer from the entire surface.

The spanwise distributions of the local Nusselt number are shown in Fig. 5.2(b). The three distributions are different from the distance to the trailing edge of the heating surface. Meanwhile, these locations are related to the positions of the dimple's front edge, center, and rear edge on the single dimpled surface. In three positions, the maximum Nusselt number drops from 105 to 94. It should be noted that in the same spanwise position, the decrease of the Nusselt number is not linear streamwise. This indicates that in the downstream thermal boundary layer, there is a trend for it to become fully developed. Again, influenced by the inhomogeneous heating, the Nusselt number distribution is different from left to right. On the right side of the centerline, where the heat flux is homogeneous, the Nusselt number sharply increases near the sidewall and gradually in the center. This shows that the influence of the walls affect the thermal boundary layer to be comparatively thicker near the walls and thinner towards the center. This pattern is similar to the simulation result in a similar case reported by Isaev et al. [30]. Furthermore, in streamwise direction, the Nusselt number near the walls does not decrease that much on the left side, indicating that the increase of thermal boundary layer is occurring more slowly near the wall than in the center. On the left side, the distribution is almost linear. This could be due to the Nusselt number being strongly influenced by the inhomogeneous heat flux at this side, which decreases from the cathode to the center of the heating surface. In this case, the region with a higher heat flux has a lower Nusselt number. Furthermore, in streamwise

direction, the Nusselt number is nearly identical at the two sides for $X = 28.2$ mm. There, the value on the left is decreasing by increasing the X. This suggests that the higher heat flux is continuous on the left side and has an accumulated influence on the local heat transfer.

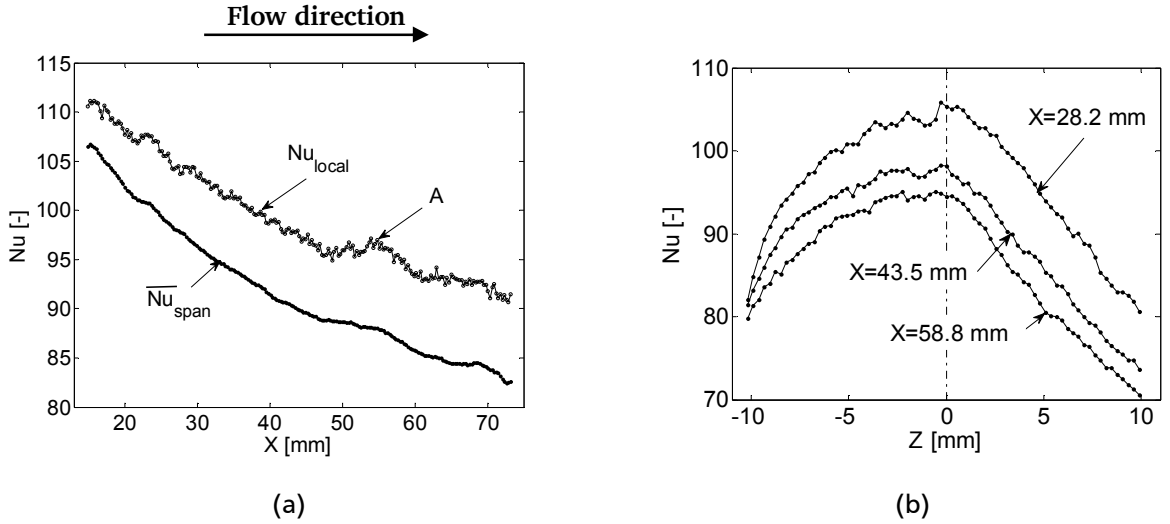

Fig. 5.2: Nusselt number distributions: (a) streamwise distribution and spanwise-mean Nusselt number distribution on centerline, (b) spanwise distributions at different positions of X in flow direction ($\mathrm{Re_d} = 2 \times 10^4, T_{\mathrm{in}} = 35\ ^{\circ}\mathrm{C}$ and $\dot{q} = 32\ \mathrm{kW/m^2}$).

5.1.2 Influence of the Reynolds Number

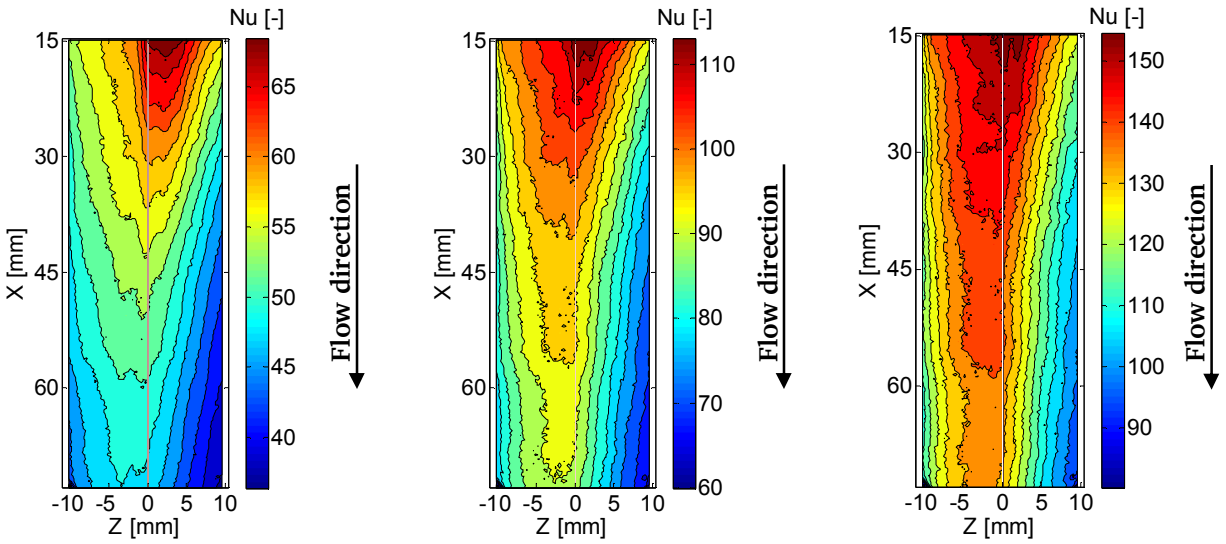

Fig. 5.3: Nusselt number distributions on the flat surface for different Reynolds numbers ($T_{\mathrm{in}} = 35\ ^{\circ}\mathrm{C}$ and $\dot{q} = 32\ \mathrm{kW/m^2}$)

As shown in Fig. 5.3, the influence of the Reynolds number on heat transfer is significant. The maximum local Nusselt number for the lower Reynolds number is 68.5, which is about 60.1% of the maximum value of the reference case. For higher Reynolds number, the value is 154.6 and

thus 137% of the reference case value. This is because an increase of the Reynolds number triggers turbulence in the boundary layer and thus promotes the mixing which increases the heat transfer. The V-shaped iso-lines being similar suggest that the flow structures above the heating surface may be similar for different Reynolds numbers. In this case, the spanwise-mean Nusselt number decreases in a similar pattern for different Reynolds numbers (Fig. 5.4 (a)). In the spanwise direction, since the influence of the increasing Nusselt number near the wall is intensified at higher Reynolds numbers, the distribution for these is a bit more curved (Fig. 5.4(b)). This shows that the thermal boundary layer influenced by the wall becomes narrow when the Reynolds number is increased.

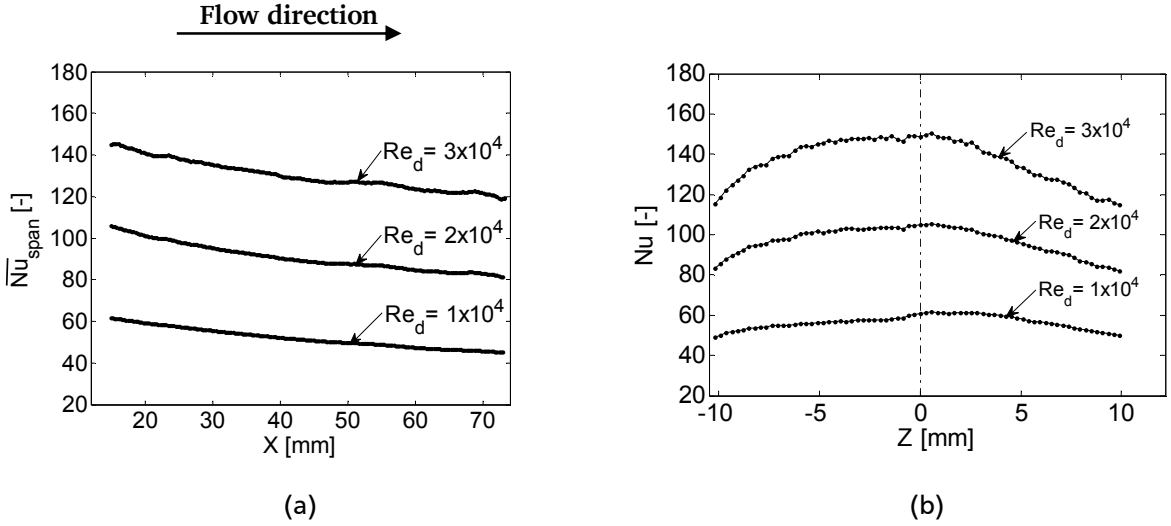

Fig. 5.4: Nusselt number distributions on the flat surface for different Reynolds numbers ($T_{\mathrm{in}} = 35\ ^{\circ}\mathrm{C}$ and $\dot{q} = 32\ \mathrm{kW/m^2}$): (a) spanwise-averaged Nusselt number distributions, (b) local Nusselt number distributions in spanwise direction ($X = 28.2\ \mathrm{mm}$).

The streamwise Nusselt number distribution was also confirmed by simulation results [43]. The simulation was conducted by using the RANS method with the identical channel geometry, flow properties, and experimental conditions. The comparison between the experimental and simulation result are shown in Fig. 5.5. According to the distributions, the two results are close to each other with a deviation of up to 16.4%. Since the heat flux in the simulation was assumed to be homogeneous and the bottom side of the heating wall was adiabatic, the small difference between the experimental results and simulation results may be due to the imperfect nature of the experimental conditions. Nevertheless, since the uncertainties of the Nusselt number in these two experiments are within $\pm 12\% - \pm 28\%$ and thus cover the maximum deviation, the validation can be confirmed.

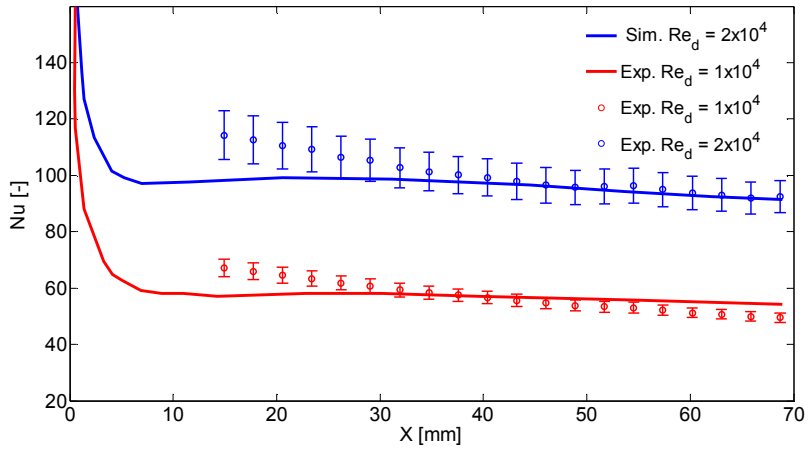

Fig. 5.5: Comparison with the simulation results [43].

In order to characterize the heat transfer influenced by the Reynolds number, the area-mean Nusselt number is plotted against the channel Reynolds number (Fig. 5.6). Additionally, a correlation,

$$\overline{\overline{\mathrm{Nu}}} = 0.0357 \cdot \mathrm{Re_h}^{0.84}, \tag{5.1}$$

was derived by using the regression model mentioned in section 4.1.3. This correlation is displayed in the figure as a blue-colored smooth line. The condition of this correlation is the heat transfer of an asymmetric heated channel flow, which is hydraulically fully developed but thermally still developing, which can be described by an empirical correlation reported by Kakaç et al. [47]:

$$\frac{\overline{\overline{\mathrm{Nu}}}_\mathrm{e}}{\mathrm{Nu}_\infty} = 1 + \frac{0.9756}{(X/D_\mathrm{h})^{0.760}}, \tag{5.2}$$

where Nu_∞ is determined by equation 2.1 ($n = 0.4$), X defined as the total length of the investigated heat transfer area in streamwise direction is 74 mm in the current study. Since the inlet flow temperature $T_\mathrm{in} = 35\,°\mathrm{C}$, the Prandtl number $\mathrm{Pr} = 4.833$ is determined from the Wärme atlas [1]. Thus, the empirical correlation is:

$$\overline{\overline{\mathrm{Nu}}}_\mathrm{e} = 0.0514 \cdot \mathrm{Re_h}^{0.8}, \tag{5.3}$$

As shown in figure 5.6, the correlation from the experiment and the empirical correlation are a good match. This shows that the influence of the inhomogeneous heat flux has less influence on the area-mean heat transfer from the surface. Furthermore, it also supports the assumption that the heating power P is equal to the heat flow $\dot{Q}_{\mathrm{h},2}$. Small deviations (up to 3.5%) found at higher

Reynolds numbers are probably due to the high uncertainty, which rose along with the Reynolds number.

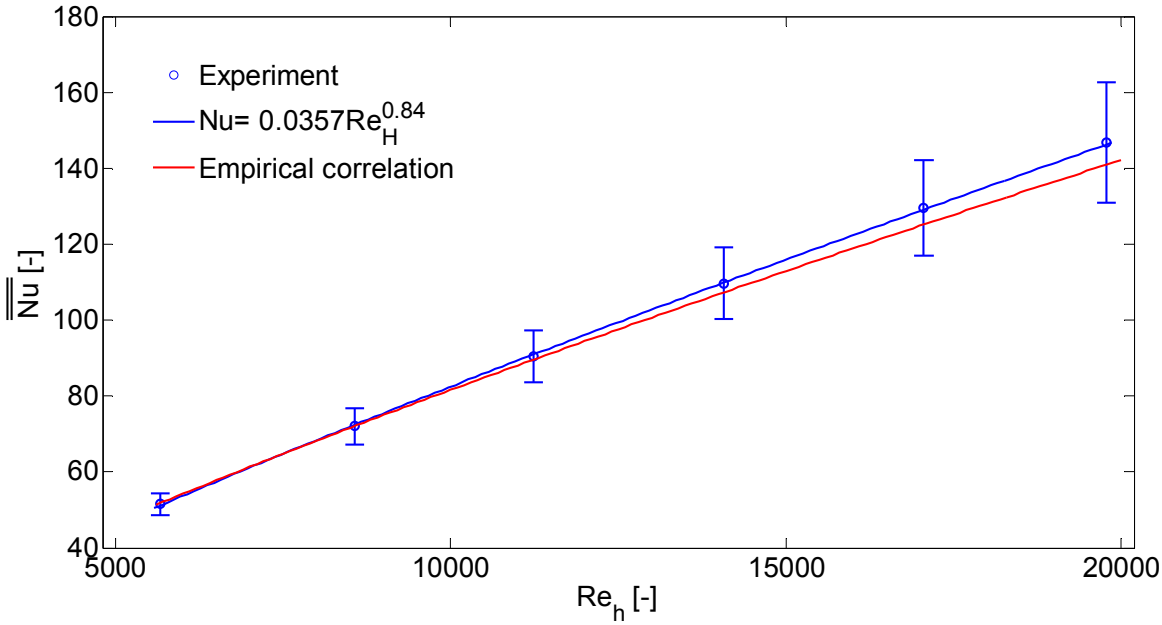

Fig.5.6: Effect of the Reynolds number on the area-mean Nusselt number distribution on the flat surface ($T_{\text{in}} = 35$ ℃ and $\dot{q} = 32$ kW/m^2).

5.2 Heat Transfer on the Dimpled Surfaces

The experiment on single- and double-dimpled surfaces, measured under the reference condition ($\text{Re}_{\text{d}} = 2 \times 10^4$, $T_{\text{in}} = 35$ ℃, $\dot{q} = 32$ kW/m^2), is presented in this section. Furthermore, the Nusselt number ratio is discussed by comparing it with the value on a plane surface.

5.2.1 Single-Dimpled Surface

Wall temperature distributions of a single-dimpled surface under the reference condition are shown in Fig. 5.7(a). On the flat region before the dimple area, the effects are similar to those on the plane surface in that a thermal boundary layer is developing along the streamwise direction. Under the influence of the dimple structure, three temperature regions were identified in the dimple region and its wake, which are shown in Fig. 5.7 (b). In the dimple region, the recirculation zone was found close to the front edge with a typical banana-shaped formation. The temperature in this zone was around 40 ℃ which is similar to the temperature on the flat region but higher than in other parts of the dimple region. Two high temperature regions were located at the sides, symmetrical to each other. As expected, influenced by the inhomogeneous heat flux, the temperature of one peak on the left side is always higher than that on the other side. The reattachment zone, covering the rear side of the dimple surface, was a symmetric area

with a temperature of around 38 ℃. The lowest temperature value was found in a region, called the reattached region, near the rear dimple's edge and close to the centerline. After the dimple, the wall temperature in the wake gradually increased in the streamwise direction from the rear dimple's edge.

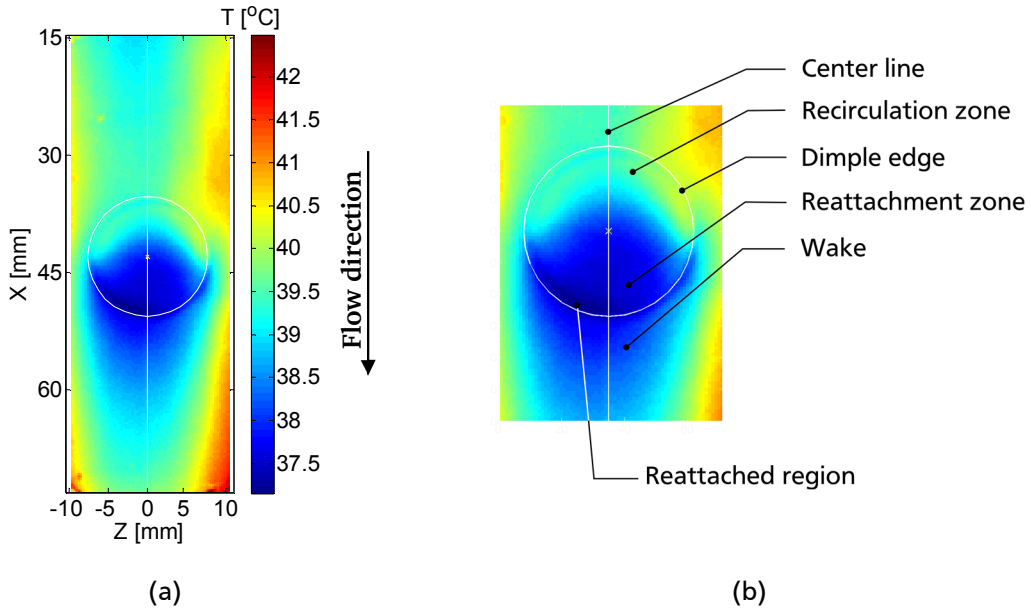

Fig. 5.7: Wall temperature and Nusselt number distributions on the single-dimpled surface under the reference condition ($\mathrm{Re_d} = 2 \times 10^4, T_{\mathrm{in}} = 35\ ^{\circ}\mathrm{C}$ and $\dot{q} = 32\ \mathrm{kW/m^2}$).

The presence of these three zones confirms the heat transfer mechanism, which is determined by the flow structure in the dimple. According to the flow structure described by Presser [73] and Terekhov et al. [88] (see Fig. 2.5), in the central plane of the dimpled surface, the separated flow reattaches on the rear side of the dimple area and creates a circulation inside the dimple area while the boundary layer redevelops behind the structure. Corresponding to the identification of a maximum heat transfer region on the dimpled bottom near the rear edge where the continuous reattachment takes place [92], the lowest temperature was formed in the reattachment zone. Due to the reversed flows, starting from the reattachment zone upstream, the wall temperature in this zone increased sharply against the flow direction. When close to the dimple's front edge, the reversed flow detaches from the surface and forms the vortex structure in the dimple . As a result, the local heat transfer becomes worse in that region [56], and accordingly, causes the higher wall temperature in the recirculation zone. In the wake, due to the high turbulence level generated by the separated boundary layer, the heat transfer is enhanced just after the dimple's rear edge and reduced downstream with the flow redeveloping [41]. Off the center plane, because of the dimple geometry, a transverse vortex cell is formed in the dimple, causing the banana-shaped hot zone where the heat transfer is weakened [92].

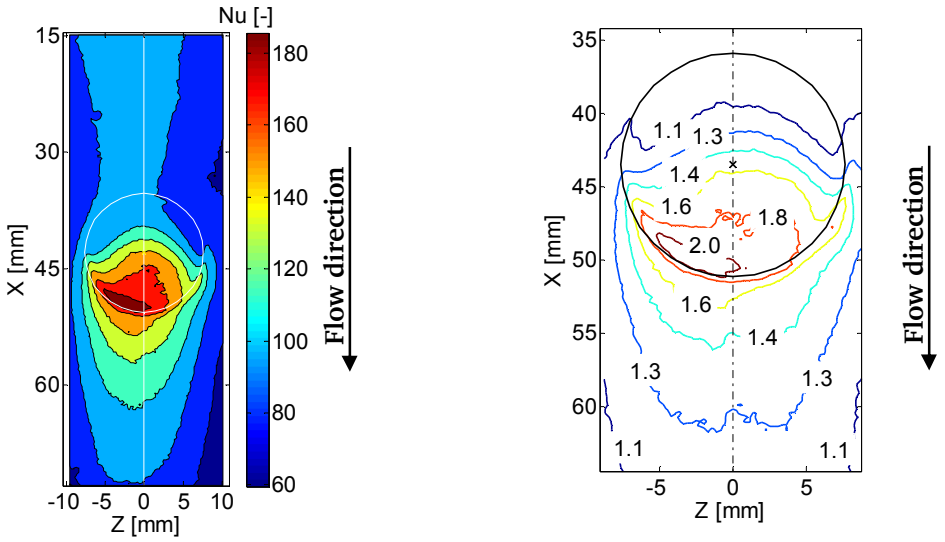

(a) (b)

Fig. 5.8: Heat transfer distributions on the single-dimpled surface ($\mathrm{Re_d} = 2 \times 10^4, T_{\mathrm{in}} = 35\ ^{\circ}\mathrm{C}$ and $\dot{q} = 32\ \mathrm{kW/m^2}$): (a) Nusselt number distribution, (b) isometric lines of Nusselt number ratio $Nu_{\mathrm{d}}/Nu_{\mathrm{pl}}$ (part of the calibrated area).

The Nusselt number distribution on the single dimpled surface is shown in Fig. 5.8(a). As expected, the local maximum value is found in the reattachment zone near the rear edge. While the region with lower values located near the inlet edge is almost equal to the Nusselt number on the plane surface upstream, the minimum Nusselt number on the right side of the region is probably caused by the inhomogeneous heating. Behind the rear edge of the dimple, the Nusselt number drops to a value of around 150 and decreases gently downstream. The distribution inside the dimple is similar to the experimental results reported by Terekhov et al. [56, 92]. Furthermore, the heat transfer rate distribution ($\mathrm{Nu_d/Nu_{pl}}$) displayed in Fig. 5.8(b) indicates the presence of heat transfer enhancement on the dimpled surface by comparing it to the reference surface. Along the flow direction, the Nusselt number ratio increase from the front dimple's edge forward to reach a maximum value in the reattachment zone, where the greatest value is around $\mathrm{Nu_d/Nu_{pl}} = 2.1$. In the wake region, the isometric lines become blunt compared to the Nusselt number distribution. It seems as if the dimple structure affects an additional influence on the boundary layer generated from the sidewalls so that the Nusselt number near the center plane drops more slowly than on the plane surface. This distribution is comparable to the simulation results reported by Isaev et al. [30]. However, unlike the simulation results, the asymmetric distribution of Nusselt number ratio in the reattachment zone was not observed in the experimental result. This may be due to the displayed experimental result being an averaged

distribution gathered over 10 s. In this case, the divergence may have been caused by the low frequency oscillations of the wall temperature (see section 5.4.2).

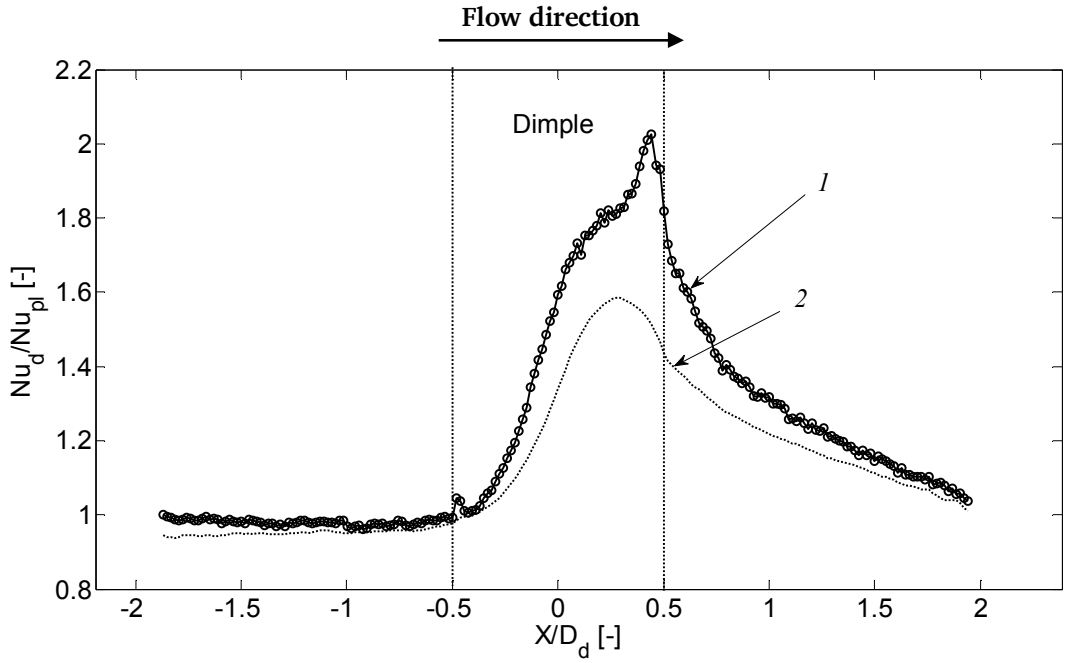

Fig. 5.9: Streamwise Nusselt number ratio distributions ($\mathrm{Re_d} = 2 \times 10^4, T_{\mathrm{in}} = 35\ ^{\circ}\mathrm{C}$ and $\dot{q} = 32\ \mathrm{kW/m^2}$): 1- local distribution on the centerline ($\mathrm{Nu_d/Nu_{pl}}$), 2- spanwise-mean distraction ($\overline{\mathrm{Nu}}_{\mathrm{span,d}}/\overline{\mathrm{Nu}}_{\mathrm{span,pl}}$).

The streamwise Nusselt number ratio distributions are shown in Fig. 5.9. Curve 1 is the local heat-transfer-rate distribution on the longitudinal centerline of the dimpled surface, while curve 2 is the distribution of spanwise-mean values along the streamwise direction (see section 4.1.3). As expected, after the dimple's front edge ($X/D = -0.5$), the local Nusselt number ratio rises sharply from $\mathrm{Nu_d/Nu_{pl}} \approx 1$ to the local maximum value $\mathrm{Nu_d/Nu_{pl}} = 2.0$ near the rear edge ($X/D \approx 0.4$). After that location, the Nusselt number ratio drops dramatically and reaches a value comparable to the flat surface downstream at a distance of twice the dimple-printing diameter from the structure center. Again, compared to the simulation results reported by Isaev et al. [30], the profiles of the distributions are quite similar. However, there are also big differences inside the dimple. In the simulation, the Nusselt number ratio is quite small near the front part of the dimple ($\mathrm{Nu_d/Nu_{pl}} < 1$) and has a maximum of $\mathrm{Nu_d/Nu_{pl}} \approx 3.5$. Furthermore, the Nusselt number ratio increases gradually for most of the dimple region and rises sharply near the rear edge. However, in the experimental result, the increase is sharp in the dimple region and rises at a relatively moderated rate behind the dimple center. It is possible that in the experiment, the wall temperature distribution, especially at extreme temperatures, was defused by the tangential conduction of the glass substrate. Furthermore, due to the inhomogeneous

heating in the dimple, the local Nusselt number rose close to the center of the dimple (see section 4.2.1). In the figure, the distribution of the spanwise-mean values shows a similar pattern to the local distribution. However, the spanwise-mean Nusselt number distribution shown in Fig. 5.9 is also smaller than the centerline distribution, especially around the maximum heat transfer region. This suggests that the heat transfer enhancement due to the reattachment only has a local influence in the spanwise direction, even though the mean Nusselt number ratio reaches a maximum of $\overline{\mathrm{Nu}}_{\mathrm{span,d}}/\overline{\mathrm{Nu}}_{\mathrm{span,pl}} = 1.6$.

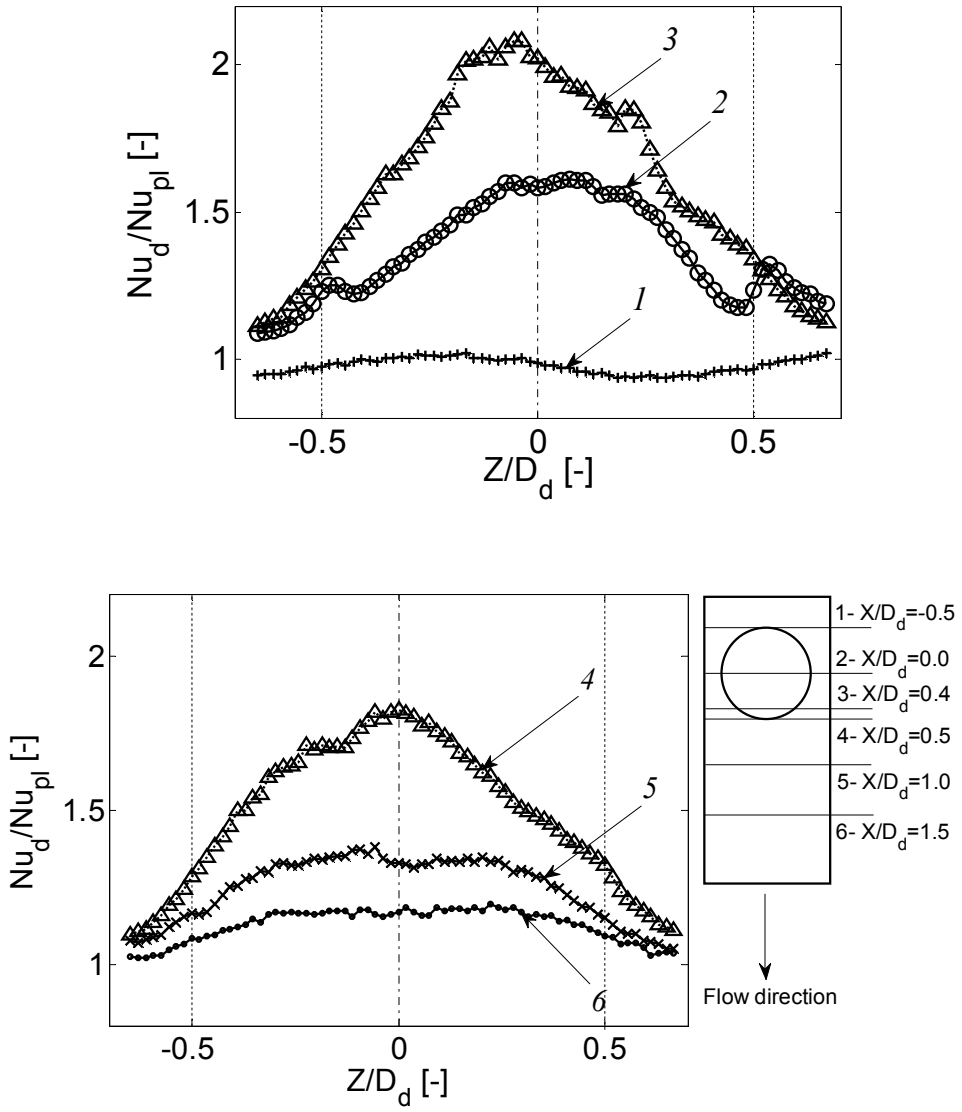

Fig. 5.10: Spanwise distributions at the different locations on the single dimpled surface.

Figure 5.10 shows the spanwise distributions at different streamwise locations of the dimpled surface. The distribution is similar to that of the plane surface at the dimple's front edge. In the center of the dimple, the distribution shows a typical profile reported by the simulation and

experimental studies [30, 92]. This profile has a peak at the center and two smaller valleys aside, adjacent to the dimple's edges. This is due to the two recirculation flows of the vortex extending to the sides of the dimple at the spanwise center plane and having a low enhancement in heat transfer. However, because of the high velocity in the center part, a significant enhancement can be found here [92]. Curve 3 is the distribution near the dimple's rear edge where the maximum local Nusselt number ratio is located in the streamwise direction ($X/D_\mathrm{d} = 0.4$). It should be noted that, the dimple's edges at the sides are located at $Z/D_\mathrm{d} = \pm 0.3$. In the distribution, the maximum Nusselt number ratio is on the left side of the center plane and a little higher than the value in the center. In the wake, the local Nusselt number ratio drops abruptly from the location at $X/D_\mathrm{d} = 0.4$ to that close to $X/D_\mathrm{d} = 1$ and decreases at a relatively even pace downstream. It is likely that the turbulence level induced by the dimple decays far more quickly in the wake where the flow redevelops. Meanwhile, the major influence of the dimple structure in the wake is near the centerline of the surface. This suggests that the heat transfer of a dimple structure can be enhanced by placing another dimple upstream in the same centerline.

5.2.2 Influence of the Upstream Dimple

The heat transfer enhancement influenced by the upstream dimple was investigated by conducting the measurements on the double-dimpled surface. As a result, the Nusselt number distribution and the heat transfer rate distributions determined under the reference condition are shown in Fig. 5.11. The Nusselt number distributions of the first and second dimple show a comparable pattern, similar to the single-dimpled surface (Fig. 5.8(a)). Furthermore, the larger heat transfer area with Nu > 180 found in the first dimple is probably due to a thinner thermal boundary layer at this location, which is quite close to the leading edge of the heating surface.

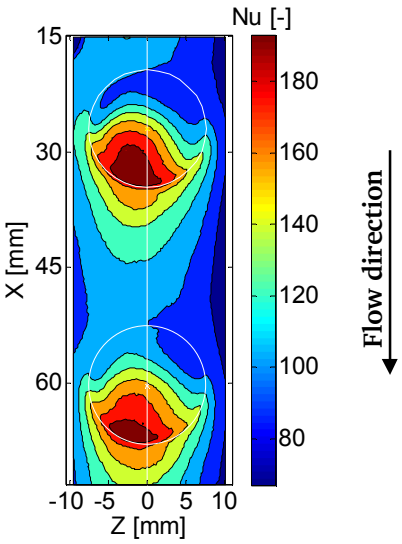

(a) Nusselt number distribution

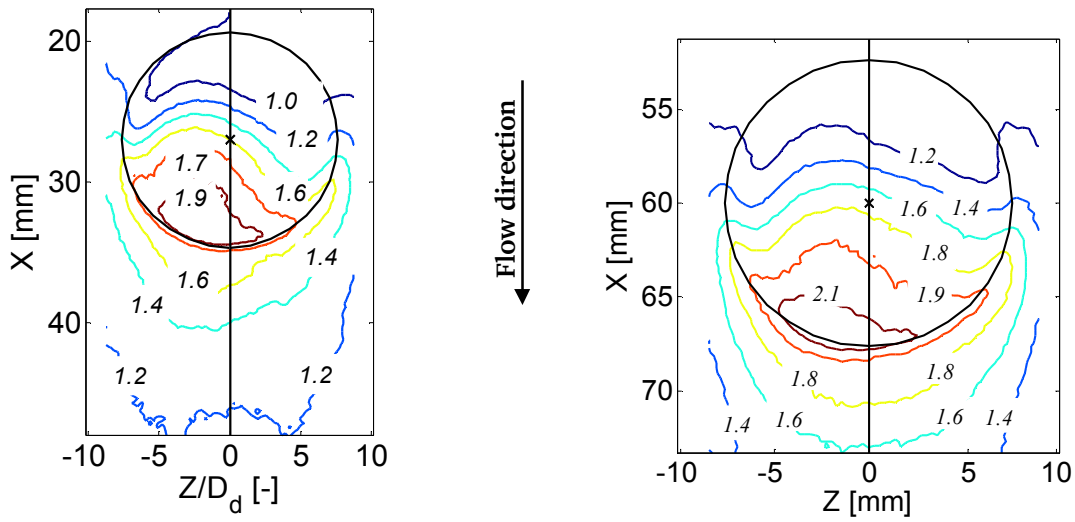

(b) $\mathrm{Nu_d/Nu_{pl}}$ (c) $\mathrm{Nu_d/Nu_{pl}}$

Fig. 5.11. Nusselt number distributions and Nusselt number ratio distributions on the double-dimpled surface under the reference condition ($\mathrm{Re_d} = 2 \times 10^4, T_{\mathrm{in}} = 35\ ^\circ\mathrm{C}$ and $\dot{q} = 32\ \mathrm{kW/m^2}$): (a) Nusselt number distribution; (b) isometric lines of Nusselt number ratio on and around the first dimple (1st-D); (c) isometric lines of Nusselt number ratio on and around the second dimple (2nd-D).

As expected, in the heat-transfer-rate distribution plotted in Fig. 5.11(b) and (c), the isometric lines show identical patterns in each dimple region. Furthermore, compared to the first dimple, the Nusselt number ratio of the second dimple is generally higher. It is likely that the greater enhancement value is due to the existence of the upstream dimple as considering that Nusselt number reduces downstream due to the developing thermal boundary layer. In the streamwise distributions of the Nusselt number ratio shown in Fig. 5.12 (a), the local and spanwise-mean Nusselt number ratios of the second dimple are always higher than those of the upstream dimple at comparable positions. The maximum of the local Nusselt number ratio of the second dimple is $\mathrm{Nu_d/Nu_{pl}} = 2.2$, which is 10% greater than the front dimple. For the same reason, the maximum spanwise-mean value of this dimple ($\overline{\mathrm{Nu}}_{\mathrm{d}}/\overline{\mathrm{Nu}}_{\mathrm{pl}} = 1.8$) is 12% larger than the first one. It is similar to the conclusion presented by Isaev et al. [35] that the heat transfer is enhanced by rows. Moreover, Terekhov et al. [90] reported an intensification of the heat transfer in the structure by placing a non-heated dimple with the same geometry upstream and an enhancement of the heat transfer coefficient of up to 28% at a similar distance between the dimples. In the local Nusselt number distribution displayed in Fig 5.12 (b), the Nusselt number at the dimple's inlet edge of the second dimple is larger than that of the first. However, the maximum Nusselt numbers in two dimples are nearly the same. Compared to the Nusselt number distribution of the reference surface under the same condition, in which the Nusselt number drops streamwise, the difference between the Nusselt numbers is enlarged in the streamwise direction. Thus, the

identical Nusselt number peaks are compensated by the streamwise decrease of the Nusselt number and caused the higher Nusselt number ratio in last dimple.

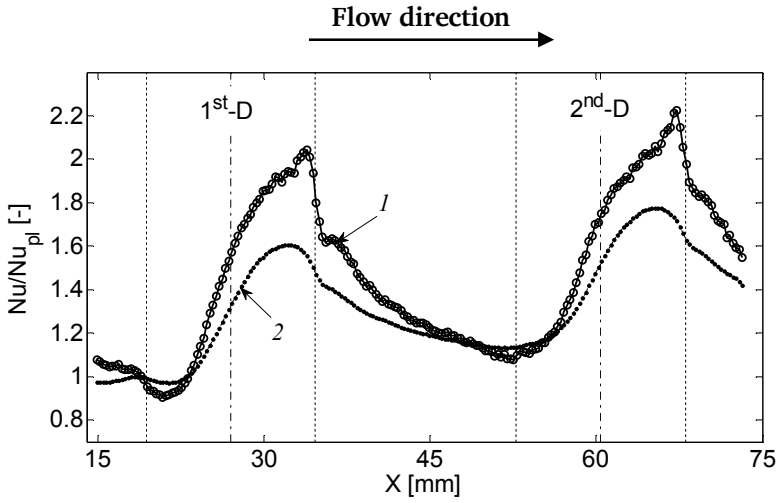

(a) Heat transfer rate distribution

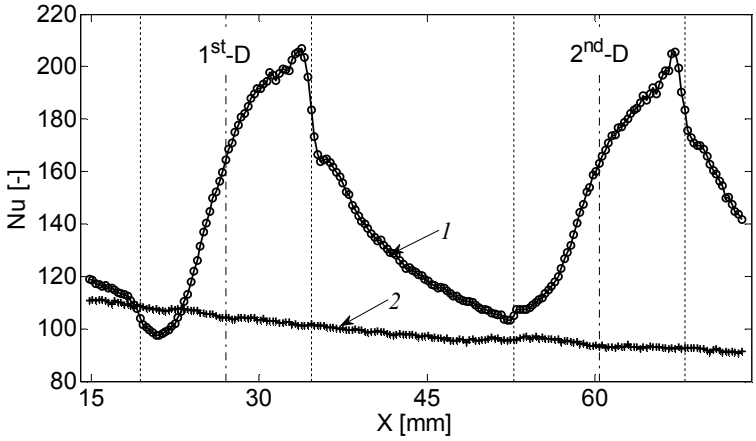

(b) Local Nusslet number distribution

Fig. 5.12. Streamwise Nusselt number and heat transfer rate distributions: (a) heat transfer rate distributions: 1- centerline distribution; 2- spanwise-mean distribution; (b) local Nusselt number distributions on the centerline: 1- double-dimpled surface; 2- reference surface.

According to Terekhov et al. [90], this enhancement is due to the turbulence induced by the upstream dimple. As shown in Fig. 5.13, the Nusselt number ratio of the second dimple is always higher than that of its upstream counterpart in the spanwise direction. In this case, the disturbance of the flow has a broad spanwise influence.

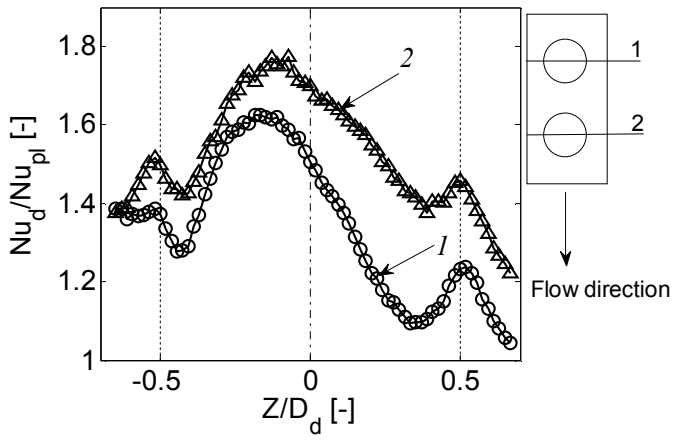

(a) centerline distributions

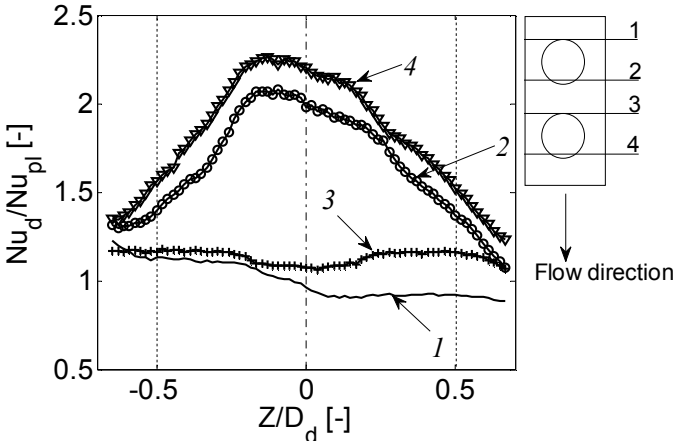

(b) distributions at different locations

Fig. 5.13: Spanwise distributions on the double dimpled surface, (a) centerline distribution: 1- in the second dimple, 2- in the first dimple, (b) distributions at different locations: 3- front edge of the first dimple, 4- front edge of the second dimple, 1- the location of the maximum in streamwise distribution in the first dimple, 2- the location of the maximum in streamwise distribution in the second dimple,

The heat-transfer-rate distributions on the centerline of these two dimples are shown in Fig. 5.13(a). The maximum of the second dimple is 1.8 in the spanwise distribution across the dimple center, which is 12.5% higher than that of the first dimple. The distribution in the first dimple is not symmetric to the distribution of the second dimple. This is probably due to the inhomogeneous heating, strongly influencing the right side of the heating surface. Except for this influence, the heat-transfer-rate distributions at the inlet of each dimple are quite similar to each other on the left side of the center plane (Fig. 5.13(b)). Therefore, the thickness of the thermal boundary layers at the inlet edge of the dimples is similar to each other. Accordingly, the strong enhancement ratio of the second dimple shows that the higher turbulence level has a greater impact on the heat transfer in the dimple region than on that of the flat surface. Finally, unlike

the centerline distribution, the distributions on the maximum streamwise positions are similar in shape. In this case, the influence of the inhomogeneous heating could have disappeared. This is present because this influence can be minimized in the higher heat transfer region.

5.3 Effects of Experimental Parameters

In this section, the influences of the three experimental parameters on the heat transfer of the dimpled surface are discussed. These parameters are the Reynolds number, the inlet flow temperature, and the heat flux. The results for different Reynolds numbers ranging from 1×10^4 to 3.5×10^4 on the single-dimpled surface and the double-dimpled surface are considered in section 5.3.1. Then the influence of the inlet flow temperature, varied from 35 ℃ to 43 ℃, and of the heat flux, varied from 18 kW/m^2 to 53 kW/m^2, is discussed.

5.3.1 Effect of the Reynolds Number

Single-Dimpled Surface

Along with the Reynolds number increasing in the turbulent flow, the heat transfer grows due to the stronger turbulence level, thinning the thermal boundary layer. In the same manner, the Nusselt number on the dimpled surface is raised to a higher level at larger Reynolds numbers (Fig.5.14 (a-c)). The patterns of the distribution in and behind the structure are nearly the same for all Reynolds numbers. This suggests that no significant change of the induced flow structures occurs within the investigated range. As for the heat transfer enhancement, the corresponding heat-transfer-rate distributions reveal that the enhancement in the reattached region and the wake becomes weaker at higher Reynolds numbers, while remaining nearly the same in other parts. In other words, the heat transfer on the reference surface in these regions grows faster in the Reynolds number range than on the dimpled surface. Furthermore, the Nusselt number ratio in the recirculation zone, which is almost constant for different Reynolds numbers, suggests that the structure of the vortex is independent from the Reynolds number. In the wake, the ratio stays close to the experiment of Terekhov et al. [88] in that the 'tongue'-shaped isometric region becomes short and narrow in spanwise and streamwise direction, respectively, when the Reynolds number increases. Additionally, at higher Reynolds numbers, the downstream end of the isometric region of heat-transfer-rate distribution is blunt compared to the case of $Re_d = 1 \times 10^4$. This is probably due to the influence of the switching mode of the vortex inside the dimple (see section 5.4.2).

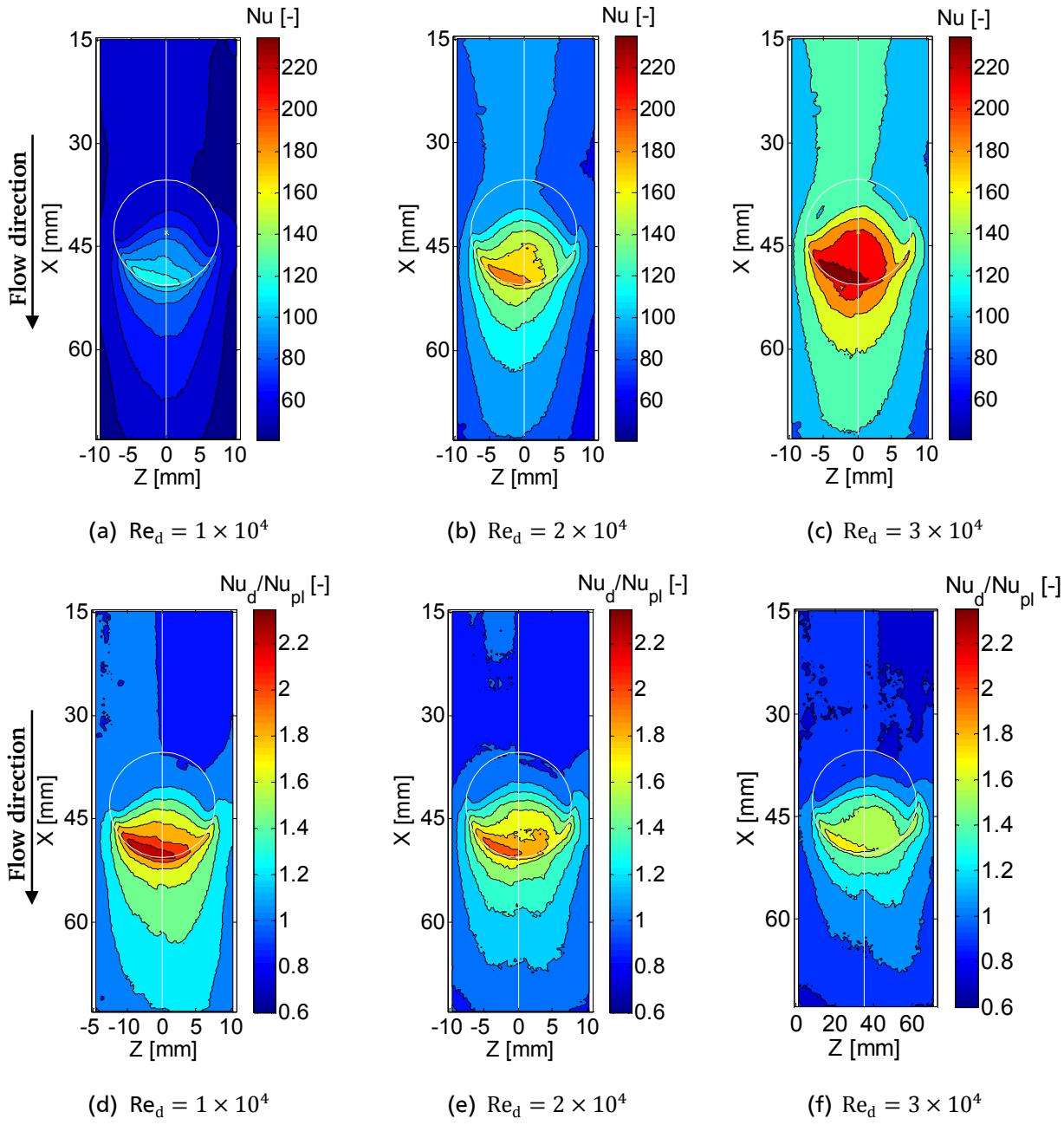

Fig. 5.14: Nusselt number and Nusselt number ratio distributions on the single-dimpled surfaces at different Reynolds numbers ($T_{in} = 35\,^{\circ}C$ and $\dot{q} = 32\ \mathrm{kW/m^2}$): (a-c) Nusselt number distributions, (d-f) Nusselt number ratio distribution.

In the streamwise Nusselt number distributions on the centerline shown in Fig. 5.15(a), the local Nusselt number reaches a maximum of 250 near the rear edge at $\mathrm{Re_d} = 3 \times 10^4$. It is 29% greater than the maximum of the reference condition ($\mathrm{Re_d} = 2 \times 10^4$). Compared to the case at $\mathrm{Re_d} = 1 \times 10^4$, the maximum of the reference condition is 55% larger. Additionally, the distributions in the downstream half of the dimple are more flat at higher Reynolds numbers. This shows that the area of the reattachment zone is much larger at higher Reynolds numbers

(see Fig. 5.14(a-c)), illustrating that the unstable reattached flow is intensified both in momentum and size.

The streamwise Nusselt number ratio displayed in Fig. 5.15 shows that the influence of the Reynolds number affects primarily the region from the dimple center downstream. It should be noted that the small difference of the distributions on the upstream plane surface is due to the uncertainty in determining the Nusselt number ratio. Besides, the same trend is found in the spanwise-mean value distributions. It partly follows the simulation results reported by Isaev et al. [30], which show a similar behavior in the reattachment zone. In the distributions, the maximum Nusselt number ratio is found at the lowest Reynolds number with a value of $\mathrm{Nu_d/Nu_{pl}} = 2.3$. This maximum is 15% greater than the maximum under the reference condition and nearly the same as the ratio between the maximums of reference condition and higher Reynolds number. This suggests that the Nusselt number ratio at the peaks shrinks in a linear progression proportional to the increase of the Reynolds number.

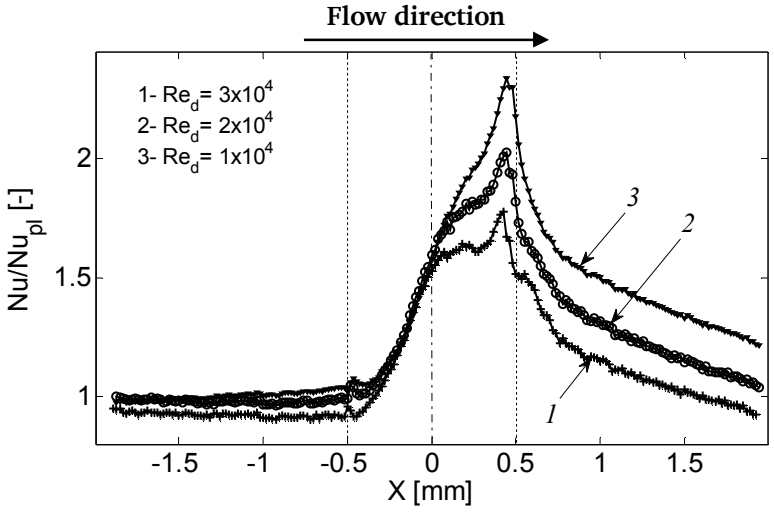

Fig. 5.15: Streamwise distributions of Nusselt number ratio on the single-dimpled surface at different Reynolds numbers ($T_{\mathrm{in}} = 35\ ^{\circ}C$ and $\dot{q} = 32\ \mathrm{kW/m^2}$).

The spanwise Nusselt number distributions on the spanwise centerline are presented in Fig. 5.16(a). The distributions are nearly symmetrical near the dimple center where the maximum rate is located. However, near the right dimple's edges, a secondary peak becomes identical when the Reynolds number increases. This suggests that the vortex structure at $\mathrm{Re_d} = 1 \times 10^4$ is still symmetric in a time-averaged observation, while moving to the right and causing an asymmetric formation at higher Reynolds numbers. In the wake, the spanwise heat transfer rate decreases when the Reynolds number rises. As shown in Fig. 5.16(b), at $\mathrm{Re_d} = 1 \times 10^4$, there are still some enhancement effects on the plane surface downstream of the dimple's rear edge,

despite nearly matching the reference surface at $\mathrm{Re_d} = 3 \times 10^4$. Similarly, the distribution becomes asymmetric at higher Reynolds numbers. In this case, the asymmetric vortex structure in the dimple retains its influence in the wake. It is likely that an outgoing jet generated on the right side of the dimple spanwise center plane affects the wake and enhances the local heat transfer.

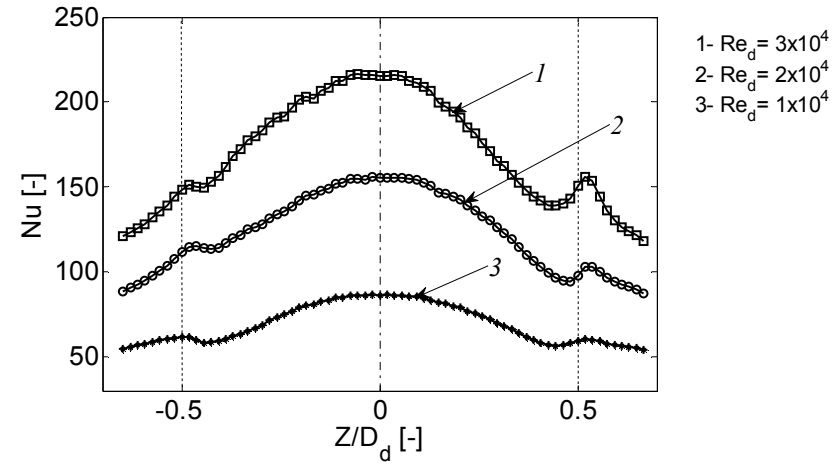

(a)

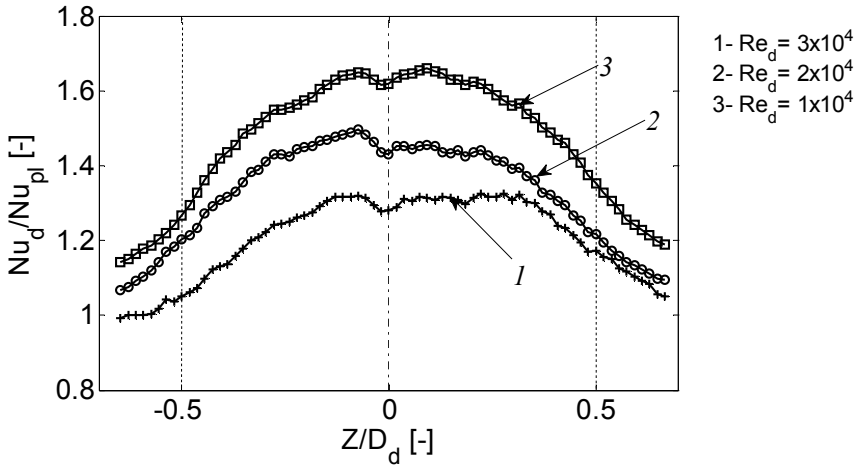

(b)

Fig. 5.16: Spanwise distributions at different Reynolds numbers, (a) Nusselt number distributions at the centerline ($X/D_\mathrm{d} = 0$), (b) Nusselt number ratio distributions in the wake ($X/D_\mathrm{d} = 0.7$).

The area-mean Nusselt number distributions shown in Fig. 5.17 quantify the heat transfer of the dimple region and wake against the Reynolds number. The dimpled area is a square with its four sides tangential to the dimple region. In the wake area, a rectangular region of the size $1.2D_\mathrm{d} \times 1.4D_\mathrm{d}$ was chosen adjacent to the rear dimple's edge. In the investigated Reynolds range ($\mathrm{Re_d} = 1 \times 10^4 - 3.5 \times 10^4$, equivalent to $\mathrm{Re_h} = 0.6 \times 10^4 - 2 \times 10^4$), the mean Nusselt number

increases with a rising Reynolds number in both areas. However, the distribution of the dimple area is considerably larger than that of the wake region. Compared to the distribution on the reference surface, the distribution of the dimple area is almost parallel to the reference distribution, suggesting that the enhancement due to the dimple structure is nearly constant in the Reynolds number range. On the other hand, the distribution of the wake area is close to the reference distribution at a high Reynolds number. This indicates that the intensification in the wake, due to the pulsating flow, decreases with the turbulent level increasing at higher Reynolds numbers.

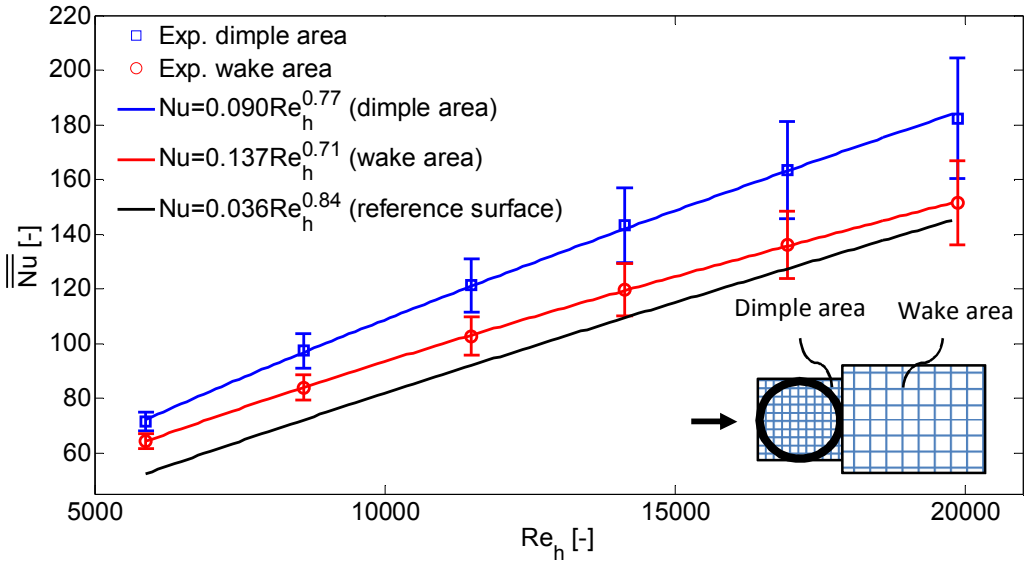

Fig. 5.17: Correlations for heat transfer on dimpled surfaces

As a comparison, the heat-transfer-rate distributions of the mean Nusselt numbers in different areas are shown against the Reynolds numbers in Fig. 5.18. As expected, the ratio of both areas decreases along with a rise of the Reynolds number. The ratio of the dimple area reduced from 1.36 at $Re_d = 1 \times 10^4$ to 1.20 at $Re_d = 3.5 \times 10^4$. In the wake, this ratio drops from 1.34 to 1.06 at the same Reynolds number range. There is a 20% enhancement in the dimple region at the maximum Reynolds number. However, in the wake, the enhancement reaches only 6%. The distribution in the wake is comparable to the experimental result reported by Terekhov et al. [89]. Nevertheless, the distribution in the dimpled area is quite different compared to the previous study of the author [92]. This is probably due to the inefficient heat flux in the dimple structure. Besides, experimental conditions, which are different in the two experiments, may have influenced the results.

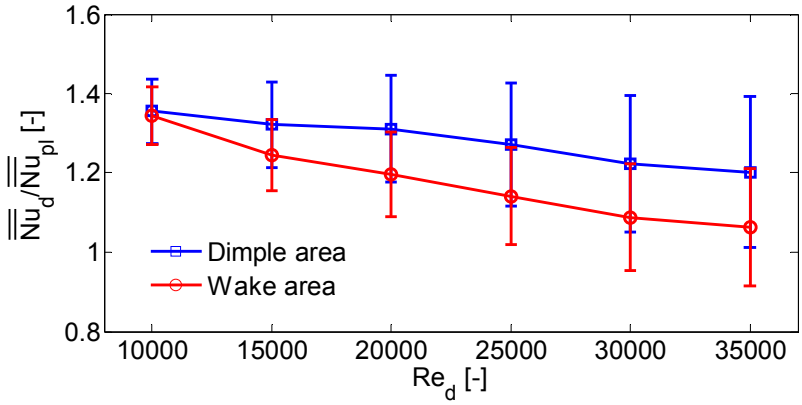

Fig. 5.18: Distributions of the mean Nusselt number ratio on different areas of the single-dimpled surface.

Based on the correlations of the mean Nusselt number distributions shown in Fig. 5.17, the Nusselt number ratios of the two areas can be:

$$\overline{\overline{Nu}}_{dimple}/\overline{\overline{Nu}}_{ref} = 2.5Re_h^{-0.07}\,, \tag{5.4}$$

$$\text{and } \overline{\overline{Nu}}_{wake}/\overline{\overline{Nu}}_{ref} = 3.8\,Re_h^{-0.13}. \tag{5.5}$$

Thus, at the reported highest Reynolds number ever investigated [88], which is $Re_d = 2 \times 10^5$ ($Re_h = 1.2 \times 10^5$), the Nusselt number ratio of the dimple area is 1.1, which still shows an enhancement of 10% over the plane surface. Considering that the mean heat transfer rate may be influenced by the area difference between the dimple surface and the plane surface (reference), a surface factor of

$$\xi = s_d/s_{dp}, \tag{5.6}$$

according to Terekhov et al. [92], is adopted to compensate for the difference. In this study, since the dimple geometry is fixed, this factor constantly remains at 1.27. The Nusselt number ratio concerning the influence of the area difference ranges from 2.03 to 1.52 in the investigated Reynolds number range and the predicted enhancement ratio at the highest Reynolds number is 1.40.

According to equation 5.5, this could be no enhancement ($\overline{\overline{Nu}}_{wake}/\overline{\overline{Nu}}_{ref} = 1$) in the wake area if the Reynolds number is higher than $Re_d = 3.1 \times 10^4$ ($Re_h = 1.8 \times 10^4$). This ratio is a little different from the result shown in Fig. 5.18. It is because that the reference Nusselt number of the correlation and the experimental result are based on a part of the heating surface. Further,

since the enhancement in the wake could be either higher or equal to the reference, this equation is finally considered no longer available as the Reynolds number exceeds $\mathrm{Re_d} = 3.1 \times 10^4$.

Double-Dimpled Surface

Compared to the heat-transfer-rate distributions shown in Fig. 5.19, the same phenomena as on the single-dimpled surface were observed on the double-dimpled surface as well. Especially in the reattachment zone and the wake of each dimple, the Nusselt number ratio decreases in size and magnitude with increasing Reynolds number. The patterns of the distribution in the second dimple are similar at different Reynolds numbers. In this case, it seems that the flow structure in this dimple shows no influences from the Reynolds number as well as the upstream dimple. Furthermore, at higher Reynolds numbers, the values of local maximum rates in each reattachment zone of the dimples are more equalized.

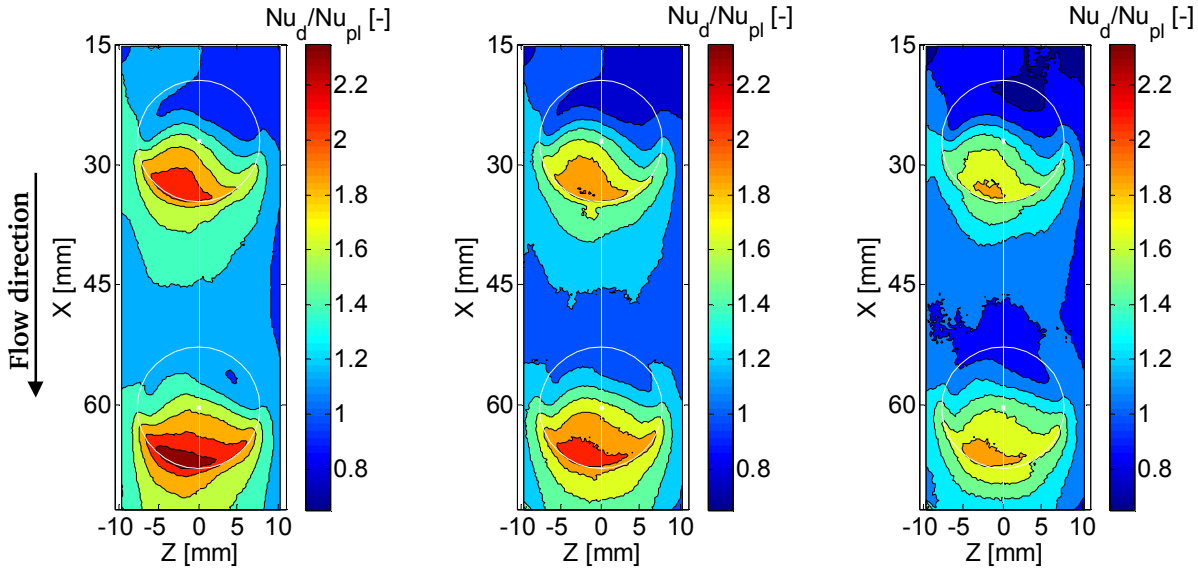

(a) $\mathrm{Re_d} = 1 \times 10^4$ (b) $\mathrm{Re_d} = 2 \times 10^4$ (c) $\mathrm{Re_d} = 3 \times 10^4$

Fig. 5.19: Nusselt number ratio distributions on the double-dimpled surfaces at different Reynolds numbers ($T_{\mathrm{in}} = 35\ ^{\circ}\mathrm{C}$ and $\dot{q} = 32\ \mathrm{kW/m^2}$).

In the streamwise distributions shown in Fig. 5.20, the local Nusselt number ratio shrinks when the Reynolds number increases. In the second dimple, the Nusselt number ratio is higher than in the first dimple in the investigated Reynolds number range at the inlet edge of each dimple. The distributions in two dimples are similar to each other. However, the maximum Nusselt number ratio in the second dimple at higher Reynolds numbers is comparable to the rate on the first dimple. It should be noted that, the Nusselt number ratio on the surface upstream of the first dimple at the Reynolds number $\mathrm{Re_d} = 1 \times 10^4$ is considerably higher than that of the reference surface. This is due to the inhomogeneous heat flux on the heating surface, which is worse on

the double-dimpled surface. In this case, a strong heat flux difference between the left and right side of the surface was encountered in the plane regions upstream of first dimple and downstream of second dimple and caused an abnormal value on the inlet plane. Accordingly, this effect may also be affecting the Nusselt number ratio in the wake of the second dimple. However, since the influence of the inhomogeneous heat flux is limited at higher heat transfer coefficient, the influences in the second dimple's wake and in the cases of higher Reynolds numbers are no more significant.

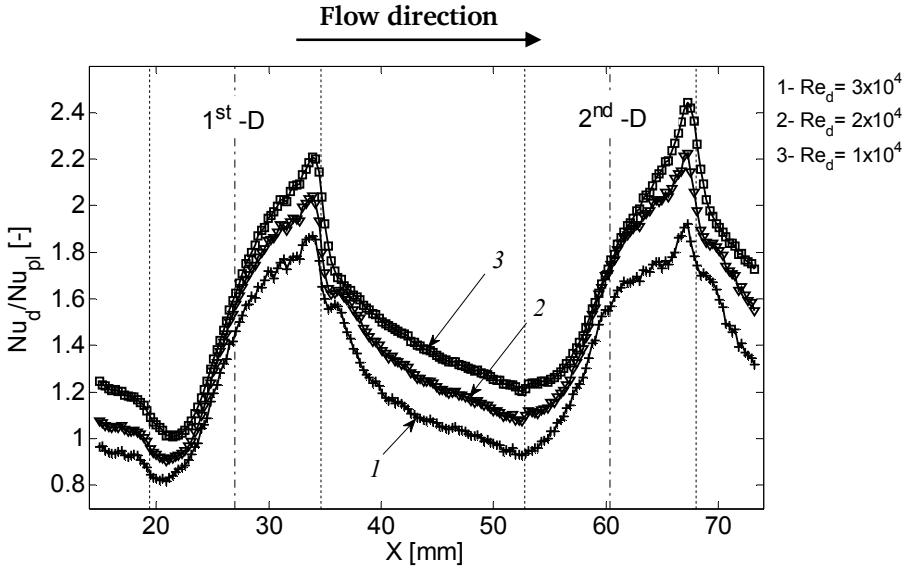

Fig. 5.20: Nusselt number ratio distributions on the double dimpled surfaces at different Reynolds numbers ($T_{\mathrm{in}} = 35\ ^{\circ}\mathrm{C}$ and $\dot{q} = 32\ \mathrm{kW/m^2}$).

Table 5.1: Comparison of the maximum Nusselt number ratios in different dimples

Dimple Reynolds number ($\mathrm{Re_d}$), [-]	$\left(\mathrm{Nu_d/Nu_{pl}}\right)_{\mathrm{max}}$, [-]		Difference of maximum Nusselt number ratio (Δ, [-])
	1st -dimple	2nd -dimple	
1×10^4	2.2	2.4	0.2
2×10^4	2.0	2.2	0.2
3×10^4	1.9	2.0	0.1
3.5×10^4	1.9	1.9	0

The local maximum values in the dimple regions at different Reynolds numbers are listed in Table 5.1,. At lower Reynolds numbers, the difference between the local maximum is 0.2. However, at $\mathrm{Re_d} = 3.5 \times 10^4$, this value is as low as zero. As mentioned for single-dimpled surfaces, the heat-transfer-enhancement region in the wake shrinks streamwise along with the increase of the Reynolds number. Here, it is probably the same effect that influences the local

maximum in the centerline of the second dimple. Nevertheless, the area-mean distributions displayed in Fig. 5.21 show that the heat transfer enhancement in the second dimple region is always higher than in the first dimple. In the Reynolds number range from $\mathrm{Re_d} = 1 \times 10^4 - 3.5 \times 10^4$, the area mean value of the second dimple is 14% higher than that of the first one.

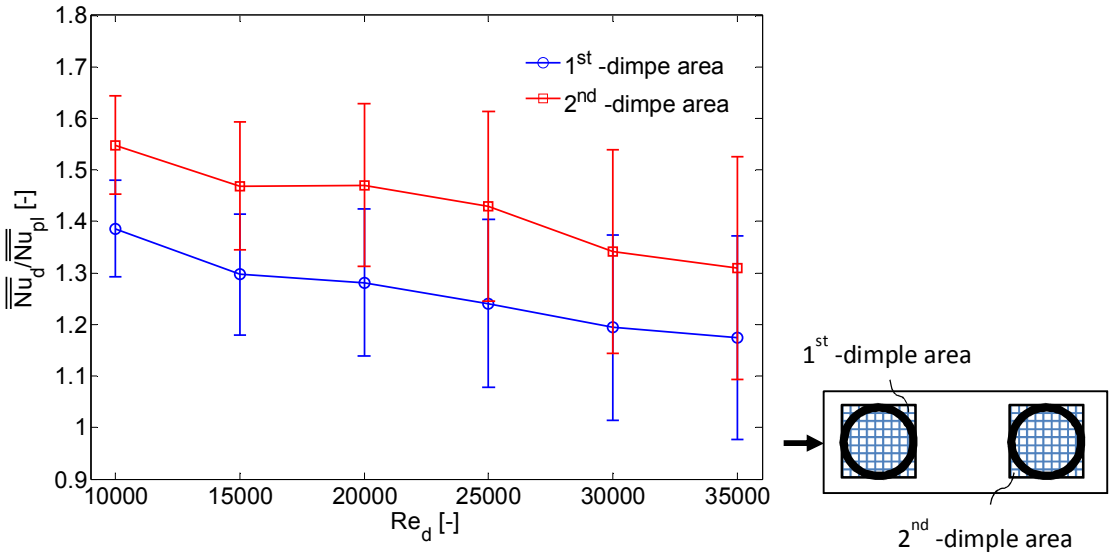

Fig. 5.21. Distributions of the mean Nusselt number ratio on different dimple areas of the double-dimpled surface.

5.3.2 Effect of Inlet Flow Temperature

Since in the convective heat transfer, Nusselt number not only depends on the Reynolds number but also on the Prandtl number, which is dependent on the flow temperature, the heat transfer of the dimpled surface could be influenced by changing the inlet flow temperature. However, the results show that the influence of this temperature is quite limited in this study. As shown in Fig. 5.22, the mean Nusselt number distribution of a single-dimpled surface is displayed against different inlet flow temperatures. Within a temperature range from 25 ℃ to 43 ℃, the mean Nusselt number on the dimpled surface decreases from 112 to 86. Thus, in this range, the variation to the mean value of the mean Nusselt number is within $\pm$14%. Furthermore, a distribution of mean Nusselt numbers on the reference surface is shown for comparison with the dimpled surface. On this surface, the mean Nusselt number drops from 92 to 80 with a variation of $\pm$8%. In this case, the influence of the inlet flow temperature is not significant. And the deviation is primarily due to the uncertainty of the measurement as well as the deviation of the Reynolds number in different flow temperatures.

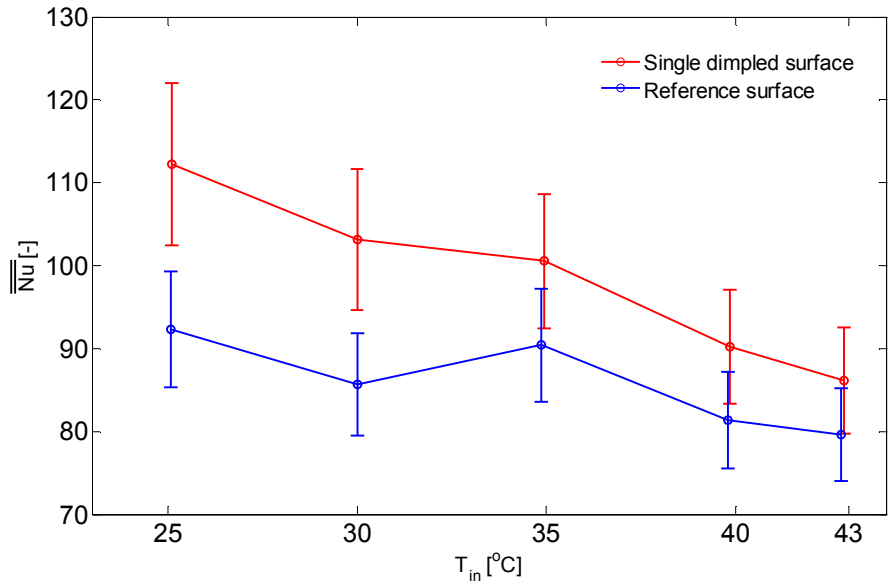

Fig. 5.22: Effect of inlet flow temperature on the mean Nusselt numbers of different heat surfaces ($\dot{q} = 32$ kW/m^2 and $\mathrm{Re_d} = 2 \times 10^4$).

5.3.3 Effect of Heat Flux

The heat flux has no effect on the heat transfer. However, it does influence the accuracy of the measurement. Once a higher heat flux is applied on the heating surface, under the same Reynolds number and inlet flow temperature, wall temperature difference is higher than in the lower heat flux case. Thus, the temperature measurement uncertainty has less influence on determining the Nusselt number. As shown in Fig. 5.23, the distributions of the area-mean Nusselt numbers on different heating surfaces are displayed against the heat fluxes. In the investigated heat flux range ($\dot{q} = 18 - 53$ kW/m^2), the mean Nusselt number on the dimpled surface varies between 101 and 95 with a deviation of $\pm 3\%$ to the mean value. On the reference surface, the mean Nusselt number from same region decreases from 100 to 85 in $\pm 9\%$. In this case, for each heating surface, the effect of the heat flux variation shows little influence on the heat transfer. However, at the heat flux $\dot{q} = 18$ kW/m^2, the mean Nusselt number on the dimpled surface is lower than that on the reference surface. Considering that the heat transfer on the dimpled surface is higher than on the plane surface, this distribution is incorrect because of the larger uncertainty of the Nusselt number at this heat flux. In higher heat fluxes, the Nusselt number of the dimpled surface is $8 - 12\%$ higher than on the reference surface. Additionally, since the uncertainty of Nusselt number is the smallest at the highest heat flux, the Nusselt number, which is more accurate, is a little bit lower than at moderate heat flux.

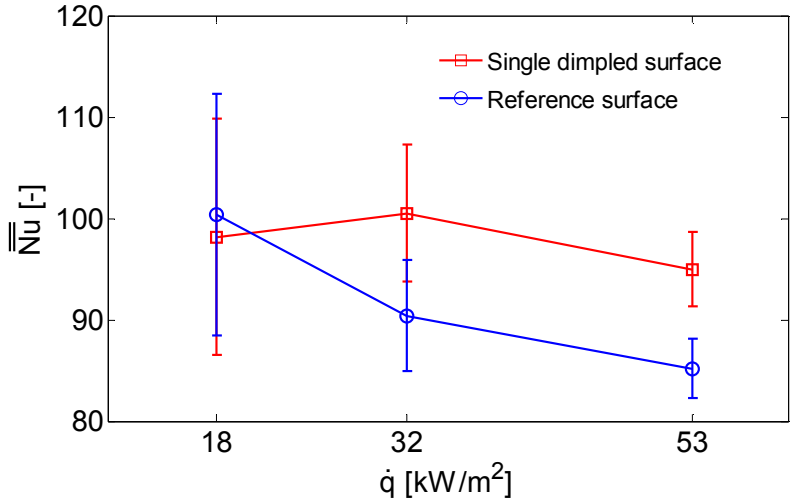

Fig. 5.23: Effect of heat flux on area-mean Nusselt number distributions on different heating surfaces ($T_{in} = 35\ ^{\circ}C$ and $Re_d = 2 \times 10^4$).

Furthermore, the inhomogeneous heat flux due to the dimple geometry is not influenced by the heat flux variation. The comparisons between the streamwise Nusselt number distributions at the moderate and highest heat fluxes (Fig. 5.24) show that the difference is only because of the measurement uncertainty, which varies regarding the local heat transfer coefficient. In this case, in a lower heat transfer region, for instance the plane surface upstream of the dimple, the difference of Nusselt number is quite small. In the higher heat transfer region, for instance in the reattachment zone, this difference is enlarged. In other words, at different heat fluxes, the distributions of inhomogeneous heat flux inside the dimple are almost the same and are only related to the dimple geometry.

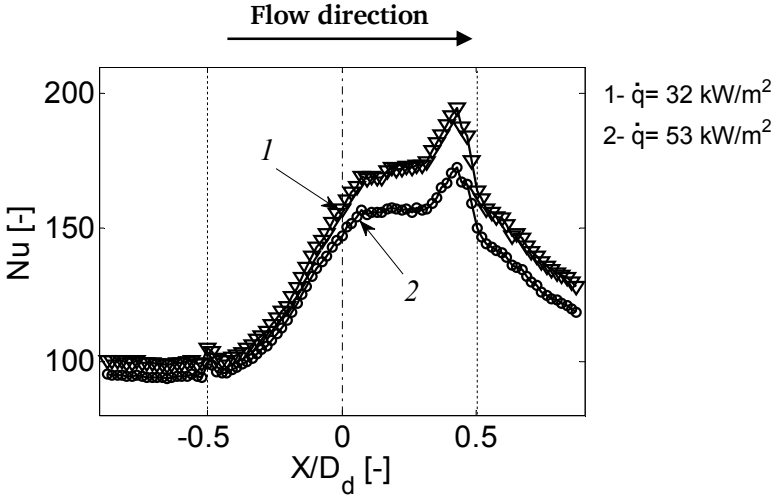

Fig. 5.24: Effect of the heat flux on the streamwise Nusselt number distributions on the centerline of the single-dimpled surface.

5.4.1 Instability of the Dimple Flow

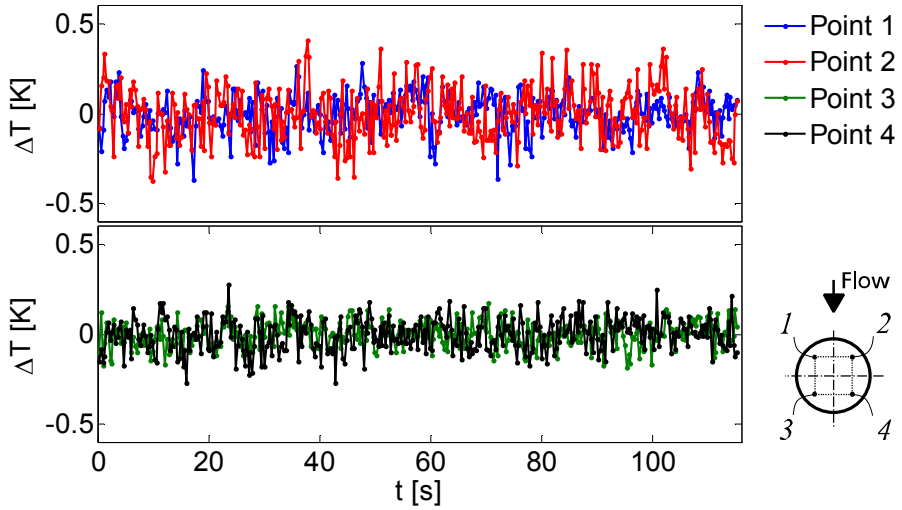

(a) $\mathrm{Re_d} = 1 \times 10^4$

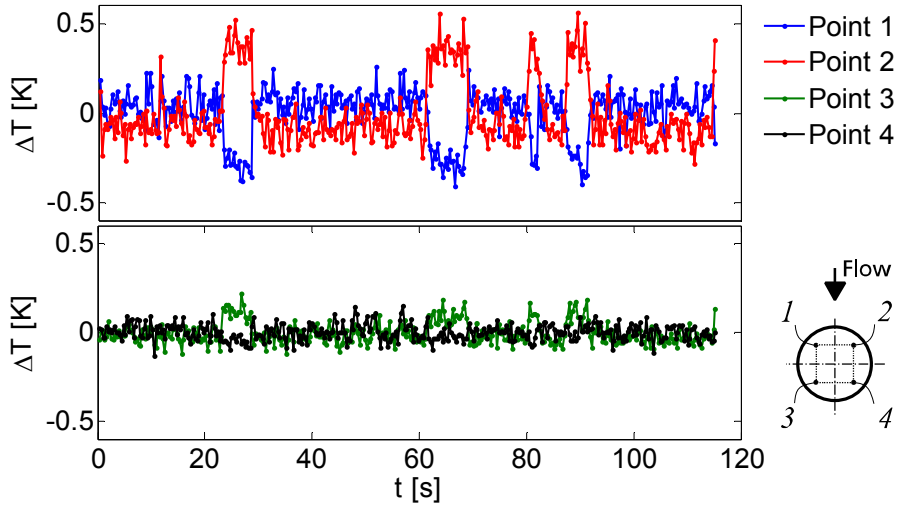

(b) $\mathrm{Re_d} = 2 \times 10^4$

Fig. 5.25: Fluctuations of local wall temperatures on four points in the dimple region.

Since the wall temperature is related to the flow structures above the dimpled surface, its fluctuations can be consider as the indicator of the instability in the flow. In Fig. 5.25, the fluctuations of the wall temperatures recorded at four points in the dimple region are plotted over time at two Reynolds numbers. These points are symmetrically distributed onto the streamwise and spanwise center planes of the dimple, at equal distances ($D_\mathrm{d}/4$) to the planes. The temperature of the points was measured by averaging over 0.32 s for each recording temperature value over a time interval of 115.2 s (see section 3.3.4).

Due to the temperatures at different points fluctuating at different levels, a temperature difference (Δt)

$$\Delta \mathrm{T}_{i,j} = \mathrm{T}_{i,j}(t) - \sum_{t} \mathrm{T}_{i,j}(t). \tag{5.7}$$

was calculated to compare the temperature fluctuations on the same basis. The distributions at a lower Reynolds number ($\mathrm{Re_d} = 1 \times 10^4$), as shown in Fig. 5.25(a), present a similar type of fluctuation in four positions. The fluctuations of the points in the rear half of the dimple (points 3 and 4) are relatively smaller than those situated in the front half (points 1 and 2) with a range of ± 0.4 K. As the Reynolds number increased to $\mathrm{Re_d} = 2 \times 10^4$, a typical alternation between two temperature levels was observed (Fig. 5.25(b)). At point 1, the temperature fluctuation keeps close to the zero level, and at $t = 23\ s$, it suddenly drops to another temperature level, around 0.3 K below. After about 6 s, the temperature switches again from the lower back to the zero level. This process is repeated four times during the whole interval, while the period length of each switching circle varied between 2 s to 8 s. On the other side, the same alternation is found at point 2, which is synchronizing with the fluctuation in point 1. However, the alternative temperature level is just opposite to position 1 and has a deviation of around 0.4 K above zero. In the rear side of the dimpled, similar temperature distributions were observed at points 3 and 4. However, the magnitude of the alternation is much smaller. To be noticed that the temperature patterns in the dimple's rear surface are just opposite to these in the front surface. For example, at same time ($t = 25.6\ s$), fluctuations at point 2 and 3 are both positive and the fluctuations at other two pints are lower. It is probable that the high frequency oscillation flow and the switching mode occurred inside the dimple and caused these fluctuations, as reported by Terekhov et al. [92]. For one thing, it is similar to the report that the switching region takes place at higher Reynolds numbers, while in the low Reynolds numbers there is only high-frequency oscillation flow in the dimple. For another, the distribution of temperature fluctuations in the front area at high Reynolds numbers indicates the alternation of the asymmetric vortex. Since the flow is asymmetric, the epicenters of the circulations became unequal in size and caused the local temperature maximums in the recirculation zone to vary from left to right. In this case, the temperature was alternating between two temperature levels at each side. The details of the heat transfer influenced by these flow regimes will be discussed in the following sections.

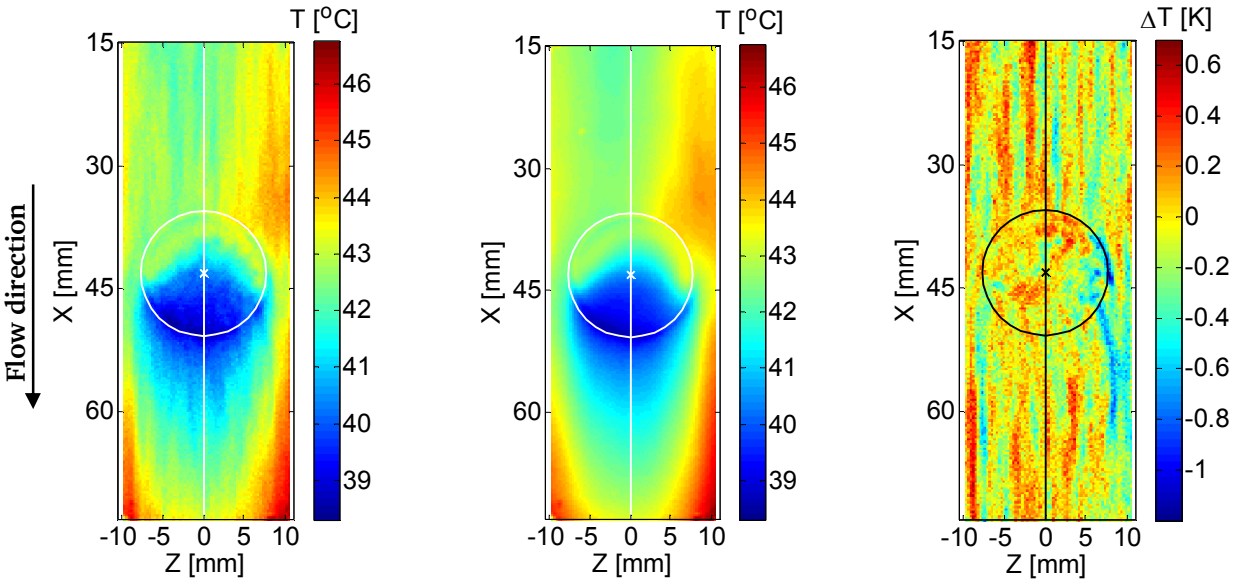

Fig. 5.26: Comparison of the wall temperature distribution at $\mathrm{Re_d} = 1 \times 10^4$ to a time-averaged distribution: (a) wall temperature distribution T_{tran} recorded in $20\,ms$, (b) averaged temperature distribution T_{avg} accumulated in 115.2 s, (c) the differences between the two distributions, $\Delta T = T_{tran.} - T_{avg.}$.

The two-dimensional temperature distribution (recorded at 50 Hz) at $\mathrm{Re_d} = 1 \times 10^4$ shown in Fig. 5.26(a) is quite similar to the time-averaged distribution accumulated over a sufficient long interval (averaged over 115.2 s, Fig. 5.26(b)). This suggests that the 'snap shot' of flow pattern in a quite small time interval is comparable to that revealed by the averaged distribution over long time. Due to the impulse of the turbulent flow in the boundary layer, temperature zones in the distribution recorded in short time are coarser than in the time-averaged distribution. On the plane surface upstream and downstream of the dimple, many belt-shaped temperature areas are located along the flow direction in the transient case. It is probably that on the flat wall the local wall temperature was influenced by the longitudinal vortex in the turbulent boundary layer, causing a higher temperature on the wall at the detached side and a lower temperature at the reattached side. These longitudinal flow structures were fluctuating over time in a small range, thus is not observed in the averaged distribution. A comparison of the two cases is presented in Fig. 5.26(c), which is a distribution of temperature differences between a 'snap shot' and averaged distribution. Since the averaged distribution is considered as a steady case of the wall temperature on the dimpled surface, the temperature difference distribution indicates the deviations of the transient wall temperature at this time. The maximum temperature deviation due to the longitudinal vortex structures is around −0.2 K– 0.6 K. In most areas inside the dimple,

the transient temperature is higher than the averaged case. It is likely that at this moment, either the flows with relatively higher temperature were brought into the dimple structure or worse heat transfer took place inside the dimple and caused the local temperature to rise. The narrow low-temperature zone found near the dimple's edge on the left has a deviation of up to 1.2 K. It is probably caused by the small transverse vibrations of the recirculation zone. Furthermore, this low temperature zone may affect the flows in the wake and causes a subsequent low temperature region downstream in the wake.

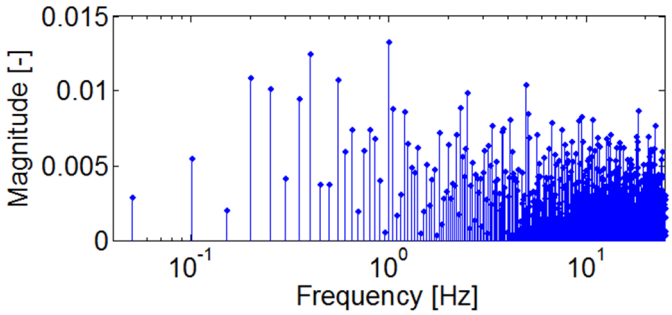

Fig. 5.27. Frequency spectrum of the temperature signal at point 1 for $\mathrm{Re_d} = 1 \times 10^4$.

The observation in the experiment shows that the flow in the dimple is asymmetric, which closely matches the pattern described in the studies [30]. In the investigated time interval, the formation of the reattachment zone is almost stable. However, the temperature distribution in the recirculation zone is more dynamic and is similar to the profiles of local heat transfer distributions predicted by Isaev et al. [30]. The frequency spectrum shown in Fig. 5.27 reveals the frequency range of the temperature fluctuation at the point 1. The frequency, which has a higher magnitude by comparison, is in a range of 0.2—5 Hz. This result is different from the character frequency of $f > 1$ Hz, as reported by Terekhov et al [91]. It is probable that the response of the wall temperature signal is delayed considerably longer than the fluctuation of the flow structure.

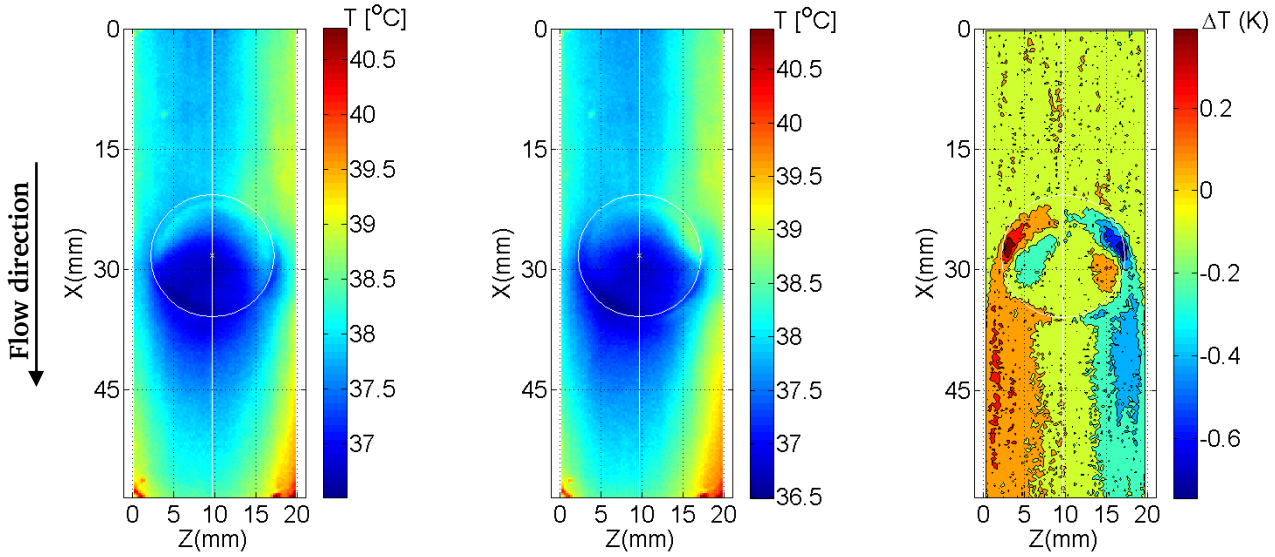

(a) T_{23s} (b) T_{49s} (c) $\Delta T = T_{23s} - T_{49s}$

Fig. 5.28: Temperature distributions in the switching mode: (a) temperature distribution at $t = 23$ s, (b) temperature distribution at $t = 49$ s, (c) temperature difference between the two distributions ($\Delta T = T_{23s} - T_{49s}$).

The wall temperature distributions in the switching mode are displayed in Fig. 5.28. The temperature distributions at the times $t = 23$ s and 49 s are shown in Fig. 5.28(a) and (b) with respect to the different temperature levels presented by local temperature fluctuations in the same process in Fig. 5.25(b). At the time $t = 23$ s, the high temperature region in the recirculation zone is almost symmetric. The distribution in the reattachment zone is asymmetric with the low temperature regions that cover most of the rear dimple's edge on the left. Besides, the distribution in the wake is nearly symmetric to the streamwise center. In the distribution at another temperature level ($t = 49$ s), the distribution in the reattachment zone is nearly unchanged, while the symmetric distributions in the recirculation zone and the dimple wake are observed. In the recirculation zone, the high temperature region primarily remains at the right side, while in the wake, the pattern is closer to the left. In order to compare the distributions for these two cases, a temperature difference distribution, which is determined by subtracting the temperature distribution of the second case from the first, is shown in Fig. 5.28(c). In the distribution, the area with a moderate value, here close to zero, indicates that there is no significant difference in switching. This applies to the plane area upstream of the dimple and in the symmetric regions inside the dimple as well as in the wake. Furthermore, the area with extreme values shows changes within the alternation, mostly distributed in the recirculation zone located in the middle of the dimple and the sides of the wake.

It is possible that this type of temperature distribution is caused by the continuous switching of the tornado-like vortex in the dimple. According to the flow structures reported by Terekhov et al. [90], two symmetric streams are generated in the middle part of the dimple and ejected outside the dimple across the dimple's edges on opposite sides. These streams cause the symmetrically distributed regions on each side of the wake. This effect is also present in the simulation result of the Nusselt distribution [42]. It is quite probable that the distribution of the different temperature zones is due to the periodic alternation of these outgoing streams. Due to the flow detaching at the epicenter of the dimple, the stagnant fluid at this location always creates a low heat transfer region and therefore raises the local temperature. When the stream travels in the dimpled, no influence was discovered in the distribution, because it is above the wall. Then, at the dimple's edge on the opposite side, this flow meets the raised dimple surface and reacts with the local flows. It creates another low heat transfer region with higher wall temperature. After that, the stream leaves the dimple's edge behind and influences the wall temperature in the wake. The distribution of the negative values indicates that the same stream effect happens again in the other switching state with the same process. This periodic alternation of the local temperature in the dimple's wake is also seen by the experimental observation [18].

In Fig. 5.29, the Nusselt number on the dimpled surface is presented with different recording times. The one shown in Fig. 5.29(a) is the Nusselt distribution recorded in a moment (in 20 ms), while Fig. 5.29(b) shows the averaged Nusselt number over 10 s. Furthermore, the comparison of the instantaneous distribution with the steady counterpart shows their difference in Fig. 5.29(c). In the first distribution, the iso-lines are much rougher than those in the averaged distribution, indicating that the local fluctuations were seen at the smaller time scales. The distribution of the difference values indicates that the heat transfer region with enhancement and reduction are both present in the dimple regions and in the wake at this moment. Similar to case in the temperature difference distributions, the differences of the instantaneous Nusselt number to the averaged case shows the influence of the switching mode in one state. In this distribution, the outgoing flow generated on the left side leaves the dimple on the right side, causing the low Nusselt number in the region. In the wake, the influence is not restricted to the side but also distributed close to the streamwise center. However, the influence in the centerline is present early, probably due to the strong turbulence at that location, where fluids from the dimple were mixed with main flow. On the other hand, the enhancement region is most likely created by some of the inlet flows attaching on the rear-right side of the dimple and mixing with the flows on the left side near the dimple' edge and in the wake after that. The maximum different of Nusselt number on the surface is nearly 50.

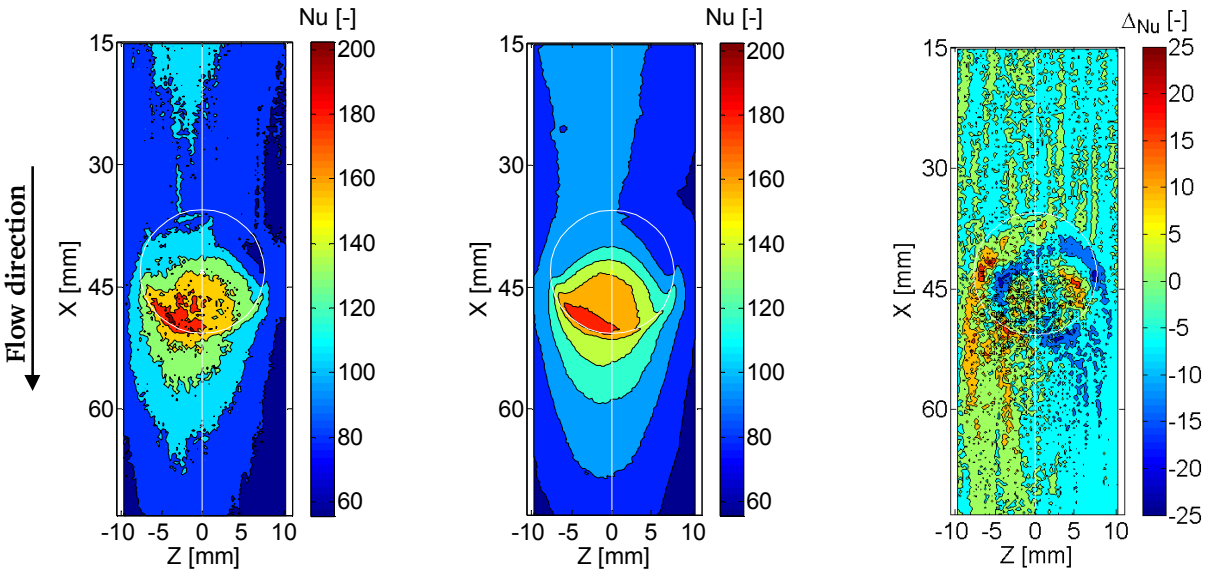

(a) Nu_{tran} (b) Nu_{avg} (c) $\Delta Nu=Nu_{tran}-Nu_{avg}$

Fig. 5.29: Comparison of Nusselt number distribution to an averaged result: (a) Nusselt number distribution recorded in a moment Nu_{tran}, (b) averaged Nusselt number distribution Nu_{avg} over $10s$, (c) distribution of the Nusselt number differences ($\Delta Nu=Nu_{tran}-Nu_{avg}$).

Finally, according to the experimental observation, the fluctuations of the wall temperature do not have a large influence on heat transfer. For one thing, the fluctuations are quite regular over time and whole dimpled surface, and therefore can be minimized by averaging over a sufficient long time period, for example 10 s. For another, in the transient distributions, flow oscillations, especially in the switching mode, influence the heat transfer at different locations. However, since the enhancement and weakness regions occur together and cover comparable areas, the influence on the area-mean values of the heat transfer on the surface is quite limited. Thus, since there is a ± 25 difference in the Nusselt number distribution, the area-mean Nusselt number and correlations are less strongly affected.

Chapter 6

Summary and Outlook

IR thermography studies at high spatial and temporal resolutions were performed to investigate the convective heat transfer enhancement created by dimple structures on a plane surface. The dimple structure, with a printing diameter of $D_\mathrm{d} = 15.3$ mm and a relative depth of $t/D_\mathrm{d} = 0.26$, was placed on the bottom wall of a rectangular channel with a relative channel height of $h/D_\mathrm{d} = 0.3$. The measurements were performed in water flow with a Reynolds number range of $\mathrm{Re_d} = 1 \times 10^4 - 3.5 \times 10^4$ and an inlet flow temperature ranged from $T_\mathrm{in} = 25 - 43$ ℃. Three surfaces, plane surface, single-dimpled surface, and double-dimpled surface, were investigated in this study. During the heating experiment, the resistance coatings on these surfaces charged by DC power produced a heat flux of $\dot{q} = 18 - 53$ kW/m^2 by Joule heating. Thermal images including time-averaged images and sequences were then recorded by IR camera and later translated into the temperature distribution via calibration matrixes determined in the in-situ calibrations. The Nusselt number was finally calculated from the measured wall temperature for evaluating the heat transfer on the surfaces.

Three zones were identified on the dimpled wall, which are comparable to previous studies. The recirculation zone was a banana-shaped area located just downstream of the front edge of the dimple. Most likely, a tornado-like vortex with poor heat transfer characteristics spread across this region. The reattachment zone was a low temperature area found within the rear half of the dimple. It was probably generated by the reattachment of the separated flow, causing a significant degree of mixing in the region. Moreover, the local maximum of the heat transfer was

observed quite close to the dimple's rear edge. The wake, i.e. the lower temperature region downstream of the reattaching zone, was created by the strong turbulence at the dimple's rear edge. The Nusselt number distribution at $Re_d = 2 \times 10^4$ showed that the highest heat transfer region was located in the reattachment zone close to the rear edge with a local maximum Nusselt number about two times higher than that on the plane surface in the identical situation. A lower heat transfer region with a heat transfer rate $Nu_d/Nu_{pl} \approx 1$ was found in the recirculation zone near the dimple's front edge. In the wake, Nusselt number dropped from the maximum value in the reattachment zone to that on the plane surface.

By increasing the Reynolds number in the channel flow, the Nusselt number on the dimpled surfaces increased accordingly. However, compared to the heat transfer on the plane surface, the Nusselt number ratio decreased with increasing Reynolds numbers. For example, the local maximum of heat transfer rates on the single-dimpled surface at the lowest Reynolds number ($Re_d = 10000$) was $Nu_d/Nu_{pl} \approx 2.4$ and became around $Nu_d/Nu_{pl} \approx 1.7$ at the highest Reynolds number $Re_d = 35000$. This indicates that the mixing effect in the boundary layer induced by the dimple structure could no longer be as significant as the turbulence mixing on the plane surface at higher Reynolds number. In the wake, influenced by the rising Reynolds number, the length of the wake shrank in the streamwise direction. Furthermore, on the double-dimpled surface, the difference between the local maximum Nusselt number ratios became smaller with the rising Reynolds numbers. This suggests that the influence of the upstream dimple was dependent on the Reynolds number. Other effects, such as the inlet flow temperature and heat flux, had less influence on heat transfer. Because of the larger temperature difference generated between the wall and inlet flow, the uncertainty of the Nusselt number at a higher heat flux was smaller.

Wall temperature fluctuation influenced by instability of the flows on the dimpled surface was observed in this study. The switching mode of the wall temperature with a variable period between 2 s and 8 s was observed at Reynolds numbers higher than $Re_d = 1 \times 10^4$. It is quite possible that this low frequency temperature fluctuation was caused by switching vortex flows in the dimple structure. When comparing the temperature distribution in one state of the switching mode to that in another state, four characteristic symmetric regions could be identified in the dimpled region, indicating the possible position of the vortex structure inside the dimpled region. Furthermore, in the wake, two asymmetric temperature regions were discovered near the dimple's rear edge. This may have been caused by the periodic jet flows, generated in the dimple and periodically ejected downstream. Finally, the influence of the switching mode on the local heat transfer was observed with a fluctuation of $\pm 30\% - \pm 50\%$. However, since the fluctuating

regions were nearly symmetric and appeared periodically over time, this fluctuation had less influence on the averaged Nusselt number of dimpled surfaces.

In the future, further research studies could be based on three questions. The first question is what will happen in broader ranges of experimental parameters, such as higher Reynolds numbers, higher heat fluxes, and lower flow temperature. In the current study, the maximum Reynolds number $\mathrm{Re_d} = 3.5 \times 10^4$ is still some distance away from $\mathrm{Re_d} = 2 \times 10^5$ in previous studies. Furthermore, it is necessary to investigate the special dimples, such as asymmetric dimples and round dimples with a hill inside, and dimple arrays, predicted by many numerical simulations.

The second question, how is the temperature distributed in the flows above the dimpled surface? This helps to know the temperature gradient in the flows, indicating the local entropy generation in the flow and leading to an innovative method for developing dimple structure. So far, it is possible in the lab to use the laser-induced fluorescence (LIF) method to measure the temperature field in the flow. However, since the measurement is conducted by observing perpendicularly the fluorescence of the flow to the inducing laser sheet to achieve a suitable focus, it is quite difficult to conduct the measurement inside the dimple, which has a concave geometry. A further difficulty is due to the current heating surface being opaque in the spectrum of the inducing laser beam. Thus, extra heat flow from the inducing laser could generate on the heating surface during the experiment and could influence the temperature measurement. In this case, new technologies need to be developed to implement LIF measurement in the structure. For one thing, a new camera lens according to the Scheimpflug principle, which enables the observation of the laser sheet at an angle to its normal axis, can be adopted for angled observation in the dimple structure. For another, the development of a new heating layer, which is coated on the smooth surface and at the same time transparent in the spectrum range of the inducing laser, might allow the influence of the laser beam to be eliminated.

Finally, new methods for improving current heating technology would be welcome. In the current study, multi-layer coated glass was used as the heating element in the water flow. In order to increase the emission rate of the thin film-glass interface, the glass surface was roughened before the coating. In this case, SiO_2 could not cover the ITO layer properly, thus causing the decaying of ITO layer during heating in the water flow. Nevertheless, the large thermal conductivity of the substrate causes a strong tangential conduction in the glass body and could have strong influences on the wall temperature distribution. In the future, the glass heater can be improved by using a smooth heating layer, such as the chromium/black chromium coating. In this case, the protection of the SiO_2 layer can be guaranteed. On the other hand,

dielectric liquid, such as silicon oil with a viscosity similar to water, can be used as the working fluid, thus avoiding any reaction with the ITO layer during heating (see appendix). However, this type of silicon oil has a much lower flash point, which is quite dangerous when large amount of the oil (~20 L) is employed in the experiment.

Appendix

Observation of heat transfer on dimpled surfaces in silicon oil flow

In order to prevent hydrolysis of ITO layer in the water flow as discussed in section 4.2.1, a test for heating up the surface in silicon oil flow[23] was considered. This test was conducted by adopting the same experimental setup used in the water experiments. A double-dimpled surface was used as the heating surface in the experiment. As a result, the wall temperature distributions measured from two situations, in which only the cathode and anode of the DC power were inversed, was compared.

Silicon oil and experimental parameters

Table. A: Physical properties of silicon oil.

Property (13 ℃)	value
Density (kg/m^3)	0.92×10^3
Viscosity (m^2/s)	5.1×10^{-6} m^2/s
Thermal conductivity (W/(m·K))	0.1155
Pr (-)	58

The silicon oil adopted in this test has the properties listed in Table A. Due to the viscosity of the oil being nearly five times greater than water, a Reynolds number $Re_h = 1600$ in the oil flow had already reached the maximum pressure in the channel comparable to the water experiment. Because of the lower thermal capacity and thermal conductivity of the oil, the temperature

[23] MB-Elbesilöle B (5×10^{-6} m^2/s at 20 ℃), L. Böwing GmbH, Hofheim a. Ts./Germany

difference between the wall temperature and the inlet flow temperature was considerably high. In this case, the inlet temperature and the heat flow (T_{in} = 13 ℃ and $\dot{Q}$ = 46 W) were set much lower than those in the water experiment to keep the measured wall temperature in the calibration range of the IR camera.

Result

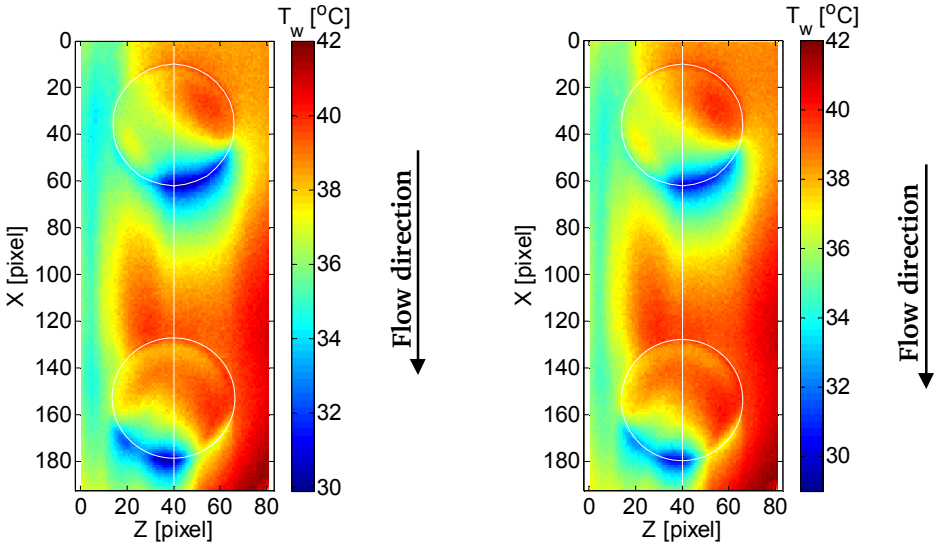

(a) cathode on left side (A side) (b) cathode on right side (B side)

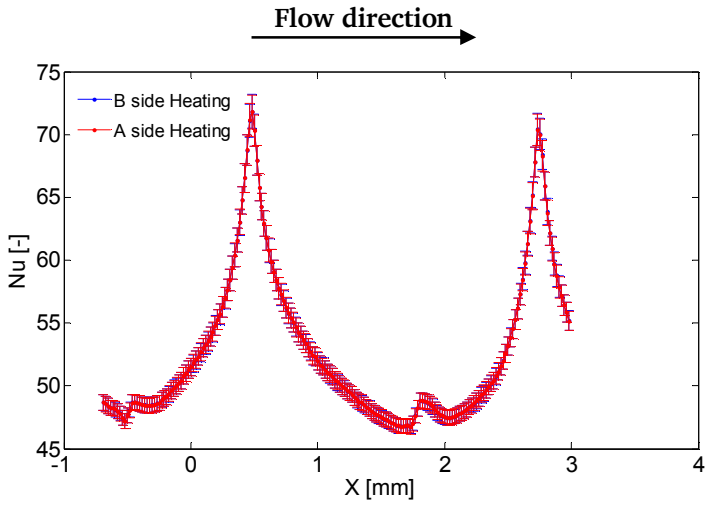

(c)

Fig. A.1. Wall temperature distributions on double-dimpled surface (T_{in} = 13 ℃, $\dot{Q}$ = 46 W, and Re_h = 1600).

As shown in the temperature distributions in Fig. A.1(a) and Fig. A.1(b), the wall temperature distribution was independent from the side of the cathode. Compared with the distributions in

the center plane of two cases (Fig. A.1(c)), these also indicate that the local wall temperature was not influenced by alternating the electrodes' sides. As a result, the asymmetric heating could only occur during heating in the water, with hydrolysis damaging the ITO coating. It should be noticed that the wall temperature distributions in both cases are not symmetric to the center plane. The investigation shows that the lower temperature region on the left side was caused by the inhomogeneous flows from upstream, formed by the sealing glue expanding in the silicon oil flow during the experiment and thus causing a disturbance in the channel flow.

Bibliography

[1] Verein Deutscher Ingenieure (VDI)-Gesellschaft Verfarenstechnik und Chemieingenieurwesen (GVC), VDI-Wärmeatlas, Springer Verlag, 2006.

[2] A. E. Bergles, Techniques to Enhance Heat Transfer, in: W. M. Rohsenow, J. P. Hartnett, Y. I. Cho (Eds.) Handbook of Heat Transfer, 3rd ed., McGraw-Hill, New York, 1998.

[3] V.N. Afanasyev, Y.P. Chudnovsky, A.I. Leontiev, P.S. Roganov, Turbulent flow friction and heat transfer characteristics for spherical cavities on a flat plate, Experimental Thermal and Fluid Science, 7(1) (1993) 1-8.

[4] V.N. Afanasyev, P.S. Roganov, Y.P. Chudnovskii, Heat transfer processes in a turbulent flow along regular reliefs of spherical concavities, Journal of Engineering Physics and Thermophysics, 63(1) (1992) 668-672.

[5] E. Allen, S. Triantaphillidou, The Manual of Photography, Elsevier Science & Technology Books, 2011.

[6] R.C. Arora, Refrigeration and Air Conditioning, PHI Learning, 2010.

[7] H. Bach, D. Krause, Thin Films on Glass, Springer, 1997.

[8] H.D. Baehr, K. Stephan, Heat and Mass Transfer, Springer Berlin Heidelberg, 2011.

[9] R.S. Bunker, K.F. Donnellan, Heat Transfer and Friction Factors for Flows Inside Circular Tubes With Concavity Surfaces, Journal of Turbomachinery, 125(4) (2003) 665.

[10] N.K. Burgess, P.M. Ligrani, Effects Of Dimple Depth on Channel Nusselt Numbers and Friction Factors, Journal of Heat Transfer, 127(8) (2005) 839.

[11] N.K. Burgess, M.M. Oliveira, P.M. Ligrani Nusselt Number Behavior on Deep Dimpled Surfaces Within a Channel, Journal of Heat Transfer, 125(1) (2003) 11.

[12] S.W. Chang, K.F. Chiang, T.L. Yang, C.C. Huang, Heat transfer and pressure drop in dimpled fin channels, Experimental Thermal and Fluid Science, 33(1) (2008) 23-40.

[13] R.C. Chu, R.E. Simons, M.J. Ellsworth, R.R. Schmidt, V. Cozzolino, Review of Cooling Technologies for Computer Products, IEEE Transactions on Device and Materials Reliability, 4(4) (2004) 568-585.

[14] J.M. Délery, Robert Legendre and Henri Werlé: Toward the Elucidation of Three-Dimensional Separation, Annual Review of Fluid Mechanics, 33(1) (2001) 129-154.

[15] J.H. Doo, H.S. Yoon, M.Y. Ha, Study on improvement of compactness of a plate heat exchanger using a newly designed primary surface, International Journal of Heat and Mass Transfer, 53(25-26) (2010) 5733-5746.

[16] M.A. Elyyan, A. Rozati, D.K. Tafti, Investigation of dimpled fins for heat transfer enhancement in compact heat exchangers, International Journal of Heat and Mass Transfer, 51(11-12) (2008) 2950-2966.

[17] M.A. Elyyan, D.K. Tafti, LES Investigation of Flow and Heat Transfer in a Channel With Dimples and Protrusions, in, 2007, pp. 609-621.

[18] A.B. Ezerskii, V.G. Shekhov, Visualization of the Heat flux in flow over isolated spherical depressions, Izvestiya Akademii Nauk SSSR, Mekhanika Zhidkosti i Gaza (Translated), No. 6 (1989) p. 161-164.

[19] T.E. Faber, Fluid Dynamics for Physicists (fourth edition), 4th ed., Cambridge University Press, 2004.

[20] A. Ferber, M. Hofer, M. Krämer, T. Warmuth, Begleitende numerische Simulationen zur experimentellen Untersuchung der konvektiven Wärmeübertragung an Dellenoberflächen, Advanced Design Project of Technischen Universität Darmstadt, Division: Technical Thermodynamicss, 2009.

[21] K. Füchsel, U. Schulz, N. Kaiser, A. Tünnermann, Low temperature deposition of indium tin oxide films by plasma ion-assisted evaporation, Applied Optics, 47(13) (2008) C297.

[22] C. Gerardi, J. Buongiorno, L.W. Hu, T. McKrell, Study of bubble growth in water pool boiling through synchronized, infrared thermometry and high-speed video, International Journal of Heat and Mass Transfer, 53(19-20) (2010) 4185-4192.

[23] S. Groß, M. Soemers, A. Mhamdi, F.A. Sibai, A. Reusken, W. Marquardt, U. Renz, Identification of boundary heat fluxes in a falling film experiment using high resolution temperature measurements, International Journal of Heat and Mass Transfer, 48(25-26) (2005) 5549-5562.

[24] J.-C. Han, S. Dutta, S. Ekkad, Gas Turbine Heat Transfer and Cooling Technology, Taylor & Francis Inc., 2012.

[25] C.R. Hedlund, P.M. Ligrani, B. Glezer, H.K. Moon, Heat transfer in a swirl chamber at different temperature ratios and Reynolds numbers, International Journal of Heat and Mass Transfer, 42(22) (1999) 4081-4091.

[26] M. Hiwada, I. Mabuchi, M. Kumada, T. Kawamura, Some characteristics of flow pattern and heat transfer past a circular cylindrical cavity, JSME, Bulletin 26 (1983) p. 1744-1752.

[27] S.A. Isaev, The Effect of Rearrangement of the Vortex Structure on Heat Transfer under Conditions of Increasing Depth of a Spherical Dimple on the Wall of a Narrow Channel, High Temperature, 41(2) (2003) 229-232.

[28] S.A. Isaev, P.A. Baranov, N.A. Kudryavtsev, A.E. Usachov, Analysis of vortex heat transfer in a transverse flow past a trench on a plane using multiblock computation technologies and different semi-empirical models of turbulence, Journal of Engineering Physics and Thermophysics, 77(6) (2004) 1236-1246.

[29] S.A. Isaev, V.B. Kharchenko, Y.P. Chudnovskii, Calculation of a three-dimensional flow of a viscous incompressible liquid in the neighborhood of a shallow well on a flat surface, Journal of Engineering Physics and Thermophysics, 67(5-6) (1995) 1013-1017.

[30] S.A. Isaev, N.V. Kornev, A.I. Leontiev, E. Hassel, Influence of the Reynolds number and the spherical dimple depth on turbulent heat transfer and hydraulic loss in a narrow channel, International Journal of Heat and Mass Transfer, 53(1-3) (2010) 178-197.

[31] S.A. Isaev, A.I. Leontiev, Numerical Simulation of Vortex Enhancement of Heat Transfer under Conditions of Turbulent Flow Past a Spherical Dimple on the Wall of a Narrow Channel, High Temperature, 41(5) (2003) 665-679.

[32] S.A. Isaev, A.I. Leontiev, P.A. Baranov, Identification of self-organized vortexlike structures in numerically simulated turbulent flow of a viscous incompressible liquid streaming around a well on a plane, Technical Physics Letters, 26(1) (2000) 15-18.

[33] S.A. Isaev, A.I. Leontiev, P.A. Baranov, K.T. Metov, A.E. Usachov, Numerical Analysis of the Effect of Viscosity on the Vortex Dynamics in Laminar Separated Flow Past a Dimple on a Plane with Allowance for Its Asymmetry, Journal of Engineering Physics and Thermophysics, 74(2) (2001) 339-346.

[34] S.A. Isaev, A.I. Leontiev, P.A. Baranov, I.A. Pyshnyi, Numerical Analysis of the Influence of the Depth of a Spherical Hole on a Plane Wall on Turbulent Heat Exchange, Journal of Engineering Physics and Thermophysics, 76(1) (2003) 61-69.

[35] S.A. Isaev, A.I. Leontiev, P.A. Baranov, I.A. Pyshnyi, A.E. Usachov, Numerical analysis of the vortex intensification of heat transfer in a channel with a set of deep spherical dimples on one of the walls, Doklady Physics, 47(10) (2002) 755-757.

[36] S.A. Isaev, A.I. Leontiev, P.A. Baranov, A.E. Usachev, Bifurcation of vortex turbulent flow and intensification of heat transfer in a hollow, Doklady Physics, 45(8) (2000) 389-391.

[37] S.A. Isaev, A.I. Leontiev, K.T. Metov, V.B. Kharchenko, Modeling of the Influence of Viscosity on the Tornado Heat Exchange in Turbulent Flow around a Small Hole on the Plane, Journal of Engineering Physics and Thermophysics, 75(4) (2002) 890-898.

[38] S.A. Isaev, A.I. Leontiev, A.E. Usachev, Numerical study of the eddy mechanism of enhancement of heat and mass transfer near a surface with a cavity, Journal of Engineering Physics and Thermophysics, 71(3) (1998) 481-487.

[39] S.A. Isaev, A.I. Leontiev, A.E. Usachev, D.P. Frolov, Identifying Self-Organizing Jet Vortices in Simulating Laminar Flow and Heat Transfer Near an Unsymmetrical Solitary Recess, Applied Energy: Russian Journal of Fuel, 37(2) (1999) p. 112-119.

[40] S.A. Isaev, A.I. Leontiev, V.L. Zhdanov, Simulation of Tornado- Like Heat Transfer at the Flow Passing a Relief with Dimples, in: Twelfth International Heat Transfer Conference, Grenoble, 2002, pp. pp. 735-738.

[41] S.A. Isaev, S.Z. Sapozhnikov, V.Y. Mityakov, A.V. Mityakov, S.A. Mozhaiskii, A.E. Usachov, Numerical analysis of the influence of the physical viscosity on the vortex heat transfer in laminar and turbulent flows around a heated plate with a shallow spherical hole, Journal of Engineering Physics and Thermophysics, 82(5) (2009) 847-859.

[42] J. Turnow, Flow Structures and Heat Transfer on Dimpled Surface, Dissertation, Division: Maschinenbau und Schiffstechnik, University of Rostock, Rostock, 2012.

[43] J. Turnow, Simulations of Heat Transfer on a Plane and Dimpled Surface at Two Reynolds Numbers (Personal Communication), University of Rostock, (2012).

[44] J. Turnow, N. Kornev, E. Hassel, Vortex structures, heat ransfer and surface optimization of dimpled surfaces, in: THMT-12. Proceedings of the Seventh International Symposium On Turbulence, Heat and Mass Transfer Palermo, Palermo, Italy, 2012, pp. 12.

[45] J. Turnow, N. Kornev, S. Isaev, E. Hassel, Vortex mechanism of heat transfer enhancement in a channel with spherical and oval dimples, Heat and Mass Transfer, 47(3) (2010) 301-313.

[46] J. Turnow, V. Zhdanov, E. Hassel, N. Kornev, Flow structures and heat transfer on dimpled surfaces, in: Seventh International Symposium on Turbulence and Shear Flow Phenomena (TSFP-7), Ottawa, 2011, pp. 6.

[47] S. Kakaç, R.K. Shah, W. Aung, Handbook of single-phase convective heat transfer, Wiley, 1987.

[48] K. Kanokjaruvijit, R.F. Martinez-Botas, Heat Transfer and Pressure Investigation of Dimple Impingement, Journal of Turbomachinery, 130(1) (2008) 011003.

[49] R. Karwa, B.K. Maheshwari, N. Karwa, Experimental study of heat transfer enhancement in an asymmetrically heated rectangular duct with perforated baffles, International Communications in Heat and Mass Transfer, 32(1-2) (2005) 275-284.

[50] R. Karwa, S.C. Solanki, J.S. Saini, Heat transfer coefficient and friction factor correlations for the transitional flow regime in rib-roughened rectangular ducts, International Journal of Heat and Mass Transfer, 42(9) (1999) 1597-1615.

[51] N. Kornev, E. Hassel, H. Herwig, S. Isaev, P. Stephan, V. Zhdanov, Erhöhung des Wärmeüberganges durch Wirbelinduktion in Oberflächendellen, Forschung im Ingenieurwesen, 69(2) (2004) 90-100.

[52] P.S. Kumar, K.S. Raju, P. Mahanta, A. Dewan, Review of passive heat transfer augmentation techniques, Proceedings of the Institution of Mechanical Engineers, Part A: Journal of Power and Energy, 218(7) (2004) 509-527.

[53] S.S. Kutateladze, E.P. Volchkov, V.I. Terekhov, Aerodynamics and Heat and Mass Exchange in Bounded Vortex Flows, Novosibirsk, Insititute of Thermophysics, Siberian Branch of Academy of Sciences USSR, (1987).

[54] P.M. Ligrani, J.L. Harrison, G.I. Mahmmod, M.L. Hill, Flow structure due to dimple depressions on a channel surface, Physics of Fluids, 13(11) (2001) 3442.

[55] P.M. Ligrani, M.M. Oliveira, T. Blaskovich, Comparison of Heat Transfer Augmentation Techniques, AIAA Journal, 41(3) (2003) 337-362.

[56] G.I. Mahmood, M.L. Hill, D.L. Nelson, P.M. Ligrani, H.K. Moon, B. Glezer, Local Heat Transfer and Flow Structure on and Above a Dimpled Surface in a Channel, Journal of Turbomachinery, 123(1) (2001) 115.

[57] G.I. Mahmood, P.M. Ligrani, Heat transfer in a dimpled channel: combined influences of aspect ratio, temperature ratio, Reynolds number, and flow structure, International Journal of Heat and Mass Transfer, 45(10) (2002) 2011-2020.

[58] R.M. Manglik, Heat Transfer Enhancement in: A. Bejan, A.D. Kraus (Eds.) Heat Transfer Handbook, John Wiley & Sons, Inc., 2003.

[59] R.M. Manglik, A.E. Bergles, Swirl flow heat transfer and pressure drop with twisted-tape inserts, 36 (2003) 183-266.

[60] F. Marcucci, P.di. Marco, W. Grassi, Technical Requirements of a Thin Gold Layer Sputted on Cleartran Substrate. Preliminary Study for the ARIEL Experiment on Fluidpac (Internal Document), University of Pisa, DE-LO 10/00 (2001) 8.

[61] R.D. Mehta, Sports Ball Aerodynamics, 506 (2008) 229-331.

[62] H.K. Moon, T. O'Connell, B. Glezer, Channel Height Effect on Heat Transfer and Friction in a Dimpled Passage, Journal of Engineering for Gas Turbines and Power, 122(2) (2000) 307.

[63] N. Schweizer, Multi-Scale investigation of nucleate boiling phenomena in microgravity, Dissertation, Division: Technical Thermodynamics, Technische Universität Darmstadt, Darmstadt, 2010.

[64] R. Nasarek, Temperature Field Measurements with High Spatial and Temporal Resolution Using Liquid Crystal Thermography and Laser Induced Fluorescence, Dissertation, Division: Technical Thermodynamics, Technischen Universität Darmstadt, Darmstadt, 2010.

[65] G. Nowak, W. Wróblewski, I. Nowak, Convective cooling optimization of a blade for a supercritical steam turbine, International Journal of Heat and Mass Transfer, 55(17-18) (2012) 4511-4520.

[66] K. Ochsner, Geothermal Heat Pumps: A Guide for Planning and Installing, Taylor & Francis, 2012.

[67] E. Oker, H.J. Merte, Semi-transparent gold film as simultaneous surface heater and resistance thermometer for nucleate boiling studies, Journal Name: J. Heat Transfer; (United States); Journal Volume: 103:1, (1981) Medium: X; Size: Pages: 65-68.

[68] C. Ozalp, A. Pinarbasi, B. Sahin, Experimental measurement of flow past cavities of different shapes, Experimental Thermal and Fluid Science, 34(5) (2010) 505-515.

[69] J. Park, P.M. Ligrani, Numerical Predictions of Heat Transfer and Fluid Flow Characteristics for Seven Different Dimpled Surfaces in a Channel, Numerical Heat Transfer, Part A: Applications, 47(3) (2005) 209-232.

[70] C.C. Pascual, S.M. Jeter, S.I. Abdel-Khalik, Visualization of boiling bubble dynamics using a flat uniformly heated transparent surface, International Journal of Heat and Mass Transfer, 45(3) (2002) 691-696.

[71] J. Petroski, Thermal Challenges In LED Cooling, Electronics Cooling (November) (2006).

[72] A.K. Pozarlik, D. Panara, J.B.W. Kok, T.H.M.v. der, Heat transfer in a recirculation zone at steady-state and oscillating conditions - the back facing step test case, in: 5th European Thermal-Sciences Conference, EUROTHERM 2008, TUE, Eindhoven, the Netherlands, 2008.

[73] K.H. Presser, Empirische Gleichungen zur Berechnung der Stoff- und Wärmeübertragung für den Spezialfall der abgerissenen Strömung, International Journal of Heat and Mass Transfer, 15(12) (1972) 2447-2471.

[74] S. Pulyaev, Experimentelle Untersuchung des Wärmeübergangs an einer Dellenstruktur, Studienarbeit, Division: Technical Thermodynamics, Technischen Universität Darmstadt, 2010.

[75] R. Schmidt, Challenges in Electronic Cooling—Opportunities for Enhanced Thermal Management Techniques—Microprocessor Liquid Cooled Minichannel Heat Sink, Heat Transfer Engineering, 25(3) (2004) 3-12.

[76] Y. Rao, Y. Xu, C. Wan, An experimental and numerical study of flow and heat transfer in channels with pin fin-dimple and pin fin arrays, Experimental Thermal and Fluid Science, 38 (2012) 237-247.

[77] A. Samad, K. Lee, K. Kim, Multi-objective optimization of a dimpled channel for heat transfer augmentation, Heat and Mass Transfer, 45(2) (2008) 207-217.

[78] S.R. Sargent, C.R. Hedlund, P.M. Ligrani, An infrared thermography imaging system for convective heat transfer measurements in complex flows, Measurement Science and Technology, 9(12) (1998) 1974-1981.

[79] B. Schilder, S.C.M. Yu, N. Kasagi, S. Hardt, P. Stephan, Local Measurement of Forced Convection Heat Transfer in a Micro Glass Tube, in: ASME 6th International Conference on Nanochannels, Microchannels, and Minichannels, Darmstadt, Germany, 2008, pp. 543-550.

[80] H. Schlichting, K. Gersten, Boundary-Layer Theory, MacGraw-Hill, 2000.

[81] R.S. Snedeker, C. Dup, Observation of a bistable flow in a hemispherical cavity, AIAA Journal, 4(4) (1966) 735-736.

[82] E.M. Sparrow, D.L. Misterek, Mass Transfer at the Base of a Cylindrical Cavity Recessed in the Floor of a Flat Duct, Journal of Heat Transfer, 108(4) (1986) 853.

[83] T.I.A.f.t.P.o.W.a. Steam, Release on the IAPWS Formulation 2008 for the Viscosity of Ordinary Water Substance, in, Berlin, 2008.

[84] T.I.A.f.t.P.o.W.a. Steam, Release on the IAPWS Formulation 2011 for the Thermal Conductivity of Ordinary Water Substance, Plzeň, Czech Republic, 2011.

[85] P. Stephan, N. Schweizer, Experimental Study of Bubble Behavior and Local Heat Flux in Pool Boiling under Variable Gravitational Conditions, Multiphase Science and Technology, 21(4) (2009) 329-350.

[86] P. Stephan, E. Wagner, R. Nasarek, Liquid Crystal Technique for Measuring Temperature, in: Encyclopedia of Microfluidics and Nanofluidics, Springer US, 2008, pp. 1012-1022.

[87] N. Syred, A. Khalatov, A. Kozlov, A. Shchukin, R. Agachev, Effect of Surface Curvature on Heat Transfer and Hydrodynamics Within a Single Hemispherical Dimple, Journal of Turbomachinery, 123(3) (2001) 609.

[88] V.I. Terekhov, S.V. Kalinina, Flow and heat transfer in a single spherical cavity: State of the problem and unanswered questions (review), Thermophysics and Aeromechanics, 9(4) (2002) p. 475-496.

[89] V.I. Terekhov, S.V. Kalinina, Y.M. Mshvidobadze, Convective heat transfer on the surface behind a spherical cavity, Thermophysics and Aeromechanics, 1(1) (1994) p. 13-18.

[90] V.I. Terekhov, S.V. Kalinina, Y.M. Mshvidobadze, The Effects of Geometric and Dynamic Flow Parameters on Heat Transfer in a Spherical Cavity, Journal of Engineering Thermophysics, 11(2) (2002) p. 153-166.

[91] V.I. Terekhov, S.V. Kalinina, Y.M. Mshvidobadze, Flow Structure and Heat Transfer on a Surface with Single Hole Depression, Russian Journal of Engineering Thermophysics, 5(1) (1995) p. 11-16.

[92] V.I. Terekhov, S.V. Kalinina, Y.M. Mshvidobadze, Heat Transfer Coefficient and Aerodynamic Resistance on a Surface with a Single Dimple, 4(2) (1997) 131-145.

[93] V.I. Terekhov, N.I. Yarygina, R.F. Zhdanov, Heat transfer in turbulent separated flows in the presence of high free-stream turbulence, International Journal of Heat and Mass Transfer, 46(23) (2003) 4535-4551.

[94] M. Van Dyke, An album of fluid motion, Parabolic Press, 1982.

[95] V. Voskoboinick, N. Kornev, J. Turnow, Study of Near Wall Coherent Flow Structures on Dimpled Surfaces Using Unsteady Pressure Measurements, Flow, Turbulence and Combustion, 90(4) (2012) 709-722.

[96] E. Wagner, Hochauflösende Messungen beim Blasensieden von Reinstoffen und binären Gemischen, Dissertation, Division: Thecnical Thermodynamics, Technischen Universität Darmstadt, Shaker Verlag, Aachen, 2009.

[97] E. Wagner, P. Stephan, High-Resolution Measurements at Nucleate Boiling of Pure FC-84 and FC-3284 and Its Binary Mixtures, Journal of Heat Transfer, 131(12) (2009) 121008.

[98] X.J. Wei, Y.K. Joshi, P.M. Ligrani, Numerical Simulation of Laminar Flow and Heat Transfer Inside a Microchannel With One Dimpled Surface, Journal of Electronic Packaging, 129(1) (2007) 63.

[99] N. Xiao, Q. Zhang, P.M. Ligrani, R. Mongia, Thermal performance of dimpled surfaces in laminar flows, International Journal of Heat and Mass Transfer, 52(7-8) (2009) 2009-2017.

[100] T.H. Yen, M. Shoji, F. Takemura, Y. Suzuki, N. Kasagi, Visualization of convective boiling heat transfer in single microchannels with different shaped cross-sections, International Journal of Heat and Mass Transfer, 49(21-22) (2006) 3884-3894.

[101] F. Zhou, S. Acharya, Mass/Heat Transfer in Dimpled Two-Pass Coolant Passages with Rotation, Annals of the New York Academy of Sciences, 934(1) (2006) 424-431.